THEORY AND OBSERVATIONS OF THE MAGNETIC FIELD IN THE SOLAR CORONA

Laura Carcedo

A Thesis Submitted for the Degree of PhD
at the
University of St Andrews

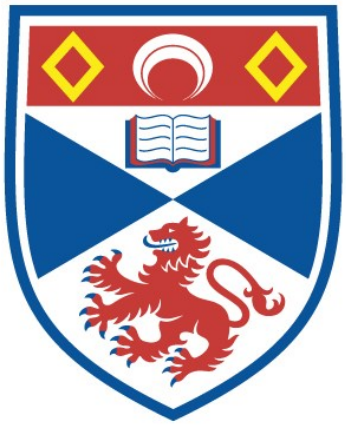

2005

Theory and Observations of the Magnetic Field in the Solar Corona

Laura Carcedo

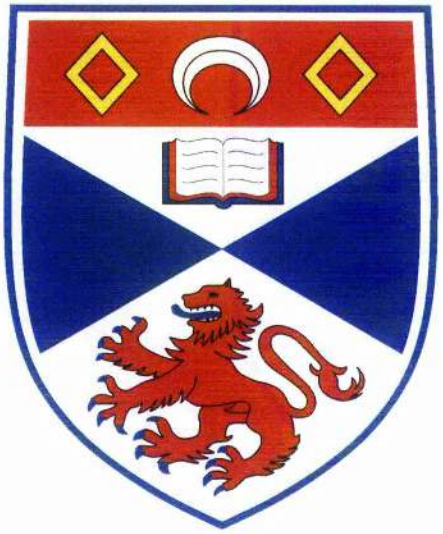

Thesis submitted for the degree of Doctor of Philosophy
of the University of St Andrews

May 14, 2005

ProQuest LLC.
789 East Eisenhower Parkway
P.O. Box 1346
Ann Arbor, MI 48106 – 1346

Abstract

Although the solar corona is one of the most studied areas in solar physics, its activity, such as flares, prominence eruptions and CMEs, is far from understood. Since the solar corona is a low-β plasma, its structure and dynamics are driven by the magnetic field.

The aim of this PhD thesis to study the magnetic field in the solar corona. Unfortunately, high quality direct measurements of the coronal magnetic field are not available and theoretical extrapolation using the observed photospheric magnetic field is required.

The thesis is mainly divided in two parts. The first part deals with the comparison between theoretical models of magnetic fields and observed structures in the corona. For any theoretical model, a quantitative method to fit magnetic field lines to observed coronal loops is introduced. This method provides a quantity C that measures how closely a theoretical model can reproduce the observed coronal structures.

Using linear force-free field extrapolation, the above field line fitting method is used to study the evolution of an active region. The method is also illustrated when the theoretical magnetic field depends on more than one parameter.

The second part of the thesis focuses on the linear force-free field assumption using two different geometric configurations. Firstly a vertical rigid magnetic flux tube is considered. The analytical expression of the magnetic field is obtained as an expansion in terms of Bessel functions. The main properties of this system are discussed and compared with two cylindrically symmetric twist profiles.

For the second system, the photosphere is assumed to be an infinite plane. Using translational geometry, the analytical expression of the linear force-free magnetic field that matches a prescribed line of sight magnetic field component is obtained. This solution is compared with the non linear solution obtained by Roumeliotis (1993).

Acknowledgements

Many people need to be acknowledge for their support during my postgraduate career. First and foremost I would like to thank my parents for always respecting my choices of study and supporting me throughout.

Particular thanks must go to Alan Hood for his constant support and supervision without which this thesis would not be possible. I would like to express my gratitude to the School of Mathematics and Statistics and specially to the Solar Theory Group.

I owe many thanks to the friends I made in Scotland, who were always there when I needed a hand, and to my friends and family in Spain, who have always welcomed me back home with open arms.

I would finally like to acknowledge gratefully the financial support of Particle Physics and Astronomy Research Council and the Instituto de Astrofísica de Canarias who appointed me for this grant.

Declaration

1. I, Laura Carcedo, hereby certify that this thesis, which is approximately 25,000 words in length, has been written by me, that it is a record of work carried out by me and that it has not been submitted in any previous application for a higher degree.

   date .....1/6/05.....signature of candidate P.

2. I was admitted as a research student in January 2001 and as a candidate for the degree of PhD in January 2002; the higher study for which this is a record was carried out in the University of St Andrews between 2001 and 2004

   date .....1/6/05.....signature of candidate .... Pp

3. I hereby certify that the candidate has fulfilled the conditions of the Resolution and Regulations appropriate to the degree of PhD in the University of St Andrews and that the candidate is qualified to submit the thesis in application for that degree

   date ....1/6/05..... signature of supervisor ..

4. In submitting this thesis to the University of St Andrews I understand that I am giving permission for it to be made available for use in accordance with the regulations of the University Library for the time being in force, subject to any copyright vested in the work not being affected thereby. I also understand that the title and abstract will be published and that a copy of the work may be made and supplied to any bona fide library or research worker.

   date .....1/6/05.....signature of candidate .... Pp

To my mother, who will always make me proud.

When I was a little kid my mother told me not to stare into the sun, so once when I was six, I did. At first the brightness was overwhelming, but I had seen that before. I kept looking, forcing myself not to blink, and then the brightness began to dissolve. My pupils shrunk to pinholes and everything came into focus and for a moment I understood.

- **Maximillian Cohen** in the motion picture ***"Pi"*** (1998).

Contents

List of Figures 4

List of Tables 6

1 Introduction 7

1.1 Solar Structure . . . 9

1.2 The Solar Corona . . . 10

1.2.1 Coronal Loops . . . 12

1.3 Solar Activity . . . 13

1.3.1 Coronal Mass Ejections . . . 13

1.3.2 CMEs and Other Phenomena . . . 15

1.3.3 CMEs and Sigmoids . . . 17

1.4 Solar Missions . . . 19

1.4.1 The Yohkoh Mission . . . 19

1.4.2 The SOHO Mission . . . 20

1.4.3 The TRACE Mission . . . 22

1.5 Outline of this Thesis . . . 22

2 Magnetic Extrapolation **24**

2.1 How to measure the magnetic field . . . 24

2.2 Force-free Models . . . 25

2.2.1 Potential Force-Free Field . . . 27

2.2.2 Linear Force-Free Field . . . 28

2.2.3 Non-Linear Force-Free Field . . . 31

2.3 Non Force-Free Models . . . 33

3 Magnetic Field Line Fitting of Observed Coronal Loops **35**
3.1 Introduction 35
3.2 Method of Approach 37
3.3 Application to linear force-free coronal loops 41
3.3.1 The footpoint positions for different values of α 43
3.4 Some comments about this Method 46
3.4.1 About Computational Time 48
3.5 Discussion and Conclusions 49

4 Further Applications of the Magnetic Field Line Fitting of Coronal Loops **51**
4.1 Magnetic Field Extrapolation of AR 8906 51
4.1.1 AR 8906 before the first eruption 54
4.1.2 AR 8960 after the first eruption 56
4.2 Magnetic Field Line Fitting for More than One Variable 57
4.3 Field Line Fitting Using Potential Fields 60
4.4 Comments and Conclusions 63

5 Approximating Non-Linear Force-Free Fields with Linear Force-Free Fields **65**
5.1 Cylindrical Geometry 66
5.1.1 General Axisymmetric Case 67
5.1.2 The Linear Force-Free Case 69
5.1.3 Magnetic Energy and Magnetic Helicity 80
5.1.4 Comparison Between Linear and Non-Linear Force-Free Field . . 84
5.1.5 Conclusions 93
5.2 Arcade Geometry 94
5.2.1 General Translational Symmetry Case 94
5.2.2 Non-linear Force-Free Field Case: An Analytical Solution 96
5.2.3 The Linear Force-Free Case 99
5.2.4 Magnetic Energy 105
5.2.5 Comparison Between Linear Force-Free Field and Non-Linear Force-Free Field 108
5.2.6 Conclusion 111

6 Summary and Further Work **113**

6.1 Summary 113

6.1.1 Comparing Theory and Observations 114

6.1.2 Linear Force-free Field 116

6.2 Future Work 117

6.2.1 Magnetic Field Line Fitting 117

6.2.2 Comparing Linear with Non Linear Force-Free Field 118

6.2.3 Future Missions 119

A Linear Force-free field using Green's Functions **121**

B Numerical Computation of Field Lines **128**

C Flux Function Coefficients for the Axisymmetric Geometry **130**

D Flux Function Coefficients for the Arcade Geometry **133**

Bibliography **136**

List of Figures

1.1 Cutaway drawing of Sun's interior. 9
1.2 Coronal loops observed by TRACE. 12
1.3 An example of a CME. 13
1.4 Sigmoid to arcade evolution 18

3.1 SOHO/MDI magnetogram and *Yohkoh*/SXT image of the full disk. 38
3.2 SOHO/MDI magnetogram and *Yohkoh*/SXT image of the selected AR. . . 39
3.3 SXT image with four simulated field lines. 39
3.4 The straighten coordinates. 40
3.5 The straighten coordinates in an example 42
3.6 The variation of C with the value of α. 43
3.7 Set of field lines for the obtained value of α. 44
3.8 Variation of the footpoints as the parameter α changes. 45
3.9 Comparing the results for different fitting functions. 47

4.1 SXT and MDI observations of the region through the three rotations. . . . 52
4.2 X-ray morphology of the AR before and after each CME. 53
4.3 SXT image showing the three regions. 54
4.4 Results for Region 2 before the first eruption. 55
4.5 Results for Region 3 before the first eruption. 55
4.6 Image and magnetogram of AR 8960 after the first eruption. 56
4.7 Results after the first eruption 57
4.8 Results of the fitting when both α and b are considered. 58
4.9 Selected field lines for different values of α and b. 59
4.10 TRACE observation of a groups of loops near the limb 60

4.11 Synoptic magnetogram with corrected for differential rotation. 62
4.12 Two TRACE loops and the best fitted field lines. 63

5.1 Flux tube of radius d and length $2L$. 69
5.2 Effect of L/d on the magnetic flux function, A. 76
5.3 The magnetic flux function, A, for several values of α 78
5.4 Contours of the magnetic field components for several values of α. 79
5.5 Field lines for two values of α. 80
5.6 Isosurfaces of the flux function, A, for different values of α. 81
5.7 Magnetic energy and helicity. 82
5.8 Magnetic field, twist and flux function at $z = 0$ and $L << d$. 85
5.9 Non-linear magnetic field and constant α field for different values of R^*. . 89
5.10 Non-linear magnetic field and constant α field for different values of R^*. . 91
5.11 Flux function for the Roumeliotis solution. 97
5.12 Magnetic field for the Roumeliotis solution. 97
5.13 Isosurfaces of the flux function $A^{(R)}$, for several values of z_0. 98
5.14 Geometry of the system for the translational case. 100
5.15 Flux function for the linear force-free field case. 104
5.16 Magnetic field for the linear force-free field case. 105
5.17 Isosurfaces of the flux function $A^{(\alpha)}$, for several values of α. 106
5.18 Magnetic energy for the translational geometry. 107
5.19 Percentage error in the approximated α. 109
5.20 Comparison between linear force-free field and Roumeliotis solution. . . 110
5.21 Field line comparison between linear force-free and Roumeliotis solutions. 111

List of Tables

1.1 The Sun's physical properties. 8

4.1 Distribution of GOES events and CME activity over three rotations. . . . 52

5.1 Special cases of the linear force-free magnetic field. 73
5.2 Comparison between both methods using Example 1. 90
5.3 Comparison between both methods using Example 2. 92
5.4 Comparison between Roumeliotis and linear magnetic energy. 111

6.1 Brief Summary of future solar missions. 120

Chapter 1

Introduction

The night has a thousand eyes.
And the day but one;
Yet the light of the bright world lies,
With the dying Sun.
- **Francis William Bourdillon** (1878).

The Sun is just one star of the hundreds of billions that populate our Galaxy. In fact, our sun is a G2 class star, which puts it in the middle of sequence of spectral classes. There are other stars which are much hotter or much cooler and intrinsically much brighter or fainter. Table 1.1 shows some of the Sun's physical properties[1].

What makes it so special is that it is "only" 150 million Km away; located in the centre of the solar system, its light and heat sustain all life on Earth. The scientific interests on the Sun can be divided in four categories:

1. The Sun is the heat engine that drives the circulation of our atmosphere; thus it is not difficult to presume that it is somehow responsible for the Earth's climate. Solar activity can influence Earth's climate in ways we must understand in order to enhance solar system research and our well-being.

2. But there is more than that. The Earth's surface is protected by its magnetic field and atmosphere, while the space is embedded in the solar wind. In the last decade,

[1] All values are taken from Lang (2001), for this table and the rest of the introduction.

Property		Value	
Mean distance to Earth		1 AU = 1.4959787×10^{11} m	
Light travel-time from Sun to Earth		499.004782 s	
Radius		$R_\odot = 6.955 \times 10^8$ m = 109 Earth radii	
Volume		$V_\odot = 1.412 \times 10^{27}$ m^3 = 1.3 million Earths	
Mass		$M_\odot = 1.989 \times 10^{30}$ Kg = 332946 Earth Masses	
Escape velocity at atmosphere		6.178×10^5 m s^{-1}	
Solar Constant		$f_\odot = 1366$ J s^{-1} m^{-2} = 1366 W m^{-2}	
Luminosity		$L_\odot = 3.85 \times 10^{26}$J s^{-1} = 3.85×10^{26} W	
Age		4.566×10^9 years	
Surface gravity		274 m s^{-2}	
Mass loss rate		10^9Kg s^{-1}	
Inclination to Earth's orbit		7°	
Angular momentum		1.7×10^{41} Kg m^2 s^{-1}	
Arc second		$1'' = 726 \times 10^6$ m	
Principal chemical constituents		(By number of atoms)	(By mass fraction)
	Hydrogen	92.1%	X = 70.68%
	Helium	7.8%	Y = 27.43%
	all others	0.1%	Z = 1.89%
Pressure	(core)	2.334×10^{16} Pa	
	(photosphere)	10 Pa	
Temperature	(core)	1.56×10^7 K	
	(radiative zone)	$1.5 \times 10^7 - 1.5 \times 10^6$ K	
	(convection zone)	$1.5 \times 10^6 - 6 \times 10^3$ K	
	(photosphere)	5780 K	
	(chromosphere)	$6 \times 10^3 - 2 \times 10^4$ K	
	(transition region)	$2 \times 10^4 - 2 \times 10^6$ K	
	(corona)	$2 \times 10^6 - 9 \times 10^6$ K	
Layers Thickness	(core)	0.25 $R_\odot = 1.74 \times 10^8$ m	
	(radiative zone)	0.45 $R_\odot = 2.72 \times 10^8$ m	
	(convection zone)	0.30 $R_\odot = 1.995 \times 10^8$ m	
	(photosphere)	5×10^5 m	
	(chromosphere)	2.5×10^6 m	
	(transition region)	$< 10^5$ m	
	(corona)	To the edge of solar system	
Density	(mean density)	1409 Kg m^{-3}	
	(core)	1.5×10^5 Kg m^{-3}	
	(photosphere)	10^{-4} Kg m^{-3}	
	(chromosphere)	10^{-10} Kg m^{-3}	
	(corona)	10^{-12} Kg m^{-3}	
Rotation Period	(equator)	26.8 days	
	(30° latitude)	28.2 days	
	(60° latitude)	30.8 days	
Magnetic Field	(sunspots)	$0.1 - 0.4$ T = $1 \times 10^3 - 4 \times 10^3$ G	
	(polar)	0.001 T = 10 G	
	(Earth)	0.00003 T = 0.3 G	

Table 1.1: The Sun's physical properties.

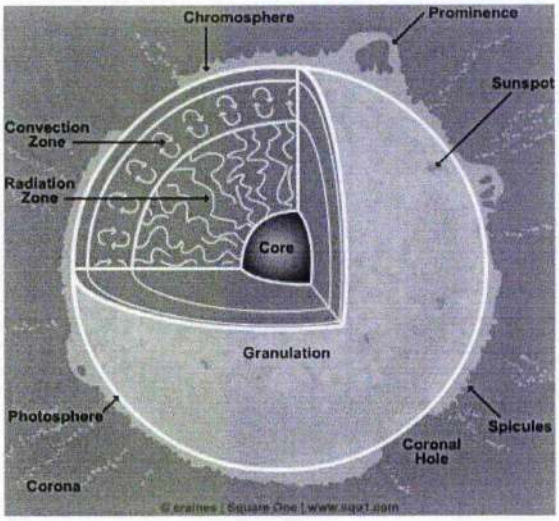

Figure 1.1: Cutaway drawing of Sun's interior. Image by Caroline Raines of Square One *research* PTY LTD (http://www.squ1.com).

the attention focused on space-weather has grown considerably, in an attempt to predict magnetic storms that would affect satellites and space stations

3. The Sun is also the key for understanding our universe. Unlike the rest of the stars we observe, this one can be studied in great detail. The same way we can not completely understand matter until we master the atom, we will not be able to comprehend how galaxies work without an in-depth knowledge of our Sun.

4. The Sun is a gigantic nuclear fusion plant composed of plasma. Therefore, there is also a connection between solar physics, laboratory research on plasmas and nuclear fusion research.

1.1 Solar Structure

The Sun is divided into many layers, as illustrated in Figure 1.1. All of the Sun's energy is produced by nuclear fusion in the *core*, where densities and temperatures are high enough. This energy will be transported to the outer layers of the Sun through two types of processes: *radiation*, which involves movement of energy but not of material, and *convection* where motions of the plasma transport the energy as kinetic energy.

It takes 10^7 years for photons to reach the Sun's surface, called *photosphere*[2]. The photosphere is observed in white light and this is where most of the energy is radiated. The features we can observe in the photosphere include *granules*, *supergranules* and *sunspots*.

Above the photosphere, there is a thin layer (2.5 million metres thick) called the *chromosphere*. Here the temperature rises from 6000 K to 20000 K and the density is a million times less than in the photosphere; the chromosphere is so faint that it was traditionally only visible during solar eclipses. The chromosphere's brightest emission lines are the hydrogen-alpha (or Hα, of 656.3 nm of wavelength) and the singly-ionised calcium (or Ca II, of 393.4 nm). The features observed in the chromosphere are the *chromospheric network* of magnetic field elements (that outline the boundaries of *supergranular cells*), bright *plages* around dark *sunspots*, dark *filaments* across the disk and *prominences* above the limb.

The *transition region* is a layer of less than a hundred thousand metres long between the corona and the chromosphere. In this layer the temperature increases and the density decreases quite dramatically with height. The transition region can be observed in the ultraviolet.

This PhD thesis is mainly focused in the solar corona and its magnetic field, which are explained on more detail in the next section.

1.2 The Solar Corona

The Solar corona extends above the visible surface of the Sun. This tenuous solar atmosphere is expanding in all directions, filling interplanetary space. It consists of hot, fully ionised, diffuse plasma (T = 10^6 K, $\rho = 10^{-14}$ Kg m^{-3}).

Because of its high temperature, the actual emission of the corona is mainly at short wavelengths, such as extreme ultraviolet (or EUV, of 10 to 100 nm) and X-ray (of 0.01 to 10 nm). It can also be seen in the visible light, during eclipses or by using *coronagraphs* (where the bright light of the Sun's photosphere is blocked out by an occulting disk, providing an artificial eclipse).

[2]Technically, the Sun has no surface; its gas just becomes more tenuous the further out you go. But it is common to consider its surface as the level beyond which the gas becomes transparent.

Observations of the corona show very bright areas, called *active regions* (ARs) on a less bright background known as the *quiet corona*. ARs have intense photospheric magnetic fields, as well as complex overlying magnetic field structures. In addition, sunspots and flares are located within ARs.

The coronal magnetic field is initially generated inside the Sun and then rises by magnetic buoyancy to the surface. Because the photosphere is so much denser, the gas pressure dominates over the magnetic pressure which means that the footpoints of the magnetic field are anchored in the dense photospheric plasma. Consequently, the evolution of the coronal magnetic field is determined by the motions of photospheric footpoints in response to fluid motion generated, for example, by convection. Since the bulk of the corona is effectively perfectly conducting, the topology of the magnetic field will only change if current sheets are formed.

On the other hand, away from the footpoints in the lower corona, the situation is the opposite, the magnetic pressure dominates and the hot particles are constrained by the magnetic field; also, any static magnetic field must be, to a large extent, force-free.

Once in the corona, the magnetic field can be divided into two types:

- Closed magnetic field: forming *coronal* loops such as shown in Figure 1.2 and *helmet streamers*. Located in the low corona, over neutral lines, helmet streamers connect regions of opposite polarity and commonly straddle a prominence embedded in the base of the streamer.
- Open magnetic field: forming *coronal holes* (which are dark regions observed in X-ray images), and producing the *solar wind* (which is a fast stream of plasma expelled from the Sun into the interplanetary space).

The high temperature in the corona remains one of the major unsolved mysteries in solar physics. The mechanism that transports energy from the photosphere, or below, to the corona is unknown, although many candidates have been identified. Coronal heating is a very broad area of research and it is not discussed further in this thesis.

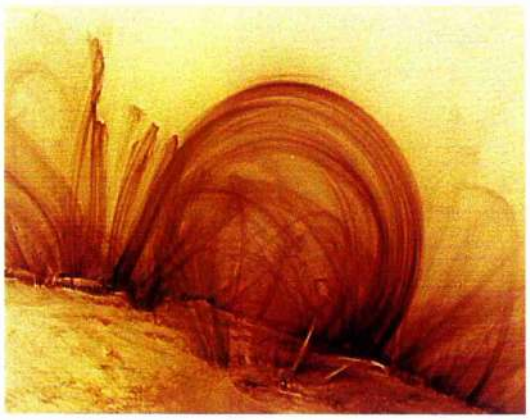

Figure 1.2: Coronal loops observed by the TRACE 171$\AA$ pass band, on November 6, 1999, at 02:30 UT. The image has been rotated over +90 degrees. Photo: NASA and the TRACE team.

1.2.1 Coronal Loops

X-Ray and EUV images show that the hottest and densest plasma in the corona is concentrated in long and thin closed structures called *coronal loops*. These loops connect regions of opposite polarity in the photosphere called *footpoints*, and present a very fine structure which can be seen in Figure 1.2.

In the Solar Corona the magnetic Reynolds number (which is the ration of the advective and diffusive terms on the induction equation) is very large which means that diffusion is negligible. Therefore the highly ionised plasma is frozen-into the magnetic field outlining the shape of magnetic field lines. Observed coronal loops indicate that they are essentially toroidal in shape and have a constant cross-section along their length. Furthermore, the length is approximately ten times the width and so the aspect ratio is usually large. Coronal loop lengths range from tens of Mm to hundreds of Mm, depending on where they are located (within one AR, interconnecting two distinct ARs or even in the quiet corona). Coronal loops may last for days or weeks, they constantly move and change shape, indicating the presence of a very dynamic magnetic field. The three-dimensional structure and the dynamics of these loops is an area of active research.

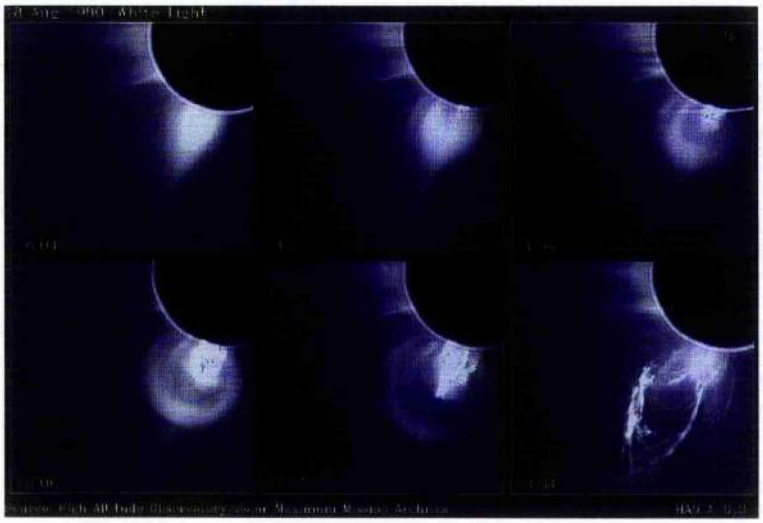

Figure 1.3: Sequence of six images of the Sun's corona, taken over the course of about three hours, showing a coronal mass ejection. Image taken form the archives of the High Altitude Observatory (National Centre for Atmospheric Research) and the Solar Maximum Mission (NASA).

1.3 Solar Activity

It has long been known that the Sun is neither featureless nor steady, Theophrastus first identified sunspots in the year 325 B.C. There is a wide range of studied phenomena, such as sunspot cycles, prominence eruptions, solar flares and coronal mass ejections. In Chapter 4, the magnetic conditions prior to and after a coronal mass ejection are examined. Coronal mass ejections are the biggest phenomena detected in the corona and they have been getting increasing attention in the past years. The following sections describe the current knowledge of such phenomena and how it relates to other solar activity.

1.3.1 Coronal Mass Ejections

Coronal Mass Ejections (CMEs) are large-scale eruptions from the solar corona, ejecting vast amounts of plasma into the solar wind. The nature and cause of CMEs, whilst magnetic in nature, are fundamental, unsolved problems.

CMEs involve the eruption of coronal plasma from closed magnetic field regions, such as helmet streamers, which can increase in brightness and size for days before erupting as a CME. The streamer disappears afterwards, leaving the region with open magnetic field,

but they differ from the open field regions found in the quiet corona.

Once a mass ejection has erupted, its outward motion may sweep up additional plasma and magnetic field from the overlying corona and interplanetary space. The compression of this magnetised plasma can, in extreme cases, lead to formation of a magnetohydrodynamic shock.

Figure 1.3 shows an example of a standard type of CME, called *loop-like ejection*. This type of ejection has three different parts, which can be seen in the bottom-middle picture: a loop-like front, produced by the distortion of the original helmet streamer, a dark low-density cavity, and a bright loop or core of denser material which is believed to be the prominence plasma that erupted as part of the mass ejection.

The large spatial scales involved (average width of 45^o, which do not change significantly over the cycle) make CMEs one of the biggest phenomena detected in the corona, only comparable with large prominences.

There is a large variability in several important characteristics of CMEs:

- *Speed*: 10 - 2100 km/s. Most mass ejections move in a nearly radial direction through the corona; their azimuthal expansion is usually slow and limited. CMEs exhibit a differential speed gradient, smoothly varying from the fast leading edge to the trailing, interior material as in self-similar expansion.
- *Acceleration*: ranges over 3 orders of magnitude. It occurs in the low corona; above the height of about 2 $R_\odot$ the speeds are relatively constant.
- *Mass*: $5 \times 10^{12} - 5 \times 10^{13}$ Kg.
- *Latitude Distribution*: The latitude distribution of CMEs depends on the phase of the solar cycle. It is very board during solar maximum and around the equator at minimum. This variation more closely parallels that of the streamers and prominences than of active regions, flares or sunspots.

Kinetic Properties of CMEs

Looking at the dynamical properties of CMEs, we find two clearly different types of CMEs:

1. Slow, gradually accelerating, associated with prominence eruptions. They tend to be balloon-like with central cores which accelerate more slowly than the leading edge. Out of the sky-plane, where they are more influenced by the solar wind, they look like smooth halos which accelerate to a limiting value (at about 3-6 $R_\odot$) and then fade away (disappearing by 20 $R_\odot$).

2. Fast CMEs with constant speeds (even as far out as 30 $R_\odot$), associated with flares. Out of the sky-plane they have a ragged structure and decelerate.

1.3.2 CMEs and Other Phenomena

CMEs and Sunspots

Hindler (1977) found a relationship between the spatial distribution of mass ejections and sunspots, suggesting a temporal relationship between the mass ejection frequency and sunspots number variation over the activity cycle. He also estimated the contributions of mass ejections to the solar wind at times of high solar activity.

St. Cyr and Webb (1991) found that the 11-year variations in mass ejection frequency are also related to the frequencies of flares observed in Hα emissions. They concluded that over the long term, there is no class of activity tracer that correlates with CME production rate better than any other. This is not surprising if we consider that all these forms of activity are related to the evolution of the solar magnetic field.

CMEs and Prominence Eruptions

One of the most common near surface activities associated with CMEs is the eruption of a prominence. Erupting prominences have often been identified as a bright feature in the interior of loop-like CMEs. There are many models where prominence eruptions drive coronal mass ejections, although there are some facts against this point of view:

1. Many mass ejections, including loop-like ones, are observed without a prominence eruption and with no hint of an interior feature in the mass ejection itself.

2. For some recorded cases, the CME has left the corona well before the prominence erupted (Wiik et al. (1997)).

3. In CMEs with an interior prominence, the prominence always moves outwards more slowly than the frontal loop of the CME.

4. The dark prominence cavity has a magnetic structure with a very different geometry and spatial scale from that of the prominence itself.

CMEs and "Optical" Solar Flares

Solar flares are sudden and violent release of matter and energy within a solar active region, driven by magnetic reconnection. It may be the result of the nonlinear evolution of an ideal MHD instability.

"Optical" Solar Flares are sudden brightenings of a region of the Sun in the visible portion of the solar spectrum (usually in Hα emission). Studies of activity associated with CMEs have found that these "optical" flares occur near the onset and location of only a minority of mass ejections.

CMEs occurring with these flares are less common than CMEs that have associated prominence eruptions. Most optical flares occur independently of CMEs and even those accompanying CMEs may be a secondary consequence rather than a cause of CMEs. However, the fastest, most energetic CMEs are usually also associated with surface flares. When extrapolating back to near-simultaneous onset of the multiple activities, uncertainties make disentangling cause and effect difficult.

CMEs and Soft X-Ray Flares

Emission of soft X-ray (SXR) and shorter wavelengths has been recognised as a direct indication of coronal plasma heating during a solar flare and they are important in the study of the thermal aspects and consequences of the flare process.

Statistical association studies indicate that erupting filaments and X-ray events, especially of long duration, are the most common near-surface activity associated with CMEs. Sheeley et al. (1984) first showed that the probability of associating a CME with a SXR flare increased linearly with the flare duration, reaching 100% for flare events of duration longer than six hours.

Hundhausen (1998), compared mass ejections and soft X-ray emissions to conclude

that:

1. Intense soft X-ray flares are neither a necessary nor a sufficient condition for the occurrence of coronal mass ejections.
2. Significant soft X-ray emission, if it does accompany a mass ejection, follows the acceleration of mass ejection features and peaks well after the ejection is under way.
3. The intensity of any soft X-ray flare that accompanies a mass ejection is not closely related to the characteristics of the ejection.

Harrison (1995), suggested that a CME and the associated flare are signatures of the same magnetic "disease", that is, they represent the responses in different parts of the magnetic structure, to a particular activity; they do not drive one another but are closely related.

1.3.3 CMEs and Sigmoids

Sigmoids are large S-shaped structures often seen in soft X-ray (SXR). Understanding their nature is important since active regions showing sigmoids are found to be statistically more likely to produce flares and CMEs. The fact that they are more apparent in SXR images than in EUV images indicates that sigmoids are hotter features than typically seen in EUV.

Sigmoid structures are likely the result of twisted solar magnetic fields; there are two distinct possibilities:

1. Sigmoids trace twisted fields within flux tubes.
2. Sigmoids arise on only certain field lines with special topological characteristics. These field lines, called *separatrix surfaces*, are where reconnection can occur and enhance SXR emission. This possibility does not explain patterns in the quiet corona and in steady-state structures.

There are two main mechanisms for the formation of sigmoidal structures, depending on their location. Inside ARs, the main mechanism is believed to be reconnection of smaller flux tubes that emerge from beneath the solar photosphere; while outside ARs, random

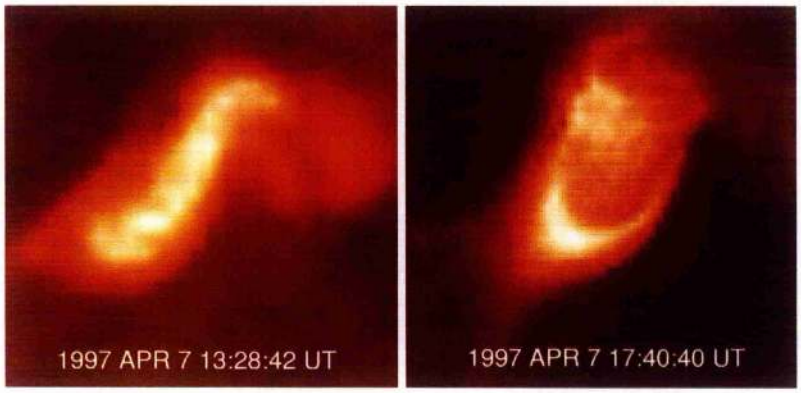

Figure 1.4: Views of the CME source region for the halo CME of 7 April, 1997 in soft X-rays from SXT on *Yohkoh*. Left image corresponds to the region before the eruption and right image after the eruption.

footpoint movement (due to photospheric supergranular motions) and shearing footpoint motions (due to rotation and diffusion) generate the twisted magnetic field necessary for the formation of sigmoids.

Twisted magnetic structures have long been associated with filament eruption and two-ribbon flares. Recently their connection with the ejection of CMEs has received increased attention. Based on the observations, Sterling (2000) concluded that:

1. Regions that are sigmoidal in shape prior to the eruption evolve into un-sheared arcades or cusp shapes after the eruption. This is generally called *sigmoid-to-arcade evolution* and the process consists on two steps:

   (a) The magnetic field stores energy via helicity, producing an S-shaped sigmoid.

   (b) At some point, this sigmoid becomes unstable and erupts, losing some of its complexity or even disappearing completely.

   An example of this is shown in Figure 1.4.

2. Footpoints of the pre-eruption features are different from footpoints of the post-eruption features.

3. Dimming regions associated with the sigmoid-feature eruptions are seen in both SXRs and EUV and the associated mass is an order of magnitude (or more) less than of a typical CME. This raises the question of whether the sigmoid regions are sources for the entire CME, or only for one portion of the structure.

1.4 Solar Missions

This thesis will include both theory and observations. Most of the observations used have been taking from two space missions: *Yohkoh* and SOHO, which are described in the next sections.

1.4.1 The Yohkoh Mission

Yohkoh ("Sunbeam" in Japanese) was a satellite dedicated to high-energy observations of the Sun, specifically of flares and other coronal disturbances. It was a project of the Institute for Space and Astronautical Sciences of Japan, but the observing instruments have contributions from United States and the United Kingdom. The *Yohkoh* mission was launched the 30th of August, 1991, from the Kagoshima Space Centre in southern Japan. In December 2001, during an solar eclipse, *Yohkoh* lost pointing and the batteries discharged. This failure put an end to the mission.

The spacecraft carried four different instruments:

The Soft X-ray Telescope (SXT) was a grazing-incidence reflecting telescope in the soft X-ray band (3-60 Å), with energies of 0.25-4 Kev. Its time resolution was up to 0.5 seconds and its spatial resolution was 2.5 arcseconds.

The Hard X-ray Telescope (HXT) was a Fourier synthesis telescope. Images in four energy bands (15-24-35-57-100 KeV) were obtained simultaneously with a temporal resolution of 0.5 seconds and a spatial resolution of 5 arcseconds.

The Bragg Crystal Spectrometer (BCS) consisted of four bent-crystal spectrometers with position-sensitive proportional counters. It observed the line complexes of Fe XXVI, Fe XXV, Ca XIX and S XV. It was designed to study plasma heating and dynamics during the impulse phase of solar flares.

The Wide Band Spectrometer (WBS) observed the overall energy release between soft X-rays and gamma-rays using three separate instrument packages: the Soft X-ray Spectrometer (2-30 KeV), the Hard X-ray Spectrometer (20-400 KeV) and the Gamma-Ray Spectrometer (0.2-100 MeV).

Together these instruments provided the most detailed record obtained of high-energy processes in solar flares and in other forms of solar coronal activity. More information on *Yohkoh* can be found in the special edition of Solar Physics, de Jager et al. (1991).

1.4.2 The SOHO Mission

The SOHO (Solar and Heliospheric Observatory) project is being carried out by the European Space Agency (ESA) and the United States National Aeronautics and Space Administration (NASA). Launched on 2nd December, 1995, SOHO is the first satellite to provide an uninterrupted view of the Sun. This is achieved by operating SOHO from a permanent vantage point 1.5 million kilometres sunward of the Earth in a halo orbit around the L1 Lagrangian point (approximately where the Sun's and Earth's gravitational pull are equal).

The spacecraft carried twelve different instruments divided into the three principal scientific objectives:

1. Study of the solar interior using the techniques of helioseismology:

   The Global Oscillations at Low Frequencies (GOLF) aims to study the internal structure of the sun by measuring the spectrum of global oscillations in the frequency range $10^{-7} - 10^{-2}$ Hz. Both p (pressure) and g (gravity) mode oscillations are investigated, with the emphasis on the low order long period waves which penetrate the solar core.

   The Michelson Doppler Imager (MDI) consists of a wide-field tunable Michelson interferometer which samples the Ni I 676.8 nm line. It provides high resolution solar images of the line of sight velocity, line intensity, continuum intensity and longitudinal magnetic field of the photosphere. It has a resolution of 4 arcseconds over the whole disk.

   The Variability of Solar Irradiance and Gravity Oscillations (VIRGO) measures the total and spectral irradiance and spectral radiance variation of the Sun, its polar and equatorial diameters and frequencies, amplitudes and phases of oscillation modes in the frequency range of 1 MHz to 8 MHz.

2. Study the heating mechanisms of the solar corona:

The Coronal Diagnostic Spectrometer (CDS) provides diagnostic information regarding solar atmosphere plasmas through the detection and analysis of spectral emission lines in the EUV of 150-800 Å, which corresponds to temperatures of 104-106K.

The Extreme Ultraviolet Imaging Telescope (EIT) is able to image the solar transition region and inner corona in four selected bandpasses in the extreme ultraviolet (EUV): Fe IX/X (171 Å), Fe XII (195 Å), Fe XV (284 Å) and He II (304 Å).

The Large Angle and Spectrometric Coronagraph (LASCO) is a wide-field white light and spectrometric coronagraph consisting of three optical systems having nested fields of view. Together, they observe the solar corona from just above the limb at 1.1 solar radii out to 32 solar radii.

The Solar Ultraviolet Measurements of Emitted Radiation (SUMER) is a UV telescope equipped with a normal incidence spectrometer to study plasma flows, temperatures, densities and wave motions from the upper chromosphere to the lower corona. It has a spatial resolution of 1.5 arcseconds, a time resolution of 10 seconds and velocity resolution of 1 km/s.

The Ultraviolet Coronagraph Spectrometer (UVCS) is an occulted telescope that provides spectroscopic measurements at ultraviolet wavelengths in the region between 1.3 and 10 solar radii. This data is used to obtain the proton velocity distribution, proton outflow velocity, electron temperature and O VI, Si XII, and Mg X outflow velocities and densities.

3. Investigation of the solar wind and its acceleration processes:

The Charge, Element and Isotope Analysis System (CELIAS) is designed to study the composition of the solar wind and of solar and interplanetary energetic particles.

The Comprehensive Suprathermal and Energetic Particle Analyser (COSTEP) determines the energy distribution for different particle species (protons, helium ions and electrons).

The Energetic and Relativistic Nuclei and Electron experiment (ERNE) records the high energy distribution (above 1 MeV/nucleon) of the fast moving streams of particles produced by energy eruptions in the solar atmosphere.

The Solar Wind Anisotropies (SWAN) is devoted to the measurement of large scale structures of the solar wind, and in particular the distribution with heliographic latitude of the solar wind mass flux.

More information on the SOHO mission can be obtained in the special edition of Solar Physics, de Jager et al. (1995).

1.4.3 The TRACE Mission

The Transition Region and Coronal Explorer (TRACE) satellite, launched 2 April 1998, is a NASA Small Explorer (SMEX) that images the solar photosphere, transition region and corona with high spatial and temporal resolution (1 arc second and 1 min respectively).

TRACE contains multilayered optics and a lumogen-coated CCD detector to record three EUV wavelengths and several UV wavelengths. It observes plasmas at selected temperatures from 6000 K to 10 MK with a typical temporal resolution of less than 1 min.

More information about TRACE can be found in Handy et al. (1999).

1.5 Outline of this Thesis

This PhD thesis will study the magnetic field in the corona using both theory and observations.

Chapter 2 summarises the principal ways to extrapolate the photospheric magnetic field into the corona. These reconstruction methods have been widely used to compare with coronal strutures.

Chapter 3 proposes a quantitative way to compare theoretical coronal magnetic fields with observations. It is common, when extrapolating the magnetic field into the corona, to have some free parameters which are necessary to adjust in order to reproduce the coronal structures observed. The method suggested in this chapter will return the value of the free parameters that provide the best correlation with the observations. This method is illustrated with an example using linear force-free field extrapolation and *Yohkoh*/SXT images.

Chapter 4 is dedicated to further applications of the above field line fitting method. It is divided in three sectons: In Section 4.1, the method discussed in Chapter 3 is used to study a complete active region using linear force-free fields before and after an eruption. In Section 4.2 the above method is used when two free parameters are needed. Finally, in Section 4.3 the field line fitting method is used for a potential field, where the position of the footpoints act as the parameters the magnetic field depends on.

Chapter 5 will discuss how linear force-free field compare with other more general solutions. It studies two different geometries: Section 5.2 uses azimuthal symmetry while Section 5.2 uses translational symmetry.

Finally, Chapter 6 includes a summary of the overall thesis, conclusions and suggested future work and lines of improvement.

Chapter 2

Magnetic Extrapolation

Originality consists in returning to the origin.
- **Antonio Gaudí** (1852 - 1926).

It is generally assumed that the magnetic pressure in the corona is much larger than the plasma pressure (a low β plasma), therefore its structure and dynamics are controlled by the local magnetic field. Eruptive events, such as flares, coronal mass ejections (CMEs) and eruptive prominences are driven by excess energy in the magnetic field. Knowledge of the magnetic structure of the corona plays a key role in providing a more complete understanding of such events.

Unfortunately, currently and probably also in near future, high quality direct measurements of coronal magnetic field are not available. As an alternative, many authors have modelled the coronal magnetic field by extrapolation from the observed magnetic field at the photospheric level.

2.1 How to measure the magnetic field

In the presence of a magnetic field, the atomic energy levels, the transitions between these levels, and the associated spectral lines split; the separation between levels is proportional to the magnetic field strength. This effect is called the *Zeeman effect* and can be used to measure the strength of the line of sight component of the magnetic field in the pho-

tosphere. The lines corresponding to Zeeman splitting also exhibit circular polarisation effects.

In the presence of a weak magnetic field, when the Zeeman splitting is comparable to the natural broadening of the line, the spectral lines are linearly polarised in contrast to the circular polarisation associated with the Zeeman effect. This is called the *Hanle effect*. Both Zeeman and Hanle effect combined can be used to obtain all the components of the magnetic field. More information about the Hanle effect can be found in Trujillo Bueno (2001).

To measure the magnetic field in the Sun, astronomers use *magnetograms*. These instruments consist on an array of tiny detectors that measure the Zeeman and Hanle effects at different locations across the photosphere. Linear magnetograms only measure the line of sight component of the magnetic field, while vector magnetograms measure the three components.

For the photosphere, the magnetically sensitive line has a wavelength of 525.02 nm and the above mechanism produces very impressive magnetograms. These magnetograms show how the photospheric magnetic field is far from uniform, with nearly all the magnetic flux concentrated in patches called *active regions*, surrounded by almost field free areas.

Unfortunately, for the corona, the magnetically sensitive lines are very faint and they have only occasionally been observed (e.g., House (1977); Arnaud and Newkirk (1987); Judge (1998)). To complement this, the new topic of coronal seismology can provide some information about the coronal magnetic field based on a detailed knowledge of the MHD waves modes (e.g. Roberts et al. (1984), Nakariakov and Ofman (2001), De Moortel and Hood (2000)). Although there has been new developments on the subject (Judge et al. (2001)) high quality direct measurements of the coronal magnetic field are not available.

2.2 Force-free Models

In astrophysical situations, the magnetic field is force-free when it is embedded in a tenuous compressible medium of high electrical conductivity such that the field energy far exceeds the kinetic or thermal energy of the medium. The force-free condition is a direct

dynamic consequence, and resistive diffusion can only take the magnetic field from one force-free configuration to another.

The momentum conservation equation in MHD is:

$$\rho\frac{D\mathbf{v}}{Dt} = -\nabla p + \mathbf{j}\times\mathbf{B} + \rho\mathbf{g}, \tag{2.1}$$

where $\mathbf{v}$ is the plasma velocity field, ρ is the plasma density, p is the plasma pressure, $\mathbf{j}$ is the current density, $\mathbf{B}$ is the magnetic field and $\mathbf{g}$ is the gravity field. For the solar corona velocities are considerably smaller than the Alfvén speed which make the left hand side of Equation (2.1) negligible. If the height of the region of interest is much less than the scale-height and the ratio

$$\beta = \frac{2\mu_0 p_0}{B_0^2} \tag{2.2}$$

is much less than unity, then the magnetic field dominates over pressure and gravity and can be assumed to be force-free (for another point of view see Gary (2001)). Thus the magnetic force cancels:

$$\mathbf{j}\times\mathbf{B} = 0. \tag{2.3}$$

Since

$$\mathbf{j} = \frac{1}{\mu_0}\nabla\times\mathbf{B}, \tag{2.4}$$

the above condition reduces to

$$\nabla\times\mathbf{B} = \alpha(\mathbf{r})\mathbf{B}, \tag{2.5}$$

where α is constant along the field lines but may depend on the position.

Depending on the assumptions imposed on α there are three main force-free models. For the *potential field* case, the parameter α vanishes and no magnetic current is present. α is considered constant for the *linear force-free field* case. Finally, the most general case is the *non-linear force-free field*, where α varies with the position. These three models will be explained in the following sections.

2.2.1 Potential Force-Free Field

This is the simplest model. It is also known as *current-free field* since no current is allowed. Under this assumption, the magnetic field should follow the following equations:

$$\nabla \times \mathbf{B} = 0, \tag{2.6}$$

$$\nabla \cdot \mathbf{B} = 0. \tag{2.7}$$

This potential assumption is very limited. In the high corona the solar wind distorts the magnetic field making the potential approximation unrealistic. In the chromosphere and lower corona, where mechanical energy is dissipated, large gradients of temperature and density may well generate electric currents (which in some instance can be considerable).

The biggest advantage of this model is that it is a well defined boundary value problem, where the Laplace equation has to be solved using Neumann boundary conditions. Therefore, the solution obtained, given the appropriate boundary conditions, will be unique.

Schmidt (1964) obtained the potential magnetic field above a limited photospheric region, S', assuming that the magnetic field component normal to the boundary plane is known inside S' and vanishes everywhere else. The magnetic field will be

$$\mathbf{B} = \nabla\phi, \tag{2.8}$$

where

$$\phi = -\frac{1}{2\pi}\int_{S'} \frac{B_z(x', y', z' = 0)}{(x - x')^2 + (y - y')^2 + z^2} dx'dy' \tag{2.9}$$

is the *scalar potential.* Although this is a mathematical rigourous solution for the current-free magnetic field above an infinite plane provided that the normal component of the magnetic field at the plane is everywhere specified, in practise, for a finite domain, the above expression for the magnetic field is reasonably correct as far as the contribution to the integral outside the magnetogram can be neglected and the magnetic field tends to zero faster than $1/r^{1.5}$ as z tends to infinity. Semel (1967) generalised the above result when an arbitrary component of the magnetic field is specified.

Schatten et al. (1969) and Altschuler and Newkirk (1969) computed the potential field in the full volume between the photosphere and a surface at some radial distance R_s (approximately $1.6R_\odot$ for Schatten et al. (1969) and $2.5R_\odot$ for Altschuler and Newkirk

(1969)). The assumption that the field becomes radial, thereby simulating the effects of the solar wind, provides the boundary condition at $r = R_s$. The surface $r = R_s$ is often called *source surface* since it serves as a source for the interplanetary magnetic field, and it is where currents in the corona cancel the transverse magnetic field. This source surface model is widely used to study solar wind, interplanetary magnetic field and coronal holes but it is not able to reproduce observations for middle and high latitudes structures (such as polar plums or coronal streamers). A more advanced approach introduced by Schatten (1971) and Zhao and Hoeksema (1994), includes current sheets between the oppositely directed open field lines.

2.2.2 Linear Force-Free Field

Though not generically observed, linear force-free field models provide an easy mathematical formulation to go beyond the potential field and allow studies of the simplest force-free fields.

Low (1973) stated that the linear force-free field is the only possibility for the magnetic field to remain force-free, whilst undergoing resistive diffusion in a static medium.

The magnetic energy of a linear force-free field is larger than the potential case, but linear force-free fields can not rapidly relax to potential due to the conservation of the magnetic helicity (see Berger (1984)). Both potential and linear force-free fields have no free energy, which can be released during an eruption related to ideal or resistive MHD-instabilities. Therefore they are poor approximations to ARs prior to an eruption.

In fact, the linear force-free field is the minimum energy state with a given total helicity (see Taylor (1974) and Woltjer (1958)). Therefore, if the helicity is conserved, plasmas loosing energy to fluid viscosity, may evolve towards the constant-α field. Although, most linear force-free configurations are topologically inaccessible given only ideal motions, reconnection can remove all topological constrains other than the total helicity conservation. Lothian and Browning (1995) considered the linear force-free field as a limit the magnetic field relaxes towards through localised reconnections, conserving helicity but converting free magnetic energy into thermal energy.

With the line of sight magnetogram, the linear force-free problem is ill posed, which means that the solution is not unique (Chiu and Hilton (1977), Seehafer (1978)). Also, the solution will have α as a free parameter that needs to be adjusted. In fact, the possible

values α can assume are always limited within a certain range.

Constant α force-free fields have to be constrained to finite areas. Seehafer (1978) calculated the magnetic field for the full volume around the Sun, given one component of the field in the photosphere. He found that the magnetic energy is not finite in this system and concluded that the extension of a global scale linear force-free field to infinity neither has a physical meaning nor provides a mathematically unique boundary value problem.

For the linear force-free field case, Equation (2.5) reduces to the Helmholtz equation

$$(\nabla^2 + \alpha^2)\mathbf{B} = 0. \tag{2.10}$$

The main methods to solve this equation are described in the sections below.

Fourier Series

Nakagawa and Raadu (1972) obtained the magnetic field above the centre of the disk, given the line of sight magnetogram in the photosphere. The magnetic energy and the twist increases with the value of α. The parameter α is constrained by $|\alpha| < 2\pi/L$, where L is the dimension of the magnetogram. Alissandrakis (1981) obtained the magnetic field above anywhere in the solar disk, given the longitudinal component of the magnetic field in the photosphere.

This method is more computationally efficient but it carries some disadvantages. The Fourier transform performed on a rectangular plane with the solutions being periodic. When using real data, it has to be placed in a computational grid and *aliasing* effects may arise, which consist of the distortion of the magnetic field at the edges of the observed regions. To mitigate this effect one solution consists on increasing the size of the computational box, but it produces a reduction in the possible values of α.

Green's Functions

Chiu and Hilton (1977) studied the boundary value problem of constant α force-free field in Cartesian geometry. They expressed the magnetic field in terms of the Green's function:

$$\mathbf{B}(x, y, z) = \frac{1}{2\pi} \int_{-\infty}^{\infty} \int_{-\infty}^{\infty} \mathbf{G}(x - x', y - y', z) B_z(x', y', 0) dx' dy'$$

$$+\frac{1}{2\pi}\int_{-\infty}^{\infty}\int_{-\infty}^{\infty}\tilde{\mathrm{G}}(x-x',y-y',z)H(x',y')dx'dy', \quad (2.11)$$

where $H(x,y)$ is any finite integrable function of the source coordinates, G is the Green's function and $\tilde{\mathrm{G}}$ is the "complementary" Green's function necessary to make Equation (2.11) a general solution for the magnetic field. The expression of both Green's function and how they are obtained is included in Appendix A.

Petrie and Lothian (2003) studied the effect of including the complementary Green's function. Choosing $H(x,y) = bB_z(x,y)$, where b is a real parameter, some simple systems of two and four sources where studied. When b has the same sign as α, the field tends to acquire additional twist. Conversely, when b and α have opposite signs, the twist decreases as b increases and can eventually be reversed. When studying the connectivity of different systems, they concluded that, the effect of b depends on the topological stability of the system and is less straightforward than the familiar response to varying α, but both parameters have comparable effects.

Chiu and Hilton (1977) studied the field for sets of 2-7 point sources. When $\alpha \neq 0$ the field lines acquire twist or "swirls" whose sense is reversed when the sign of α is reversed. As α increases, some field lines will wander quite far away of the region of interest, carrying large amounts of twist. This can be interpreted as developed forms of the *Kruskal-Shafranov* instability, which is a kink instability produced when the ratio between B_θ and B_z exceeds a certain aspect ratio, $2\pi aL$ for a plasma column, or R_0/a for toroidal devices (see Kruskal and Schwarzschild (1954) and Shafranov (1956)).

Seehafer (1978) obtained the linear force-free magnetic field for a semi-infinite column ($0 \leq x \leq L_x, 0 \leq y \leq L_y, 0 \leq z < \infty$), knowing B_z at the photosphere ($z = 0$) and imposing that $|B_z|$ vanishes at the boundaries ($x = 0, x = L_x, y = 0, y = L_y$).

Semel (1988) generalised the solution given by Chiu and Hilton (1977) to the oblique case.

Bessel's Function

Schatzman (1965) obtained a solution of the linear force-free equation for axial symmetry in terms of the Bessel functions, assuming an exponential decrease of the field with height. Nakagawa et al. (1971) generalised this solution as an expansion in terms of the

Bessel functions. They concluded that the obtained solution can reproduce some of the topological characteristics of the magnetic field in filaments and chromospheric fibrils near sunspots.

2.2.3 Non-Linear Force-Free Field

The use of non-linear fields is essential to understand eruptive phenomena, as there are both observational and theoretical reasons which suggest that the pre-eruptive magnetic fields are non-linear force-free. Linear force-free field minimises the magnetic energy under the assumption of global helicity conservation, therefore if helicity conservation holds for a coronal eruption, a linear force-free field would not be able to provide the necessary energy. Also, since non-linear force-free field takes into account the existence of localised electric currents, it is more suitable to determine the 3D magnetic configuration of ARs with complex topology.

If the parameter α is allowed to vary between field lines, the normal component of the magnetic field is insufficient as the boundary condition to solve Equation (2.5). To properly formulate the problem, it is necessary to supply all three components of the magnetic field. Unfortunately, vector magnetograms carry high uncertainties.

Non-linear force-free fields do not need to be constrained to a finite domain. Aly (1984) considered some general properties of three-dimensional, force-free fields in an infinite domain, D. If the magnetic field decays to zero sufficiently fast and the normal component is fixed on the boundary, the magnetic energy cannot be made arbitrary large. Therefore $W_0 \leq W_{FF} \leq W_{OPEN}$; where W_0 is the energy of the potential field, W_{FF} is the energy of the force-free field and W_{OPEN} is the energy of the open field.

Several methods to approach the non linear force-free field problem are discussed in the following sections.

Integrating from the Photosphere

The force-free equation can be reformulated in such away that the vector magnetogram is integrated upwards into the corona. Knowing the magnetic field at some height $z = z_0$, the magnetic field at a slightly higher level $z = z_0 + dz$ is computed using only the assumption that the intervening field is force-free. This method has been used by Wu

et al. (1990) and Amari et al. (1997). Unfortunately this system presents an ill posed problem, and slight errors in the computed magnetic field at one level grow exponentially with height. Although attempts have been made to regularise the method, the solution is limited to low heights only.

Grad-Rubin Method

This method was first introduced by Grad and Rubin (1958) and Sakurai (1981). The vertical component of the magnetic field and the distribution of α over an area of positive polarity in the photosphere is needed. From an initial potential field, an electric current is induced over the field lines emanating from the positive flux. The new non potential field will produce a new set of field lines and the current can be induced again. The method is iterated until the field lines do not change considerably. This scheme converges when α is sufficiently small, but it appears to break down for highly non-potential coronal fields. This method has also been used by Amari et al. (1997), Amari and Luciani (1999) and Amari et al. (1999).

MHD-Relaxation Methods

This scheme was introduced by Chodura and Schlueter (1981). Starting with a suitable magnetic field which is not in equilibrium, the system is let to relax into a force-free state. The difficulty is that it cannot be guaranteed that for the boundary conditions imposed and for a given initial magnetic field, a smooth force-free equilibrium exists to which the system can relax. Special care has to be taken in choosing the initial magnetic field, which limits the applicability of this relaxation method.

Roumeliotis (1996) proposed a "stress-and-relax" method for reconstructing the coronal magnetic field from vector magnetogram data. The initial magnetic field is the unique potential solution whose normal component at the photosphere coincide with the magnetogram data. This initial magnetic field undergoes alternating stressing and relaxing phases. In the stressing phase, the vector potential in the interior of the computational box is held fixed while the lower boundary is adjusted to better reproduced the observed transversed field. In the relaxation phase, the vector potential at the lower boundary is fixed while the magnetic field inside the computational box is allowed to relax to a nearby force-free configuration. The process is iterated until the difference between the lower boundary

and the magnetogram data is minimised.

Optimisation Method

This method was introduced by Wheatland et al. (2000). The optimisation method consists of minimising a functional containing a quadratic form of the force balance and the solenoidal condition. The magnetic field is not necessarily solenoidal during the computation, but it will be divergence-free if the optimal state is reached (thus, the functional vanishes). The problem is that it cannot be guaranteed that this optimal state is indeed reached for a given initial field and boundary conditions.

This optimisation method only needs vector magnetograms and not the α-photospheric distribution. The disadvantage is that it requires boundary conditions on all boundaries of the computational box. Wiegelmann (2004) deals with this problem by using a weighting function inside the functional so the solution is less dependent on the unknown boundaries, which are on the top and the sides of the computational box.

2.3 Non Force-Free Models

These model includes plasma pressure and gravity. They are needed when β is finite, such as in places like helmet streamers. In this case, the full magnetohydrostatic (MHS) equations are taken into account. Using the MHS approximation is justified when it is intended to study the state of the medium or relatively slowly evolving macroscopic plasma processes. Because of the non-linearity of the MHS equations, the problem of seeking all solutions is extremely complicated. Several approaches to constructing self-consistent MHS models are known to date, which permit analytic solutions to be determined. These approaches are based on some not fundamentally differing preliminary assumptions concerning the way in which the solutions behave.

Low (1985) showed that, if the electric current is assumed to flow perpendicular to gravity everywhere, the MHS equilibrium problem for atmospheres can be simplified to one of solving a single non-linear scalar partial differential equation. This *horizontal current* model may be most appropriately used to globally extrapolate the observed photospheric field into the corona near the solar minimum phase. Further horizontal current studies include Zhao and Hoeksema (1993), Zhao and Hoeksema (1994), Zhao et al.

(2000) and Petrie and Neukirch (2000).

Wiegelmann and Inhester (2003) showed that the information contained in a vector magnetogram together with a tomographic reconstructed coronal density distribution and the assumption of magnetohydrostatic force balance is sufficient to calculate the finite β coronal magnetic field. Unfortunately, both current vector magnetograms and tomographic reconstruction carry a considerable error, which make this method very hard to used with real data.

Chapter 3

Magnetic Field Line Fitting of Observed Coronal Loops

Never send a human to do a machine's job.
- **Agent Smith** in the motion picture "The Matrix" (1999)

3.1 Introduction

Present observations of coronal loops can be divided into two classes, namely those observed above the solar disk and those observed above the limb. Although the loops above the solar disk are genuinely three dimensional structures, their observations in soft X-rays and EUV provide images that are projected onto the disk and so only provide two dimensional information. Essentially, detailed information about the height is lost.

These restrictions will be removed by the NASA's Solar TErrestrial RElations Observatory (STEREO) mission, which will use two identically equipped spacecraft to provide 3D imaging of the Sun.

However, until that time, two-dimensional information is all that is available. Aschwanden et al. (1999) have developed a method of dynamic stereoscopy to reconstruct the three-dimensional geometry of loops, where the solar rotation is used to vary the aspect angle of otherwise static structures. This method assumes that the loops do not change signific-

antly in time.

As discussed in Section 2.1, the coronal field is largely unknown, and the only method to deduce the magnetic structure of the corona is to use theoretical models to extrapolate it from magnetic field data in the photosphere.

Magnetograms of the area can provide a boundary condition for the magnetic field in the photosphere. Using the magnetograms as boundary conditions, the coronal magnetic field can be extrapolated. For many magnetic field models, the coronal magnetic field will depend on one or more parameters whose values may be unknown.

Because of the small value of magnetic resistivity (or equivalently, the large value of the magnetic Reynolds number, R_m), the magnetic field and the plasma are "frozen-in" together. The negligible perpendicular thermal conduction means that heat rapidly spreads along the field but cannot diffuse across the field. Thus, neighbouring field lines can have a very different temperature. Hence, it is thought that the enhanced intensity outlines the local magnetic field in coronal loops (e.g. Zirin (1971), Frazier (1972), Poletto et al. (1975) and Levine (1976)).

Magnetic extrapolation has been used in many other studies. For example, Tang et al. (2000) studied a brightening event that occurred on 18 May 1994. They used *Yohkoh* soft X-ray images,vector magnetograms and Hα filtergrams and produced a magnetic extrapolation using a linear force-free field. The fit to the observations was produced by trial and error.

van Driel-Gesztelyi et al. (2000) studied two sigmoid events (on 25 October 1994 and 14 October 1995) and both were related to the onset of CMEs. Stokes vector magnetograms, from Mees Observatory, were matched to *Yohkoh* soft X-ray images using a linear force-free field. The method of construction is not specified.

Régnier and Amari (2001) and Régnier et al. (2002) studied the active region NOAA 8151 (11-13 February, 1998) in which a filament eruption is linked to the disappearance of a sigmoidal structure. Observational data was taken from *Yohkoh* soft X-ray images and vector magnetograms (from Mees Observatory) and a nonlinear force-free field using a vector potential, Grad-Rubin-like method was calculated numerically.

In order to fit the loops observed with extrapolated field lines, it is necessary to find the best value of the parameters that define the magnetic field (for example, α in the linear force-free case). The method that is most often used is to choose a value of the parameters,

plot some field lines and compare them "by eye" with the shape of the observed loops. If they do not look similar, another value for the parameters is chosen until a "similar" shape is found.

In this chapter the efficiency of this method is questioned. What makes one fit better than another? In some cases, a slight change of the parameters does not change the field line profile significantly, so no firm conclusions can be drawn about which is the best approximation. Also, the selection of which field lines to plot will have a bearing on the result. Are the selected field lines characteristic of the magnetic field? Furthermore, fitting a two-dimensional image to a 3D magnetic field calculation introduces an additional free parameter that has to be determined, namely the height of the field lines.

For these reasons, it is necessary to produce a more quantitative than a qualitative method to measure just how accurate the magnetic field extrapolation is. A possible solution to this problem is presented in this chapter. Section 3.2 describes the general method and Section 3.3 illustrates its use for the particular case of a linear force-free field (although the method can be used for any model that describes the magnetic field using a set of parameters).

Some effort in this direction has been introduced by Wiegelmann and Neukirch (2002). They presented a similar method but for three-dimensional structures, that will be applied to data from the SECCHI instrument aboard the STEREO mission.

3.2 Method of Approach

The method is split into several steps and a more detailed description of each step will be presented in Section 3.3 in the form of an example. While certain parts of the procedure can be automated, there are other sections that currently require human decisions.

Step 1. Co-align the magnetic data (e.g., from SOHO/MDI) and the loop image (e.g., X-ray from *Yohkoh*/SXT, or EUV from SOHO/EIT or TRACE, or H_α from the Solar Flare Telescope at the NAOJ): In general, photospheric magnetograms and loop images are taken from different instruments (therefore different positions) and not necessarily at the same time. For these reasons it is necessary to align both observations so that they are looking at the same area. An IDL routine was designed to deal with this, it basically clips and derotates a map structure to a

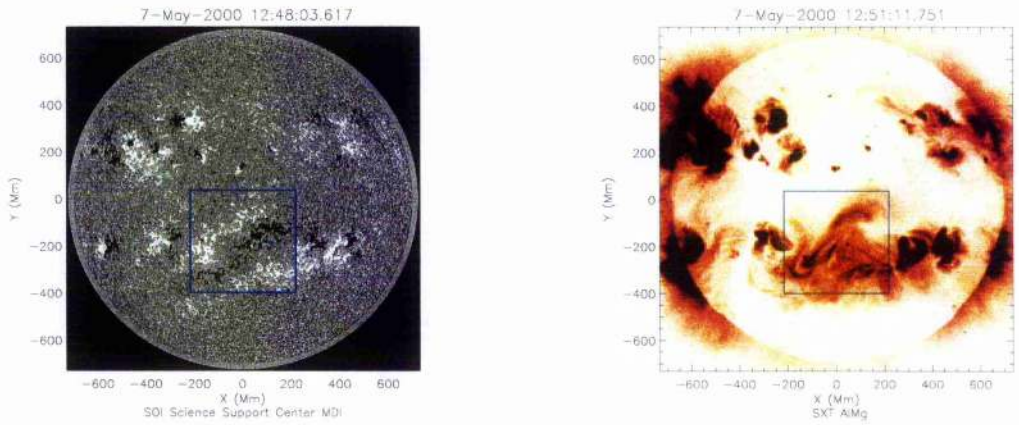

(a) (b)

Figure 3.1: (a) SOHO/MDI magnetogram and (b) *Yohkoh*/SXT image of the full disk. The magnetogram has been derotated to compensate form the different time and relative position respect the*Yohkoh*/SXT image.

region and time specified as an input. An example of this can be seen in Figure 3.1. This step will be less accurate as the difference in time becomes larger, therefore it is convenient to select image and magnetograms as simultaneous as possible.

Step 2. Identify the loop and its footpoint areas: The loop is identified in the intensity image and care should be taken to select a loop that does not have any other loops crossing either in front or behind it. In addition, it is essential that, to some degree, the complete loop can be seen. The footpoints are taken as the ends of the loop in the intensity, unless there is a dominant polarity source seen in the magnetograms. For simplicity, each footpoint area is a circle defined by its centre and radius, although a more complex definition could be applied. The value of the centre and radius is chosen so the entire end of the loop is included on it (or the entire source in the magnetogram). An example of this can be seen in Figure 3.2. The blue circles show the selected footpoints in both the magnetogram and the SXT image.

Step 3. Select a value for the magnetic field parameter, α: At this stage, α is simply an adjustable parameter or set of parameters in the magnetic field model. For the force-free assumption, α describes the non-potential nature of the field. In general though, α can be a (many) parameter(s) in the magnetic field model and the method is not restricted to linear force-free fields.

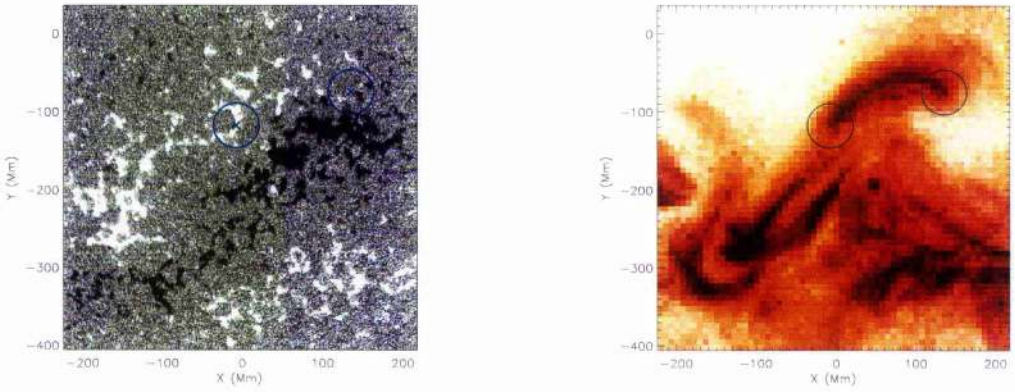

(a) (b)

Figure 3.2: (a) SOHO/MDI magnetogram and (b) *Yohkoh*/SXT image of the selected AR. Both footpoint areas (blue circles) are selected.

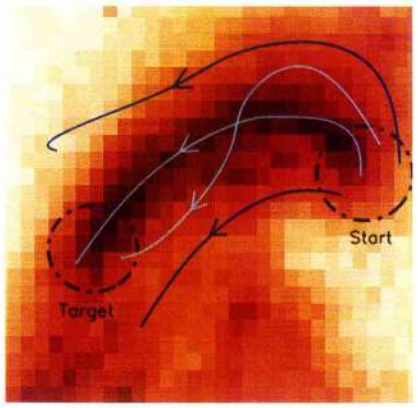

Figure 3.3: Four simulated field lines beginning at the starting footpoint area are shown. Acceptable field lines (light blue) and unacceptable field lines (dark blue) are shown.

Step 4. Calculate a set of field lines: The starting points for the field line calculations are spread over both footpoint areas. Each field line equation is integrated, from a starting point until the field line either returns to the photosphere or leaves the region of interest. If a field line starts in one of the footpoint areas and ends inside the other, it is accepted, otherwise it is rejected. Consequently, only the field lines that go from one footpoint area to the other will be used. This is illustrated in Figure 3.3, where four simulated field lines are plotted over the loop image, the selected field lines (light blue) will always connect both footpoint areas. However, while the end points may be correct, the shape of the field lines may be entirely different from the shape of the loop. It is the object of this chapter

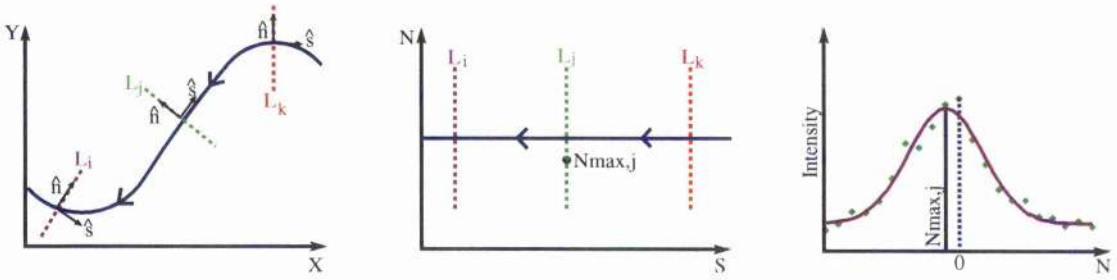

(a) (b) (c)

Figure 3.4: (a) The original field line in photospheric coordinates. (b) The straightened out field line acts as a coordinate measuring the distance from one footpoint. (c) The intensity normal to this line is shown.

to determine the quality of the field line fit, by calculating a measure of how well the field lines fit the observations.

Step 5. For each field line, calculate the deviation between the field line and the observed intensity pattern, $C_i(\alpha)$: This method is illustrated in Figure 3.4. A two dimensional coordinate system is chosen that uses the distance along the field line as one of the coordinates and the distance perpendicular to the field line as the other (shown in Figure 3.4(b)). In this manner the field line is 'uncurled' or straightened out. The effect is to give, at each location, j, along the loop, an intensity variation perpendicular to the field, $I_j(N)$, where N is the perpendicular normal coordinate (shown in Figure 3.4(c)). This intensity profile is fitted by a Gaussian and the maximum of the Gaussian is taken as the location of the loop. This will occur at $N = N_{max,j}$. If $N_{max,j} = 0$, then the loop and the field line are at the same location. In general, $N_{max,j} \neq 0$ so that there is a discrepancy between the loop location and the field line. The standard deviation, $C_i(\alpha)$, of this difference is calculated. For the ith field line this is given by

$$C_i^2(\alpha) = \sum_{j=1}^{M} \frac{N_{max,j}^2}{(M-1)} \tag{3.1}$$

where M is the number of locations along the S coordinate.

Step 6. Calculate the overall deviation for the chosen value of α, $C(\alpha)$: The value of $C_i(\alpha)$, will vary from field line to field line. These deviations must be combined to give a measure $C(\alpha)$ for a specific value of α. In this study, both the average and the minimum values of $C_i(\alpha)$ will be calculated and compared. However,

more complex statistical methods could easily be used instead.

Step 7. Repeat the procedure for different values of α. The value of α that gives the overall global minimum of C provides the best fit to that particular observed loop.

3.3 Application to linear force-free coronal loops

The procedure is illustrated using an example to fit linear force-free fields to *Yohkoh*/SXT images of coronal loops. In this case the parameter α is the linear force-free constant determining the amount of non-potential current in the system.

The *linear force-free field* case has already been discussed in Section 2.2.2. It is likely that the actual coronal magnetic field will not be a linear force-free field but this approximation provides a simple illustration of the proposed field line fitting method.

Assuming that the region of study is near the disk centre, and ignoring the photospheric curvature, a Cartesian system of coordinates is used. In Appendix A the magnetic field is obtained in terms of the Green's function for Cartesian coordinates.

For the purpose of this study, the arbitrary function $H(x, y)$ of Equation (2.11) is set equal to zero everywhere. The assumption that varying the choice of α gives sufficient freedom to obtain a qualitative match to the real field is often made in the literature (e.g., Lothian and Browning (1995)), and it is equivalent to setting $\partial B_z/\partial z = 0$ everywhere on the boundary except at the sources of **B**, where it is fixed by the strength of the source.

The magnetic field is calculated by numerical integration over B_z at the simplest level: summation of blocks, where each pixel in the magnetogram is a point source (delta function). Also, the field lines have been calculated in parallel using a fourth-order Runge-Kutta scheme with an adaptive stepsize algorithm. More information about this method can be found in Appendix B.

The data used in this example corresponds to an AR studied by Glover et al. (2001) during three consecutive rotations. During the first and the second rotations (March and April), it dominated activity on the disk. During its third rotation two CMEs took place. This study has been done prior to the first CME during the third rotation.

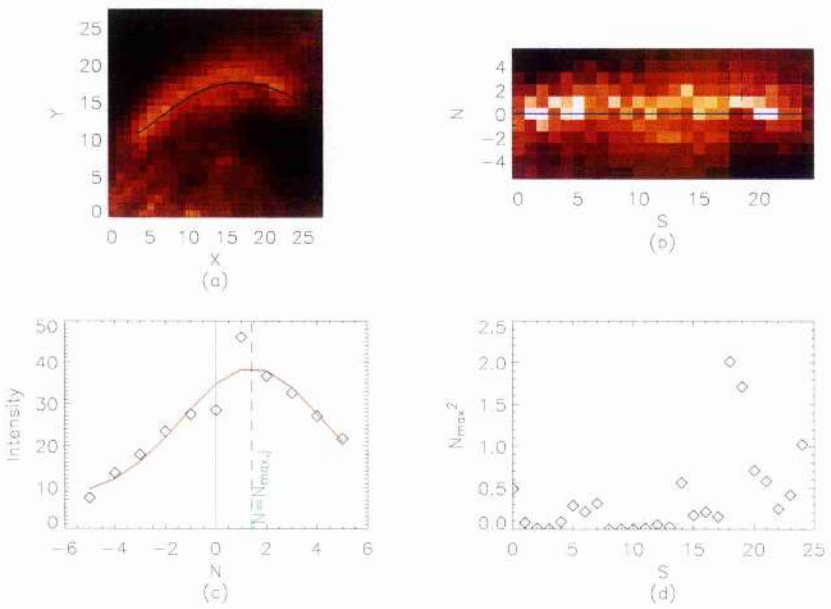

Figure 3.5: (a) The original SXT image and a superimposed acceptable field line. (b) The 'uncurled' field line and the transformed SXT image. (c) The transverse intensity profile and Gaussian fit at a chord located at S = 18, as shown in (b). (d) The difference between the field line and the intensity as a function of the distance along the loop. All the lengths on these plots (such as X, Y, S and N) are specified in pixels of the SXT image. Each pixel has a width of 7.13 Mm.

Figure 3.2 shows the entire active region and the co-aligned magnetogram of the region of interest. The example will concentrate only in the upper loop of the structure; the foot point areas are indicated in the figure as blue circles.

As discussed in Section 3.2, each of the acceptable field lines is 'straightened' out along with the corresponding SXT image (Figure 3.5), and a measure of the deviation, C, between the field line and the image is calculated. In this example, 330 field lines (acceptable and unacceptable) were calculated for each value of α; their starting points were spread evenly through both footpoint areas. For the field line shown in Figure 3.5 the value of C is 4.26 Mm, while the value of α is 0.016 Mm^{-1}.

Finally, the value of α that provides the best fit is estimated. Figure 3.6 shows $C(\alpha)$, for $\alpha \in [5, 25] \times 10^{-3}$ Mm^{-1}, plotting both the average and the minimum of C for all acceptable field lines. For α less than 8.74×10^{-3} Mm^{-1} and greater than 21.15×10^{-3} Mm^{-1}, there are no field lines that finished in the target area.

Although the variation of C is similar when considering either the minimum or the

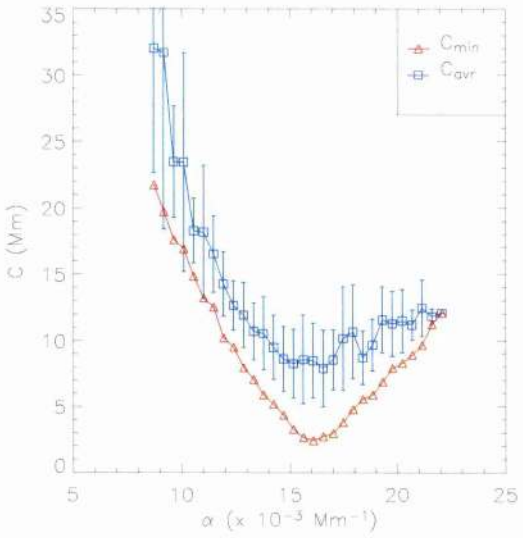

Figure 3.6: The variation of C with the value of α, showing both, the average (C_{avr}) and the minimum (C_{min}) values for all field lines. The error of C_{avr} is calculated as the mean absolute deviation.

average of all the field lines, C_{avr} fluctuates slightly near the minimum. This makes difficult to discern which value of α minimises C. It is only possible to conclude that the value of α should be somewhere between 0.015Mm^{-1} and 0.017Mm^{-1}. The result for α will then be 0.016 ± 0.001 Mm^{-1}. For such an α, $C_{min} \approx 2.80$ Mm and $C_{avr} \approx 8.35$ Mm.

The error of the parameter α has been estimated according to the width of the plot of C_{min} and C_{avr} around their minimums. Therefore, the smaller the general slope of $C(\alpha)$ its minimum, the bigger the error in α. This will be the general approach for now on. A more rigourous estimation could be to consider the error as the amount α needs to vary to produce an increment on C of a certain percentage.

For the value of α estimated with this method, some field lines have been plotted and compared with the SXT observed structures in Figure 3.7.

3.3.1 The footpoint positions for different values of α

It is interesting to notice how the footpoint position changes for different values of the parameter α. Figure 3.8 shows this effect. For each field line, its endpoints are traced. If

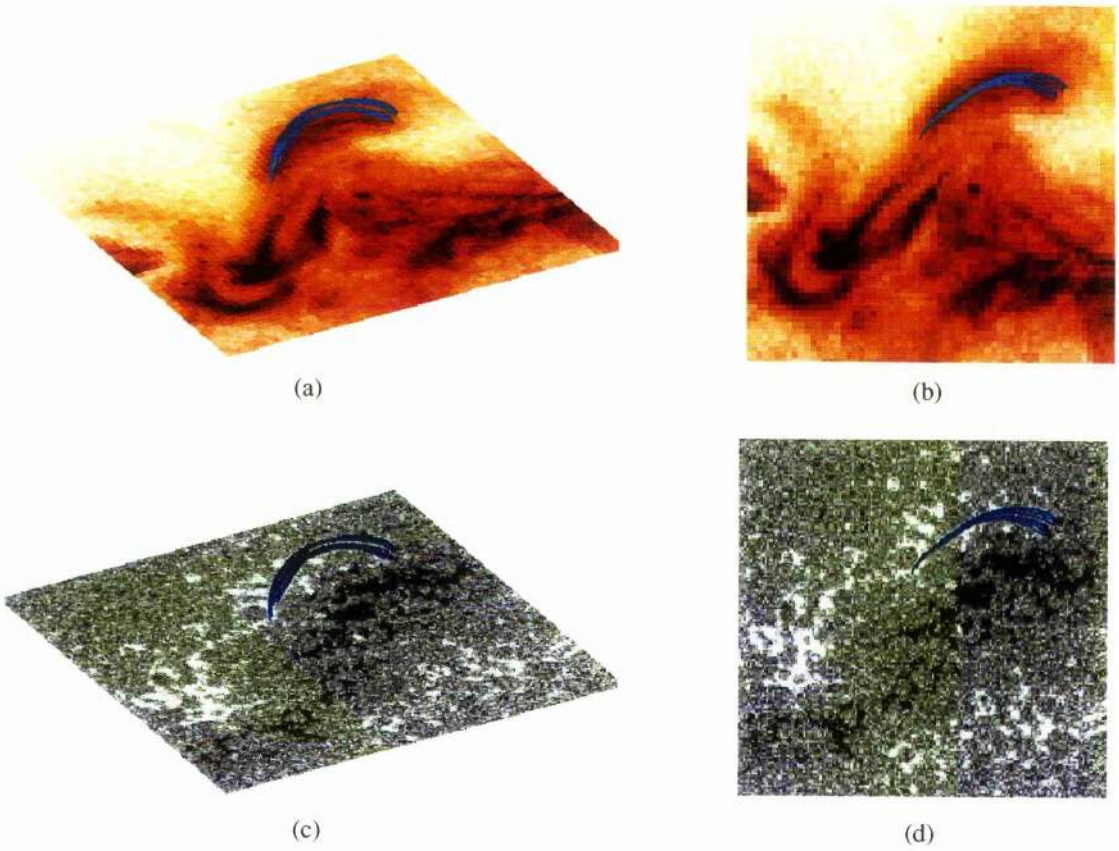

(a) (b)

(c) (d)

Figure 3.7: For the obtained value of α, a set of field lines has been plotted on top of the *Yohkoh*/SXT image ((a) and (b)) and the SOHO/MDI magnetogram ((c) and (d)).

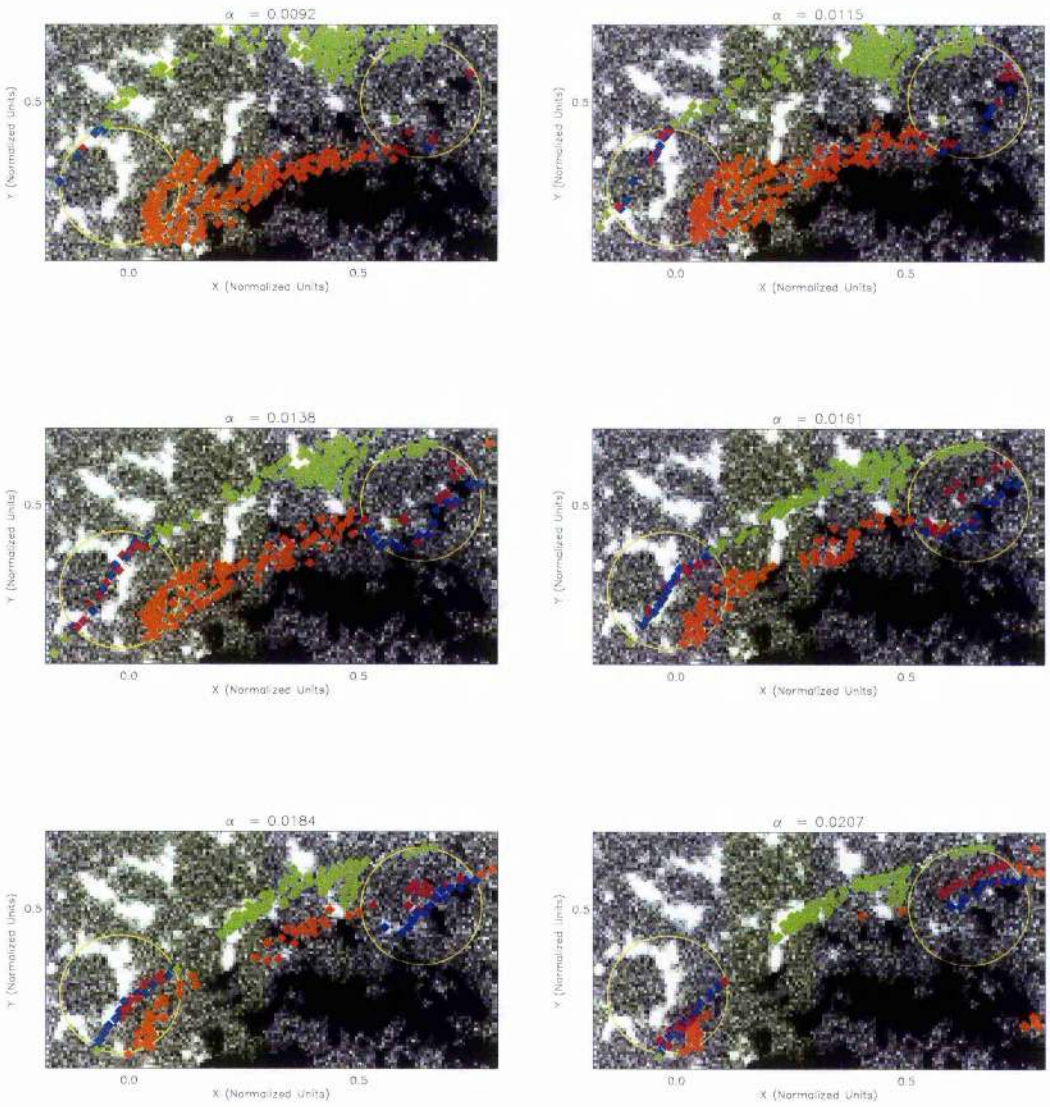

Figure 3.8: Variation of the footpoints as the parameter α changes. Blue and red dots correspond to the first and last point of the selected field lines while green and orange dots are the endpoints of the discarded field lines.

a field line connects both footpoint areas is selected and its first and last points are plotted as a blue and a red dot respectively. If the field line does not connect both footpoint areas it is discarded and its end point is plotted as a green dot if it started on the left footpoint (with main negative polarity) and as a orange dot if it started on the right footpoint (with main positive polarity).

It is interesting to see what the effect of α is in the location of all the endpoints. For small values of α the end points of the discarded field lines are located in the sources well outside the footpoints. When α is bigger the increase of the twist causes the end points to concentrate in the area between both footpoints.

On the other hand, the end points of the selected field lines, with the right connectivity, concentrate in a thin ribbon-like area all across each foot point. This "ribbon" of points varies drastically with α, moving south for the negative footpoint and north for the positive one. When α is close to optimum (the value that best reproduces the observations) the endpoints sit on top of the bigger magnetic sources in each footpoint (this effect is more dramatic for the negative source).

3.4 Some comments about this Method

The method described in Section 3.2 and applied in Section 3.3 has several limitations. Some of those can be solved by improving some of the steps.

Observations (both magnetogram and image) should be chosen as simultaneous as possible, to reduce errors in Step 1. Also the method will be more accurate when the structures are closer to the disk centre.

In Step 2, it is assumed than the studied structure is isolated and that both footpoints are included. These assumptions make the rest of the method a lot easier, but there are ways around this problem. If the studied loop is not isolated, the image can be manipulated to eliminate the extra features, although this procedure should be done with a lot of caution. One way of doing this could be to identify the area of the loop to study (using a contour plot, for example) and remove every emission outside this area. This procedure can not always be easily done.

The advantage of starting the field lines from the footpoints is that the height can be

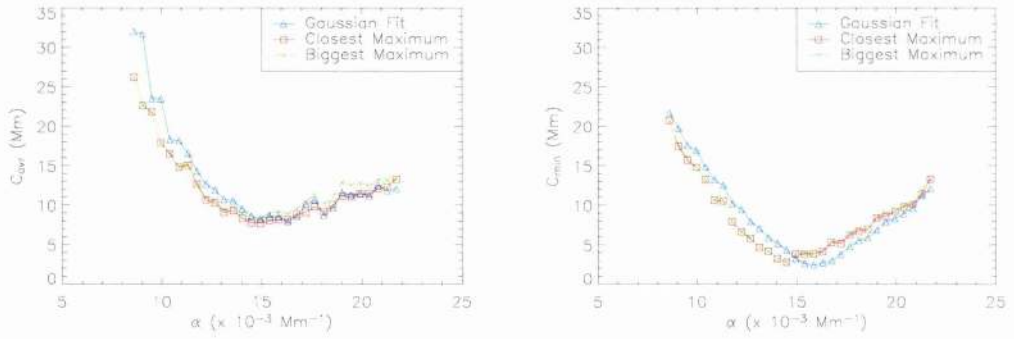

(a) (b)

Figure 3.9: Both (a) C_{avr} and (b) C_{min} for the three different methods of fitting the intensity pattern: The Gaussian fit and the quadratic fit around the biggest and the closest maximum.

easily estimated (e.g. just above the photosphere) in these areas. If the footpoints are not included in the image, field lines may be started further along the loop at some coronal height. The problem is that this height will be an extra free parameter to fit which will result in a longer computational time. Also, the way field lines are selected in Step 4 would have to be reconsidered.

Step 5 is the key of the entire method. A way to estimate quantitatively how well the theoretical field lines reproduce the observed structure is elaborated. The way the coordinates are straightened around the field line is done just to simplify the next move, where the intensity is fitted to a Gaussian.To test how much the method depends on this particular choice, other approaches were tested. Instead of a Gaussian, a quadratic expression can be fitted to the points around either the biggest maximum in the list or the closest maximum (the latter might be better when there is more than one loop in the area). The results obtained are compared to the Gaussian fit results in Figure 3.9. The overall result does not depend heavily on the function chosen for the fit, in fact there is a discernible difference only in C_{min}. The reason for this behaviour is as follows. Since this step is repeated for each point of each field line, when the field lines are sufficiently long then the fluctuation in each point cancel out when the overall value is calculated.

3.4.1 About Computational Time

All the routines included in this chapter have been implemented in IDL. Although IDL is very convenient for showing results and produce graphs, it is not the best choice for computationally intensive calculations. The computational time necessary to produce a result like the one discussed in Section 3.3 currently depends on several parameters:

- The number of field lines necessary to produce a realistic fit. The higher number of field lines the better the method will work, but it will make the computational time larger.
- The number of different values of α to study. Same as before, the smaller the step between values, the smaller the error bound in α, but this can become very computationally expensive.
- The resolution of the magnetogram. Since each pixel in the magnetogram translates as one term in the numerical integration of B_z, the higher the resolution of the magnetogram, the slower it becomes to calculate the magnetic field. Since the magnetic field has to be calculated a considerable number of times during the integration of each field line, the magnetogram resolution can become quite restrictive.

The second and third restrictions above can be made more efficient as follows. The time restrictions for the possible values of α can be improved by making the study in two steps. Firstly doing a sampling to get an estimation of where the minimum would be, afterwards a fine grid can be made around the areas where C reaches its smallest.

The restrictions in the resolution of the magnetogram can be improved by setting the pixels of the magnetogram below a certain noise threshold to 0, therefore not including these points in the calculation.

At the present the computational time is quite long, taking around two weeks to compute the necessary field lines to reproduce the result in Section 3.3. Most of this time is spent calculating the field lines for all the cases. If the field line calculation is done using a more efficient programming language (like Fortran), the overall computational time can be reduced considerably.

3.5 Discussion and Conclusions

This chapter has presented a simple technique for optimising the fit of a theoretical coronal magnetic field model to X-ray (or other coronal) observations. The method provides a set procedure for fitting the magnetic field in an objective manner, removing the subjective nature of previous methods that simply pick field lines that are similar in shape to an observed coronal loop. Here a collection of magnetic field lines are fitted by minimising the deviation between them and the intensity pattern, rather than just picking one field line and fitting it by eye.

There are seven steps in the procedure and these are described in Section 3.2. Step one consists of a proper alignment between magnetograms and coronal images.

The user has important decisions to make in step two. Here the endpoints of the coronal loop are identified by eye, from either the ends of the coronal emission or from dominant polarity sources in magnetograms. These footpoints are individually modelled by circles, whose centre and radii must be given. This step can be automated using advanced feature recognition techniques.

The remaining steps are essentially automated. The accuracy of α depends on its range and stepsize ($\delta\alpha$), bearing in mind that some values of α may produce no acceptable field lines.

The calculation of the field lines in step four, starting from the one of the photospheric footpoints, depends on the particular theoretical model being used. However, enough field lines must be calculated to be representative of the flux connectivity of the footpoints. Although the fitting procedure applies to any theoretical magnetic field model, the constant α solution is used here. It is determined as an analytical expression in terms of a Green's function solution.

Step five is the key to the field line fitting technique. A particular acceptable field line is selected and a coordinate system based on the distance along and perpendicular to this field line is constructed. The coronal image is then transformed into this coordinate system and the position of the coronal loop, in terms of the maximum of the coronal emission, is deduced. The position of the coronal loop is obtained by fitting a Gaussian curve to the coronal intensity. The square of the perpendicular distance, N^2, gives a measure of the disparity of the fit at a particular distance along the loop. The total deviation, $C_i(\alpha)$,

for this particular field line is calculated by summing the differences at each location. This is repeated for all the other acceptable field lines.

In step six, either the average of C over the acceptable field lines or the minimum C is selected for each value of α.

Finally, step seven repeats the above for different values of α and the best fit is given by the value of α that provides the global minimum C.

The method has been illustrated by using the example of a constant α, linear force free field. The only free parameter in this case is α and it is adjusted to minimise the standard deviation between the observed and calculated field lines. It is accepted that the constant α field is unlikely to be the correct model for the coronal magnetic field. However, the particular magnetic field model is not crucial to demonstrate the feasibility of the fitting technique described in this chapter.

This method can easily be extended to magnetic field models with multiple parameters, though the time taken to scan multidimensional parameter space will increase dramatically with the number of parameters. The next chapter includes an example of this approach, where the complementary part of the linear force-free field is taken into account (see Petrie and Lothian (2003)). Another possibility would be to use the method of Petrie and Neukirch (2000) with a wider class of MHD solutions depending on additional parameters.

In general, this method can be applied to more general magnetic field models. To show the advantages of this fitting approach, other data sets have been studied. In particular, the same active region is followed over a period of time and the constant α field is used to investigate how the value of α changes before and after the eruption of a coronal mass ejection.

In this chapter Yohkoh/SXT data has been used to judge the quality of the extrapolated field lines for different values of the field parameters. It should be noted that observations of the same region with different wavelength filters will outline plasma at different temperatures. It would be interesting to see whether the different observations of the same region are indeed represented by a common α in a linear force-free model, or whether the value of α varies significantly. This would provide a measure of the quality of the linear force-free model in a localised region of the corona, and would have implications on the validity of using this model to study changes in α over a period of time.

Chapter 4

Further Applications of the Magnetic Field Line Fitting of Coronal Loops

Interestingly, according to modern astronomers, space is finite.
This is a very comforting thought, particularly for people who can
never remember where they have left things.
- Woody Allen.

In Chapter 3 a method to compare theory and observations was introduced. This chapter will use that method to derive conclusions about the magnetic field in an AR.

The chapter is divided in two different parts. In the first part, the linear force-free field is used to extrapolate the magnetic field in the entire AR before and after a CME.

In the second part, the method will be illustrated when more than one parameter is needed in order to extrapolate the magnetic field.

4.1 Magnetic Field Extrapolation of AR 8906

Glover et al. (2001) followed the evolution of an active region through three rotations between March and May 2000. Table 4.1 and Figure 4.1 provide comparisons between activity associated with the region throughout the three observed rotations.

	GOES Events				*CME*
	X	*M*	*C*	*B*	*Onsets*
First Rot	0	6	67	0	10
Second Rot	0	9	39	0	9
Third Rot	0	0	0	1	2

Table 4.1: Distribution of GOES events and CME activity over three rotations.

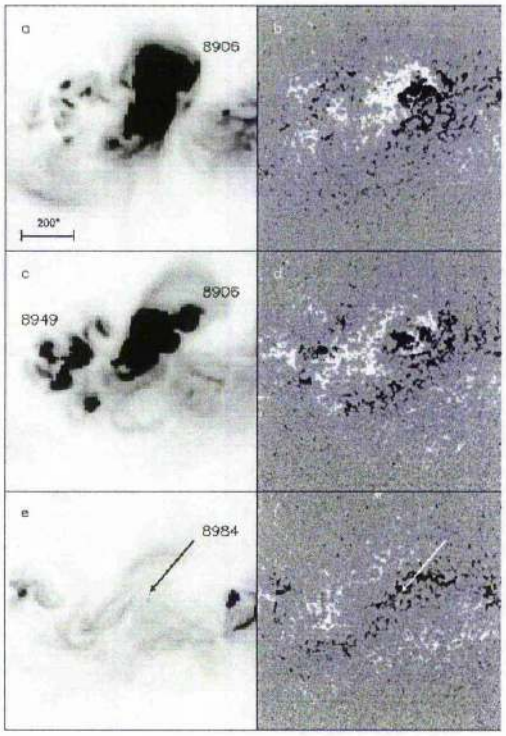

Figure 4.1: SXT and MDI observations of the region through its three rotations: 13th March (a,b), 10th April (c,d) and 7th May (e,f). Figure taken from Glover et al. (2001).

The active region was initially observed on 9 March as a highly complex area. During the first rotation (March) it dominated activity on the disk. Differential rotation reduced the field strength causing (i) the active region flux to disperse and spread out, and (ii) the formation of an extended filament channel.

During the second rotation (April), an S-shaped structure, in agreement with the hemispheric helicity rule[1] for handedness of the field, was observed to gradually fade over

[1]The Hemispheric Helicity Rule (or Hemispheric Chilarity Rule) says that magnetic fields in the northern (southern) hemisphere tend to have negative (positive) helicity. And so, coronal loops are z-shaped for the northern hemisphere and s-shaped for the southern one. The interaction between magnetic fields and both turbulent convection-zone plasmas (whose kinetic helicity depends on hemisphere) and differential solar rotation (whose direction of shear depends on the hemisphere) are likely sources of this rule.

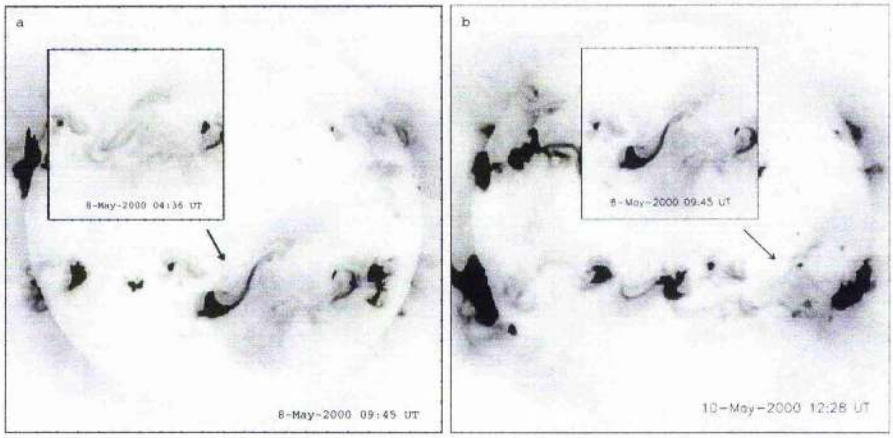

Figure 4.2: Comparison soft X-ray morphology of the region before and after the first (a) and the second CME (b). Figure taken from Glover et al. (2001).

about twelve hours. This feature connected the emerging flux at the centre of the active region and the filament channel. This phenomenon coincided with an increase in CME activity and the emergence of a second active region to the south-east, which was observed to increase in size throughout the rotation.

During the third rotation (May), a highly sheared arcade, joining the decayed remnants of two active regions on either side of the main neutral line, was observed. Very little flare activity was noticed. Two eruptions took place, the first one was a B6.8 two-ribbon flare, peaked at 06:23 8-May, the associated CME removed only part of the helicity from the filament channel. The sheared S-shaped post-flare arcade faded, until erupting again two days later. The SXR morphology before and after each eruption is showed in Figure 4.2.

In order to study how the magnetic field evolves after an eruption, the magnetic field should be followed over the AR as it evolves. During the first two rotations the AR was very active and trying to discern what produced what might be very complicated. That is why this chapter will concentrate in the development of the AR during the third and last rotation.

The following sections will extrapolate the magnetic field over AR 8906 before and after its first eruption during the third rotation. Because the AR is so near to the limb during its second eruption, magnetic field extrapolation becomes unrealistic. Magnetograms are not very accurate near the limb and the Green's function method used for the extrapolation is only accurate near the centre of the disk.

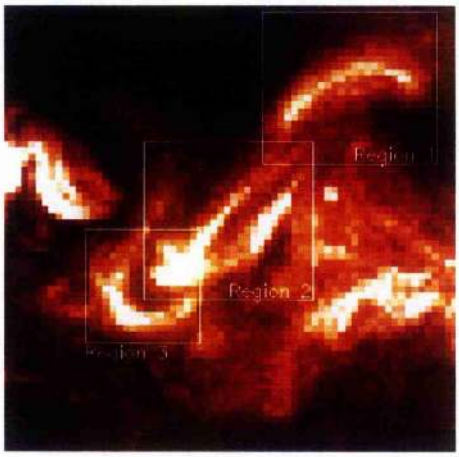

Figure 4.3: SXT image showing the three different regions the structure was divided into. Each region will be studied separately.

4.1.1 AR 8906 before the first eruption

Prior to the first eruption, AR 8906 has the morphology shown in Figure 3.2. To extrapolate the magnetic field in the area, the entire AR has been divided into three different subregions, shown in Figure 4.3. Each subregion was independently studied using the Green's Function Linear Force-free Field solution explained in Appendix A.

Region 1 has already been studied as an example and the results can be seen in Section 3.3. This region will produce the best results because it is an isolated loop. The constant α of the linear force-free field was estimated as $\alpha = 0.016 \pm 0.001$ Mm^{-1}. This value of α can reproduce a similar structure as the one observed in SXT.

In Region 2 two loops can be seen very close together. This will reduce the accuracy of the solution. Figure 4.4 shows the results for this subregion. The value of the constant α for this region is $\alpha = 0.013 \pm 0.001$ Mm^{-1}. The field lines obtained (see Figure 4.4(b)) can reproduce the top loop. Since no selected field lines seem to follow the lower structure, it is assumed the footpoint areas chosen are the ones only for the top loop.

Region 3 presents a different difficulty. Although it has only one loop on it, it twists around an area with a much higher intensity (which corresponds to the south-west area of the Region 2 loops). When field lines get close enough to this area, this high intensity can highly perturb the Gaussian fit produced during the fit, which can make the measure of C artificially low. Figure 4.5 shows the results obtained. The value of α that, according to the method used, correlates best with the observations is $\alpha = 0.012 \pm 0.002$ Mm^{-1}. It is

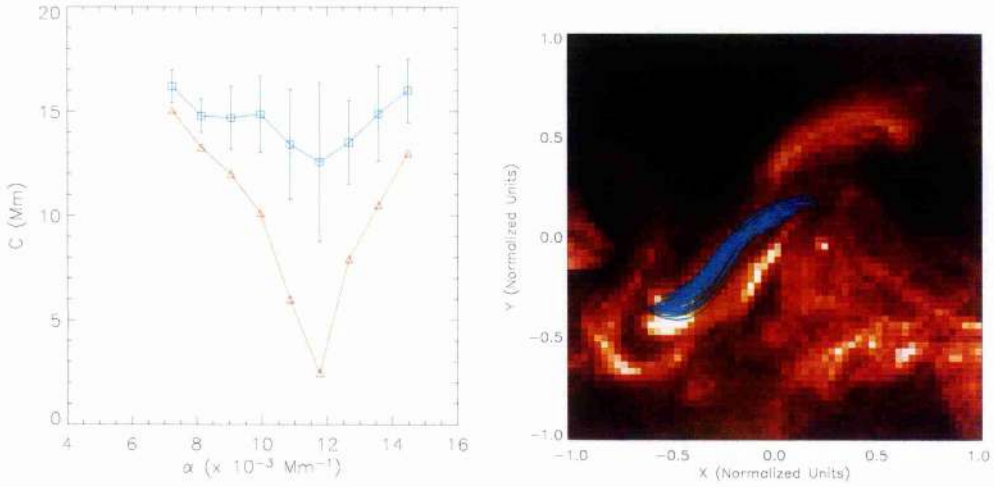

(a) (b)

Figure 4.4: Results for Region 2 before the first eruption. (a) Shows how the discrepancy C between theory and observations varies with α (C_{avr} in blue and C_{min} in red). (b) Shows a group of selected field lines for the optimal value of α.

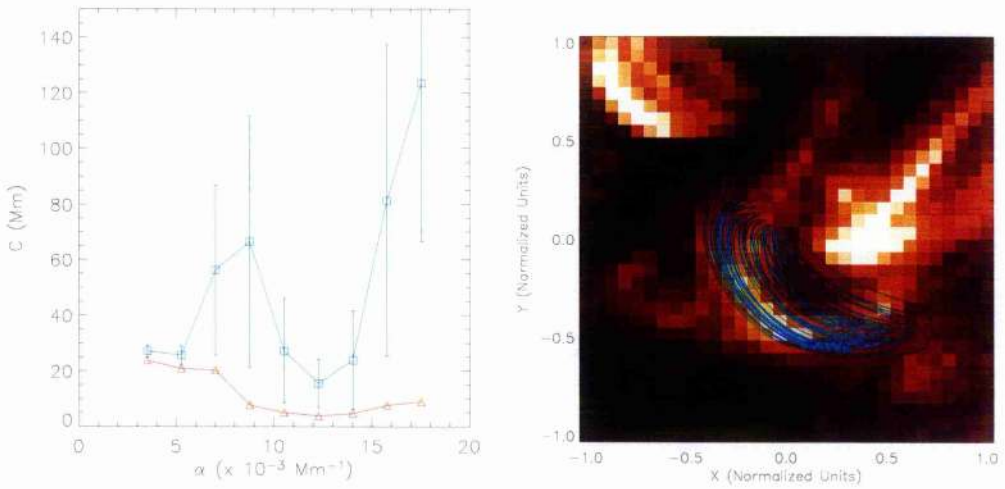

(a) (b)

Figure 4.5: Results for Region 3 before the first eruption. (a) Shows how C_{avr}, in blue, and C_{min}, in red, vary with the parameter α, (b) Shows a group of selected field lines for the optimal value of α.

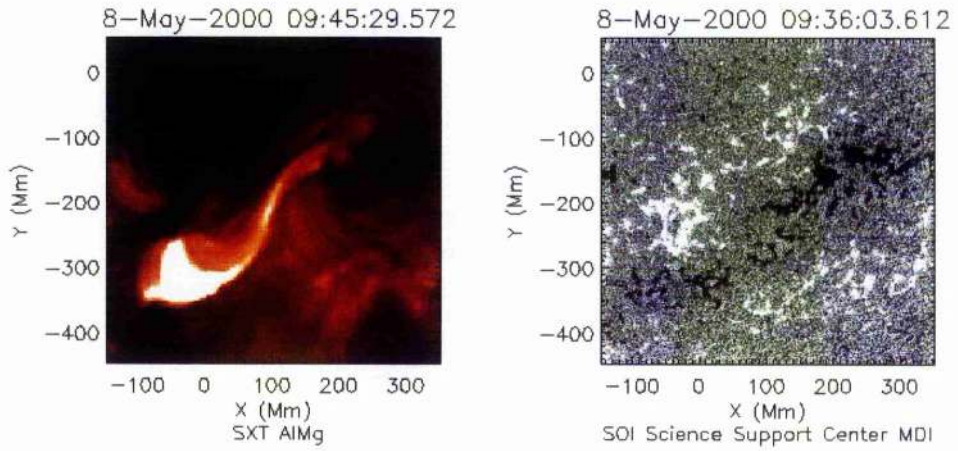

Figure 4.6: *Yohkoh*/SXT image and SOHO/MDI magnetogram of AR 8960 after the first eruption.

interesting to notice the effect of the proximity of Region 2 structures in the values of C when α is small.

In the overall AR, the magnetic field seems to be near linear force-free field with a similar value of α for Regions 2 and 3 and a slightly larger value for Region 1.

4.1.2 AR 8960 after the first eruption

Figure 4.6 shows AR 8960 shortly after its first eruption during its third and last rotation. It is interesting to point out how the AR morphology has changed. The loop observed in Region 1 has completely disappeared, while the structures in Regions 2 and 3 seemed to have joined and become brighter.

Since only one structure is observed, no subdivision is necessary and the entire AR can be extrapolated in one go. The results of this extrapolation are shown in Figure 4.7. The constant α is estimated as $\alpha = 0.014 \pm 0.002$ Mm^{-1}. This is a similar result for α as the one obtained in the same areas before the eruption. Can we conclude that α does not change? Even though the connectivity of the area appears to have changed, the coronal magnetic field does not seem to change significantly. Looking at the MDI magnetograms, the magnetic field in the photosphere does not change much either.

One thing has to be pointed out about this result. That is the high error encountered. The results for the AR after the eruption are not very conclusive. Either way, this can illustrate how the method described in Chapter 3 can be used to follow the evolution of

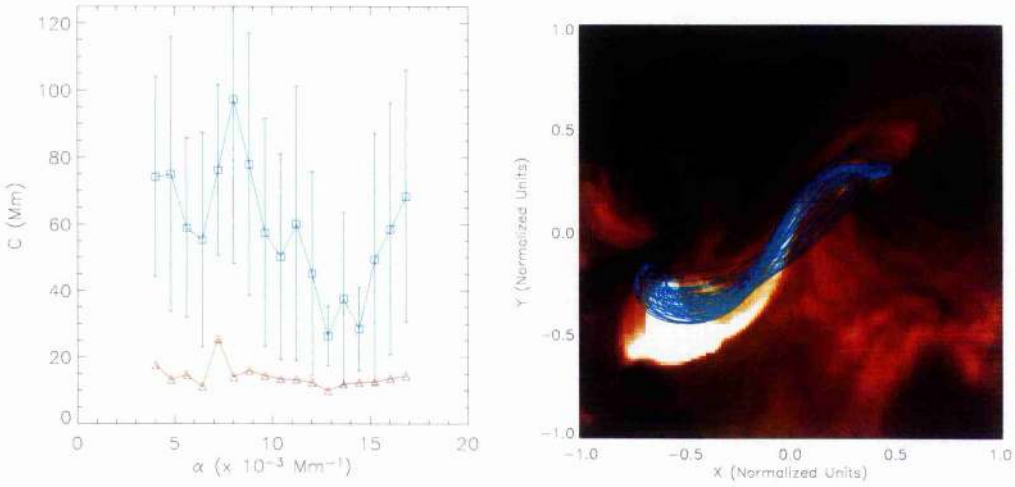

(a) (b)

Figure 4.7: Results after the first eruption. (a) Shows how C_{avr}, in blue, and C_{min}, in red, vary with α. (b) Shows a group of selected field lines for the optimal value of α.

an AR magnetic field.

4.2 Magnetic Field Line Fitting for More than One Variable

Equation (2.11) shows the general analytical solution of linear force-free magnetic field expressed in terms of the Green's function. In Sections 3.3 and 4.1 this solution has been used ignoring the complementary function $H(x, y)$. Therefore, the magnetic field had only one degree of freedom, α, the constant of proportionality between the current density and the magnetic field. In this section the method described in Chapter 3 is applied when the magnetic field depends on two different variables.

Applying the complementary function suggested by Petrie and Lothian (2003) the magnetic field becomes:

$$\mathbf{B}(x,y,z) = \frac{1}{2\pi}\int_{-\infty}^{\infty}\int_{-\infty}^{\infty}\Big[\mathbf{G}(x-x',y-y',z) + b\,\tilde{\mathbf{G}}(x-x',y-y',z)\Big] B_z(x',y',0)dx'dy'. \quad (4.1)$$

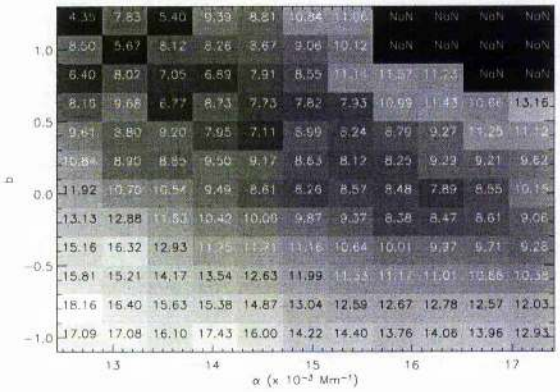

(a)

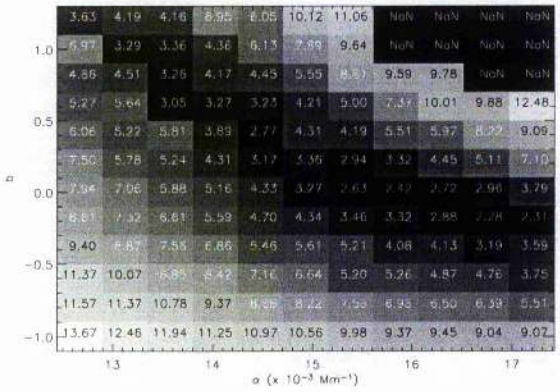

(b)

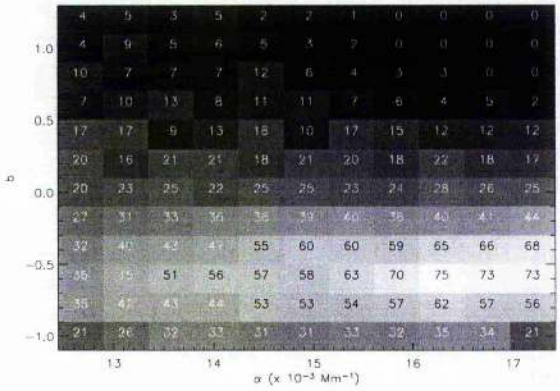

(c)

Figure 4.8: (a) C_{avr}, (b) C_{min} and (c) the number of field lines selected when both α and b are considered. Dark shades correspond to small values while light shades correspond to larger values. The numerical values are also indicated in each cell. The value "NaN" means that no field lines where selected for those cases.

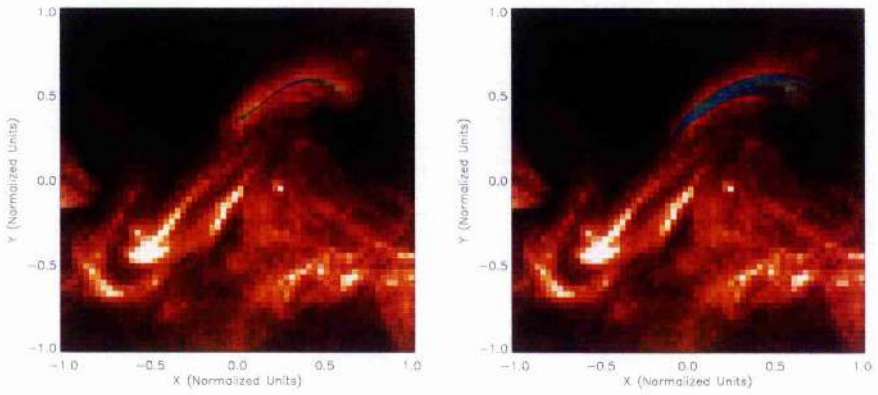

(a) $\alpha = 12.67 \times 10^{-3}$ Mm^{-1} and $b = 1.2$. (b) $\alpha = 16.74 \times 10^{-3}$ Mm^{-1} and $b = -0.2$.

Figure 4.9: Selected field lines for different values of α and b.

With this choice, the magnetic field will depend on two different parameters, α and b.

If the method described in Section 3.2 is applied under this magnetic model, the discrepancy between theory and observations will depend on both parameters so to find its minimum, a 3D plot is necessary. Figure 4.8 show the result for this magnetic model.

It is interesting to see how the number of selected field lines varies with α and b, shown in Figure 4.8(c). The row at $b = 0$ represents the number of field lines obtained in Section 3.3 and it does not seem to change much with α (between 20 and 28 lines). Since the number of field lines selected gives us an idea of the connectivity between both footpoint areas, we can conclude that varying α does not make important changes in the connectivity. The situation is very different when the b term is introduced. For big values of b, the number of field lines is small, which indicates that the connectivity between the footpoint areas is low and therefore the possibility of such a magnetic field producing a coronal loop linking both areas is small. On the other, the opposite situation is present when b is small.

Lets have look at the behaviour of C_{avr}. The horizontal line at $b = 0$ corresponds to the results studied in Section 3.3. Since a new degree of freedom is now introduced, a better fit is expected by determining the right combination of parameters. Even though C_{avr} reaches its smallest value for $b = 1.2$ and $\alpha = 0.0127$ Mm, this value has to be contrasted with the small number of field lines selected (only four field lines are selected). The selected field lines are shown in Figure 4.9(a). Although each field line follows very

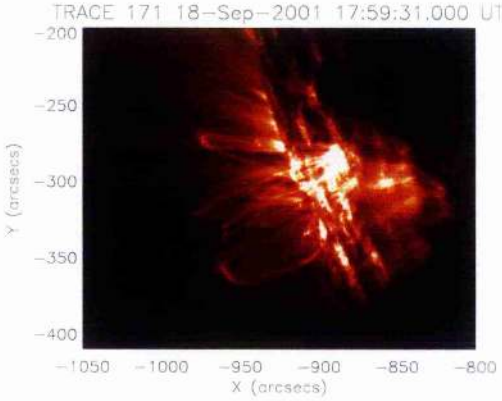

Figure 4.10: TRACE observation of a groups of loops near the limb

closely the structure found, the small amount of them that actually join both footpoint areas, makes the result less relevant.

The results for C_{min} are not very different from the ones obtained in Chapter 3. Only for a value of α slightly bigger ($\alpha = 16.74 \times 10^{-3}$ Mm^{-1}) and $b = -0.2$, a smaller value of C_{min} can be obtained. The selected field lines are plotted in Figure 4.9(b). Note also that almost twice as many field lines are selected.

It is interesting to determine the effect of b over the magnetic field line structure. As b increases, the value of α has to be decreased to compensate and retrieve a good fit. A similar result was obtained by Petrie and Lothian (2003), where the effect of the complementary Green's function seems to be the opposite of the twist produced by the original Green's function term.

4.3 Field Line Fitting Using Potential Fields

Although the magnetic potential field solution is unique and does not depend on any parameter, it is still possible to use the field line fitting method if the problem is approached from a different point of view. This section explains a possible application of the method under those circumstances.

Cirtain et al. (2005) studied an AR near the limb. A group of loops were observed in both TRACE and SOHO/CDS instruments. Figure 4.10 shows the TRACE image of the

area.

The authors were interested in finding out how far from potential the magnetic field in the area was. In order to do this, it was necessary to measure the radiative loss and to calculate the energy contained in the potential field of the AR to compare them both.

Hildner (1974) expressed the *radiative loss*[2] for optically thin radiation as

$$\delta E_R = \chi n_e^2 T^\alpha, \tag{4.2}$$

where T is the temperature, n_e is the electron number density and χ and α are empirical parameters that depend on the temperature. If the pressure, P is considered constant, the above expression can be expressed as

$$\delta E_R = \frac{P^2}{k_b^2} \chi T^{\alpha-2}. \tag{4.3}$$

Using CDS, the temperature and the density of the area can be measured and therefore the pressure can be calculated. With this data, the radiative loss can be obtained and integrated over each loop. This radiative loss can then be compared with the potential magnetic energy of the same loop to estimate how much energy must be raised from potential to account for the above radiative loss. To calculate the magnetic energy is necessary to obtain the strength of the magnetic field for each loop.

For that purpose, a potential magnetic field extrapolation was computed around the area of study. Since linear magnetograms provide the line-of-sight magnetic field, they are of no use for areas so close to the limb. Carrington synoptic magnetograms have to be used instead. This synoptic charts are assembled from individual magnetograms observed over the course of a solar rotation. The central meridional passage of all observed magnetograms are linked together to provide the photospheric magnetic field all around the Sun. The AR studied pass the meridian six days after the TRACE image was taken. Since during this time no flux emergence or flares where detected on the area, it is just necessary to correct for differential rotation. Figure 4.11 shows the result for the date of the TRACE image.

For the magnetic extrapolation, the magnetic field is assumed to be potential ($\nabla \times \mathbf{B} = 0$) with prescribed $B_r(R_\odot, \theta, \phi)$ at the photosphere and $B_\theta = B_\phi = 0$ at the source

[2]The radiative loss is the loss of energy by excited particles though the emission of photons.

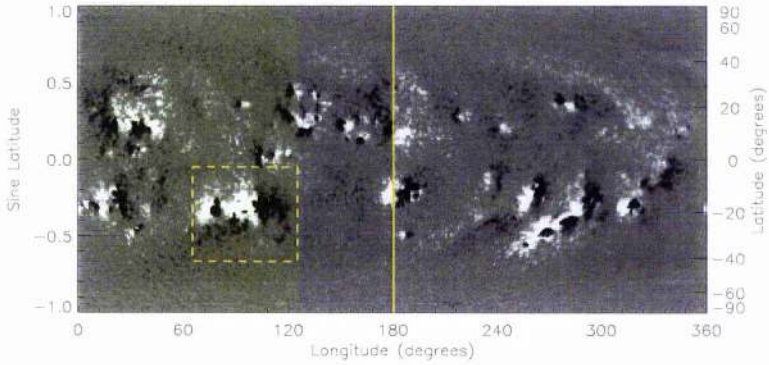

Figure 4.11: Synoptic magnetogram used to extrapolate the magnetic field into the corona. The vertical solid line shows the central meridian passage at the time when the TRACE image was taken, therefore, everything at the left of this line was measured after the selected date, while the area at the right of the line was measured before. The studied AR, located just in the limb, is enclosed by the dashed square.

surface, $r_s = 2.5R_\odot$. The magnetic field is expressed in terms of spherical harmonics; the mathematical expressions for this source surface model can be found in van Ballegooijen et al. (1998).

For each loop, it was necessary to find the field line that best fitted the shape of the loop. Assuming that the selected field line was the one followed by the plasma, the strength of the magnetic field along the loop can be assumed to be the magnetic field of the selected field line.

The method described in Chapter 3 can easily be used to determine which field line correlates best with a selected loop. For each loop, the original image was manipulated to remove the background emission. Then a set of field lines were fitted to the image and C, the parameter that measures the deviation between each field line and the observed loop, was calculated. The field line with the smallest C, was the one considered to calculate the magnetic field strength.

The method was applied in two stages. In the first one, the field line starting points formed a grid with $\delta\theta$ and $\delta\phi$ of one degree. In a second stage, the starting points are centred around the first round best fit forming a grid with $\delta\theta$ and $\delta\phi$ reduced to 0.1 degrees.

Figure 4.12 shows two loops and a group of field lines that returned the smallest value of C. The method worked very well with most of the loops studied. For the smallest loop, on the other hand, the fitting did not produce an acceptable result. This is not

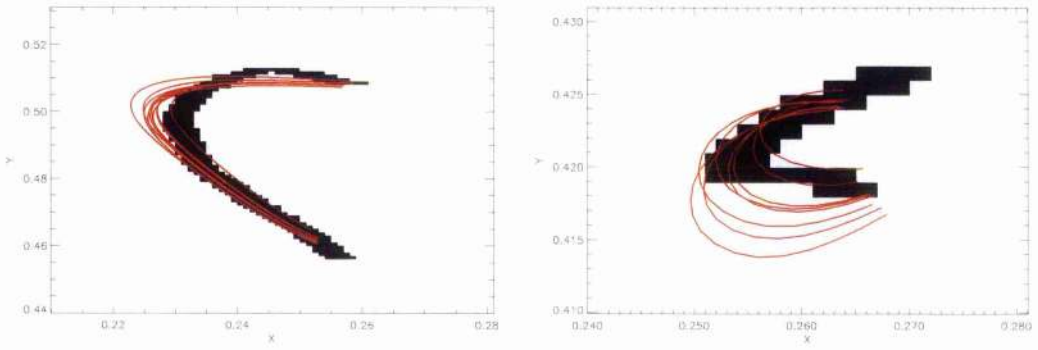

(a) (b)

Figure 4.12: Two TRACE loops (in black) and the group of field lines that produce the smallest values of C (in red). The x and y coordinates are expressed in normalised units. (a) The method works well as the loop is large enough. (b) For smaller loops the method is not as accurate.

surprising since the size of those loops where too small compared with the resolution of the magnetogram used for the extrapolation, which, therefore, limited the accuracy of the potential field.

This example shows how to use the method when three degrees of freedom are present (the coordinates of the field line starting points). The main difference is that this time each field line is compared individually instead of getting an average value as was done for the other cases.

4.4 Comments and Conclusions

This chapter has included further results obtained using the field line fitting method described in Chapter 3. The same AR was studied in more detailed and another AR was studied using potential magnetic field extrapolation.

Section 4.1 estimated the magnetic constant α, assuming linear force-free field for AR 8906 before and after its first eruption. Before the first eruption, the AR consisted of three different structures. Each of them was studied separately to obtain how α varied along the structures. The obtained values are not very far apart, which indicates that α is almost constant for the entire AR.

After the second eruption, the magnetogram doe not change drastically, although the

structure observed seems quite different. Once the magnetic extrapolation is produced, some remarks can be pointed out. It seems that, the area with the higher value of α prior to the eruption is the area that disappears after the eruption. This follows the idea that areas with more twist (and therefore a larger value of α) have a bigger probability of erupting. The remaining structure has a similar value of α as the one obtained in those areas before the eruption. It is important to point out that the error in α for this case is considerable, which can possibly indicate that the linear force-free field might not be a good approach at this stage of evolution.

Section 4.2 shows an example where the magnetic field depends on two variables. A more general linear force-free field model has been used. The results for this case are not substantially different from the results on Section 3.3, which illustrates how the linear force-free field used in Chapter 3 provides enough flexibility to fit the observed structure. It does also show how the two variables that the magnetic field depends on (α and b) are, in some way, producing an opposite effect, such that when one increases the other one has to decrease to reproduce a similar shape in the field lines. This section points out how the method would work when more than one variable is used.

In Section 4.3 the field line fitting method is used from a different point of view. An AR near the limb is studied using TRACE and CDS. In order to determine the potential energy of the system, the magnetic strength has to be evaluated. For this purpose, a series of field lines must be fitted to each observed loop. The magnetic strength for each loop is estimated as the magnetic field strength of the field line that best correlates with the observations. This example shows how the method is flexible enough to work with a magnetic field described by different variables.

Chapter 5

Approximating Non-Linear Force-Free Fields with Linear Force-Free Fields

The truth is never poor and rarely simple.
- **Oscar Wilde**, The Importance of Being Ernest, Act I (1895).

Most early models of the coronal magnetic field used the potential assumption, in which no electric currents are present. Although it might look very restrictive, its biggest advantage is that, given the line of sight magnetic field in the photosphere, it is easy to extrapolate upwards obtaining a unique coronal solution. The next simplest model is the constant α, linear force-free field. This model is a local approximation, but, how realistic is it? Three-dimensional simulations of coronal fields (Kusano et al. (1995)) show that a slowly driven field does indeed remain close to a constant α state, with energy dissipation greatly exceeding helicity dissipation, whereas other simulations find that significant non-uniformity in α persists (Dahlburg et al. (1988), and Longcope and Sudan (1992)). Clearly this is a matter of further investigation.

This chapter will examine the linear force-free field for two different geometries, and determine how they compare with more general non-linear solutions.

Section 5.1 will consider cylindrical geometry, where the photosphere consists of two parallel planes and flux tubes consist of vertical tubes connecting both planes. With the appropriate boundary conditions, the linear force-free solution for the magnetic field can be obtained. Some of its properties are studied, including its magnetic energy and helicity.

This linear force-free result will be compared with some other twist profiles.

Section 5.2 will use an arcade geometry where the photosphere is just one plane and the curvature in flux tubes is taken into account. An analytical linear force-free solution will be obtained for the translational geometry. This solution is then compared with the non-linear solution obtained by Roumeliotis (1993) in order to draw conclusions about the limitations of the linear force-free field.

5.1 Cylindrical Geometry

Observed coronal loops are toroidal in shape, as well as being long and thin structures with approximately constant cross section. To develop coronal loop models, the commonly used simplification is to restrict attention to straight cylindrical loops. The main justification of this approach is that an expansion of the toroidal force-free equation, in powers of the inverse aspect ratio, generates the straight cylinder as the leading approximation.

The study of the straight cylinder is very important since the results show that the cross-section of the loop is indeed constant over most of its length. This provides a justification for the assumption of constant cross-section when modelling toroidal loops.

Other studies have been done with this type of geometry: Parker (1979) studied twisted flux tubes constrained by external pressure. He obtained that, the twist is very large when expansion occurs and very small when severe compression is present. Browning and Priest (1983) studied an axisymmetric field with dependence on z. They found that, small twist produces expansion, but only in second order. When a high twist is present, compression decreases the twist and expansion increases it.

Zweibel and Boozer (1985) calculated the equilibrium of a thin magnetic flux tube with small twist per unit length. Their solution has a radial component concentrated near the endpoints and the energy profile is similar to earlier studies. Steinolfson and Tajima (1987) constructed a time dependent two dimensional MHD simulation when there is a continuous twisting motion on the photospheric boundary. They found that the system evolves through three different stages: in the early stage, the kinetic energy is negligible and the magnetic current and field are aligned. In the second stage, the kinetic and magnetic energy grow exponentially, but the field line structure still resembles the

one obtained by Zweibel and Boozer (1985). In the third stage both energies increase dramatically, probably due to a 3D kink instability.

Lothian and Hood (1989) investigated the shape of a magnetic flux tube when photospheric motion causes a small twist at the footpoints. Their linearised solution exhibits a boundary layer where the dependence on the axial distance is located. Outside this layer the magnetic field is essentially cylindrically symmetric. Different twisting profiles were used and they obtained solutions similar to the earlier studies.

In this section the linear force-free field solution will be calculated for the straight tube geometry. The solution will be then compared with earlier studies to determine if it can reproduce the features of other models. In Section 5.1.1 the Grad-Shafranov(-Schlüter) equation for the axisymmetric case is presented. In Section 5.1.2 this equation will be solved, ignoring the pressure term and assuming linear force-free field. The main properties of the solution are also studied in this section.

The magnetic energy and helicity expressions and their dependence on α are studied in Section 5.1.3. Section 5.1.4 compares the linear force-free field obtained with other twisting profiles used in earlier studies.

5.1.1 General Axisymmetric Case

Any axisymmetric field may be expressed in terms of the flux function A, such that

$$\mathbf{B} = \nabla A \times \nabla\theta + B_\theta\, \mathbf{e}_\theta = -\frac{1}{R}\frac{\partial A}{\partial z}\, \mathbf{e}_R + B_\theta\, \mathbf{e}_\theta + \frac{1}{R}\frac{\partial A}{\partial R}\, \mathbf{e}_z. \tag{5.1}$$

where $\mathbf{e}_R, \mathbf{e}_\theta$ and $\mathbf{e}_z$ are the unit vectors in the cylindrical coordinate system. Note that the magnetic field lines lie on surfaces of constant A. Also, the magnetic flux through a circle of radius R at constant z is simply $2\pi A(R, z)$.

The equation

$$\mathbf{B} \cdot \nabla p = 0, \tag{5.2}$$

obtained by taking the scalar product of $\mathbf{B}$ with the force balance equation,

$$\mathrm{j} \times \mathbf{B} - \nabla p = 0, \tag{5.3}$$

implies that the pressure, p, is constant along the field lines, therefore it may be expressed

as a function of the flux function: $p(R,z) = P(A(R,z))$.

The θ-component of Equation (5.3) becomes:

$$-\frac{1}{R^2}\left[\frac{\partial}{\partial R}(RB_\theta)\frac{\partial A}{\partial z} - \frac{\partial}{\partial z}(RB_\theta)\frac{\partial A}{\partial R}\right] = 0, \tag{5.4}$$

which can be written as

$$\mathbf{B}\cdot\nabla(RB_\theta) = 0. \tag{5.5}$$

As before, this means that RB_θ is a function of A. Therefore, the θ-component of the magnetic field may be expressed as

$$B_\theta = \frac{1}{R}K(A), \tag{5.6}$$

where $K(A)$ is an arbitrary function of A. This arbitrary function will be determined by the relevant boundary conditions.

The other two components of the force balance equation can be expressed as

$$\begin{aligned}-\frac{1}{\mu_0 R}\left(\frac{1}{R}\frac{\partial^2 A}{\partial z^2} + \frac{\partial}{\partial R}\left(\frac{1}{R}\frac{\partial A}{\partial R}\right) + \frac{1}{R}K(A)\frac{dK}{dA}\right)\frac{\partial A}{\partial R}\,\mathbf{e}_R \\ -\frac{1}{\mu_0 R}\left(\frac{1}{R}K(A)\frac{dK}{dA} + \frac{1}{R}\frac{\partial^2 A}{\partial z^2} + \frac{\partial}{\partial R}\left(\frac{1}{R}\frac{\partial A}{\partial R}\right)\right)\frac{\partial A}{\partial z}\,\mathbf{e}_z = \frac{dP}{dA}\nabla A,\end{aligned} \tag{5.7}$$

which reduces to

$$-\frac{1}{\mu_0 R}\left[\frac{1}{R}\frac{\partial^2 A}{\partial z^2} + \frac{\partial}{\partial R}\left(\frac{1}{R}\frac{\partial A}{\partial R}\right) + \frac{1}{R}K(A)\frac{dK}{dA}\right]\nabla A = \frac{dP}{dA}\nabla A. \tag{5.8}$$

Since all terms are in the direction of ∇A, the equation above simplifies to

$$\frac{\partial^2 A}{\partial R^2} - \frac{1}{R}\frac{\partial A}{\partial R} + \frac{\partial^2 A}{\partial z^2} + K\frac{dK}{dA} + R^2\mu_0\frac{dP}{dA} = 0, \tag{5.9}$$

which can also be expressed as

$$-\nabla\cdot\left(\frac{1}{R^2}\nabla A\right) = \mu_0\frac{dP}{dA} + \frac{1}{R^2}\,K\,\frac{dK}{dA}. \tag{5.10}$$

This equation is known as the Grad-Shafranov(-Schlüter) equation of rotational symmetry.

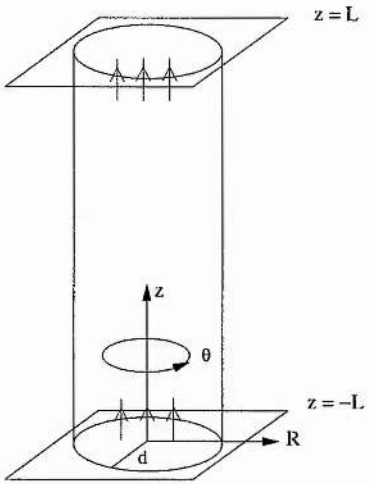

Figure 5.1: Flux tube of radius d and length $2L$. The field lines will extend from the bottom footpoint ($z = -L$) to the top one ($z = +L$).

5.1.2 The Linear Force-Free Case

The flux function and the magnetic field of an axisymmetric flux tube for the linear force-free case will be discussed in this section. The geometry of the system is shown in Figure 5.1. It consists on a rigid flux tube of radius d and length $2L$.

The system has an initially uniform magnetic field, $\mathbf{B}_{pot} = B_0\ \mathbf{e}_z$ with the magnetic flux function of the form $A_{pot} = \frac{1}{2}B_0R^2$. Later on, a twist will be introduced through the parameter α. The following boundary conditions are used:

1. The flux function at the centre is zero,

$$A(R = 0, z) = 0. \tag{5.11}$$

2. If the tube does not expand or contract, the value of A at $R = d$ does not change as the twist increases. Therefore, the condition

$$A(R = d, z) = A_{pot}(R = d, z) = \frac{B_0}{2}d^2, \tag{5.12}$$

must be satisfied.

3. Along with this, the total flux through the ends of the tube remains fixed which

means that the axial field, $B_z(R, z = \pm L)$ is the same as the potential case. Hence,

$$A(R, z = \pm L) = A_{pot}(R, z = \pm L) = \frac{B_0}{2} R^2. \tag{5.13}$$

Consider the linear force-free case, $\nabla \times \mathbf{B} = \alpha \mathbf{B}$, for which α is a constant. Using Equation (5.1) for the magnetic field, the z- and R-components become

$$\frac{dK}{dA} = \alpha, \tag{5.14}$$

therefore

$$K(A) = \alpha A + \beta. \tag{5.15}$$

The constant of integration β would give a singular B_θ as R tends to 0. In order to remove this field, due to a line current, it is necessary to impose $\beta = 0$ and $K(A) = \alpha A$.

The Grad-Shafranov(-Schlüter) equation, (5.10), becomes

$$R \frac{\partial}{\partial R} \left(\frac{1}{R} \frac{\partial A}{\partial R} \right) + \frac{\partial^2 A}{\partial z^2} + \alpha^2 A = 0. \tag{5.16}$$

This equation has a linear separable solution $A(R, z) = F(R)G(z)$, where

$$R \frac{d}{dR} \left(\frac{1}{R} \frac{dF}{dR} \right) + (\alpha^2 + k^2) F = 0, \tag{5.17}$$

$$\frac{d^2 G}{dz^2} - k^2 G = 0, \tag{5.18}$$

and k^2 is the separation constant.

For the potential case, where $\alpha = 0$ and $k = 0$, the solution becomes the initial uniform magnetic field, with

$$A_{pot,\, k=0}(R, z) = \frac{1}{2} B_0 R^2. \tag{5.19}$$

For the case $k = 0, \alpha \neq 0$, Equation (5.17) becomes

$$\frac{d^2 F}{dR^2} - \frac{1}{R} \frac{dF}{dR} + \alpha^2 F = 0, \tag{5.20}$$

which can be transformed into the Bessel's differential equation by letting $\omega = \alpha R$ and $F = \omega\Omega(\omega)$:

$$\omega^2 \frac{d^2\Omega}{d\omega^2} + \omega \frac{d\Omega}{d\omega} + (\omega^2 - 1)\Omega = 0. \tag{5.21}$$

This equation has the general solution $\Omega(\omega) = aJ_1(\omega) + bY_1(\omega)$, where a and b are constants. Since Y_1 is singular at $\omega = 0$, the constant b has to be zero, leaving

$$F(R) = \alpha R J_1(\alpha R). \tag{5.22}$$

Equation (5.18) gives $G(z) = a'z + b'$, where a' and b' are constants. Hence the flux function will be $A(R, z) = \alpha R J_1(\alpha R)(a'z + b')$. The constants a' and b' are obtained by imposing the boundary condition (5.12), the flux function takes the form:

$$A_{k=0} = \frac{d}{2} B_0 R \frac{J_1(\alpha R)}{J_1(\alpha d)}. \tag{5.23}$$

Consider $k^2 > 0$. Equation (5.17) can also be transformed into the Bessel's differential equation with solution

$$F(R) = R J_1(\sqrt{\alpha^2 + k^2} R). \tag{5.24}$$

Equation (5.18) will give the solution $G(z) = a'' \cosh(kz) + b'' \sinh(kz)$, where a'' and b'' are constants. From the symmetric boundary condition (5.13), the solution must be even with respect to z, which can only be obtained by removing the last term of G. The flux function then becomes

$$A_{k^2>0}(R, z) = R J_1(\sqrt{\alpha^2 + k^2} R) \frac{\cosh(kz)}{\cosh(kL)}. \tag{5.25}$$

The general solution will be the superposition of all the solutions in (5.23) and (5.25):

$$A(R, z) = B_0 \frac{d}{2} R \frac{J_1(\alpha R)}{J_1(\alpha d)} + \sum_{n=1}^{\infty} a_n R J_1(\sqrt{\alpha^2 + k_n^2} R) \frac{\cosh(k_n z)}{\cosh(k_n L)}. \tag{5.26}$$

To meet the boundary condition (5.12), the coefficients k_n have to satisfy

$$J_1(\sqrt{\alpha^2 + k_n^2} d) = 0 \tag{5.27}$$

therefore the possible values of k_n are

$$k_n^2 = \frac{j_{1,n}^2}{d^2} - \alpha^2, \tag{5.28}$$

where $j_{i,1}, j_{i,2}, \ldots$ denote the positive zeros of $J_i(z)$ arranged in ascending order.

Boundary condition (5.13) is used to obtain the coefficients a_n:

$$B_0 \frac{1}{2} R^2 = B_0 \frac{d}{2} R \frac{J_1(\alpha R)}{J_1(\alpha d)} + \sum_{n=1}^{\infty} a_n R J_1(\sqrt{\alpha^2 + k_n^2} R). \tag{5.29}$$

Letting $t = R/d$, $t \in (0, 1)$, and rearranging terms, the above equation takes the form

$$B_0 \frac{1}{2} d \left(t - \frac{J_1(\alpha t d)}{J_1(\alpha d)} \right) = \sum_{n=1}^{\infty} a_n J_1(j_{1,n} t), \tag{5.30}$$

which is the *Fourier-Bessel expansion* of the function

$$f(t) = B_0 \frac{1}{2} d \left(t - \frac{J_1(\alpha t d)}{J_1(\alpha d)} \right). \tag{5.31}$$

The terms a_n of the expansion will satisfy

$$a_n = \frac{B_0 d}{J_2^2(j_{1,n})} \int_0^1 t \left(t - \frac{J_1(\alpha t d)}{J_1(\alpha d)} \right) J_1(j_{1,n} t) dt. \tag{5.32}$$

A treatise on the Fourier-Bessel expansion can be found in Watson (1995a).

Using some of the properties of the Bessel function, the integral above can be solved analytically to obtain

$$a_n = \frac{-B_0 \alpha^2 d}{k_n^2 J_2(j_{1,n}) j_{1,n}}. \tag{5.33}$$

This result is derived in Appendix C.

To summarise, for the linear force-free case, the general solution of the Grad-Shafranov (-Schlüter) equation becomes:

$$A(R, z) = B_0 \frac{d}{2} R \, \frac{J_1(\alpha R)}{J_1(\alpha d)} - \sum_{n=1}^{\infty} B_0 \frac{\alpha^2 d}{k_n^2} \, R \, \frac{J_1(j_{1,n} R/d)}{J_2(j_{1,n}) j_{1,n}} \, \frac{\cosh(k_n z)}{\cosh(k_n L)}, \tag{5.34}$$

where $k_n^2 = j_{1,n}^2/d^2 - \alpha^2$. Note that, for large values of n, $j_{1,n} \approx (n - 1/2)\pi$ and the

	$A(R,z)$	$B_R(R,z)$	$B_\theta(R,z)$	$B_z(R,z)$	Φ
$\alpha \to 0$	$\frac{1}{2}B_0R^2$	0	0	B_0	0
$R \to 0$	0	0	0	Eq. (5.43)	$\frac{1}{2}\alpha$
$R \to d$	$\frac{1}{2}B_0d^2$	0	$\frac{1}{2}B_0\alpha d$	Eq. (5.47)	
$z \to 0$	$\frac{d}{2}RB_0\frac{J_1(\alpha R)}{J_1(\alpha d)}$	0	$\frac{\alpha d}{2}B_0\frac{J_1(\alpha R)}{J_1(\alpha d)}$	$\frac{\alpha d}{2}B_0\frac{J_0(\alpha R)}{J_1(\alpha d)}$	$\frac{J_1(\alpha R)}{RJ_0(\alpha R)}$
$z \to \pm L$	$\frac{1}{2}B_0R^2$	Eq. (5.53)	$\frac{1}{2}B_0\alpha R$	B_0	$\frac{1}{2}\alpha$

Table 5.1: Special cases of the linear force-free magnetic field.

series in (5.34) converges rapidly. The magnetic field then becomes

$$B_R(R,z) = \sum_{n=1}^{\infty} B_0 \frac{\alpha^2 d}{k_n} \frac{J_1(j_{1,n}R/d)}{J_2(j_{1,n})j_{1,n}} \frac{\sinh(k_n z)}{\cosh(k_n L)}, \tag{5.35}$$

$$B_\theta(R,z) = \frac{\alpha A}{R} = B_0 \frac{\alpha d}{2} \frac{J_1(\alpha R)}{J_1(\alpha d)} - \sum_{n=1}^{\infty} B_0 \frac{\alpha^3 d}{k_n^2} \frac{J_1(j_{1,n}R/d)}{J_2(j_{1,n})j_{1,n}} \frac{\cosh(k_n z)}{\cosh(k_n L)}, \tag{5.36}$$

$$B_z(R,z) = B_0 \frac{\alpha d}{2} \frac{J_0(\alpha R)}{J_1(\alpha d)} - \sum_{n=1}^{\infty} B_0 \frac{\alpha^2}{k_n^2} \frac{J_0(j_{1,n}R/d)}{J_2(j_{1,n})} \frac{\cosh(k_n z)}{\cosh(k_n L)}. \tag{5.37}$$

The only free parameters are α, B_0, d, and L. Since coronal loops are long and thin structures, the interesting case will be when L is much bigger than d.

The twist per unit length will be

$$\Phi = \frac{1}{R}\frac{B_\theta}{B_z} = \frac{\dfrac{\alpha d}{2}\dfrac{J_1(\alpha R)}{J_1(\alpha d)} - \displaystyle\sum_{n=1}^{\infty} \dfrac{\alpha^3 d}{k_n^2} \dfrac{J_1(j_{1,n}R/d)}{J_2(j_{1,n})j_{1,n}} \dfrac{\cosh(k_n z)}{\cosh(k_n L)}}{R\left(\dfrac{\alpha d}{2}\dfrac{J_0(\alpha R)}{J_1(\alpha d)} - \displaystyle\sum_{n=1}^{\infty} \dfrac{\alpha^2}{k_n^2} \dfrac{J_0(j_{1,n}R/d)}{J_2(j_{1,n})} \dfrac{\cosh(k_n z)}{\cosh(k_n L)}\right)}. \tag{5.38}$$

Special Cases

Table 5.1 includes results for some special cases, which are discussed in the following sections.

(a) $\alpha \longrightarrow 0$: Using

$$\lim_{x\to 0} J_n(x) = \frac{x^n}{2^n n!} + O(x^{n+2}), \tag{5.39}$$

it is easy to proof that, as α tends to zero, the system tends to the uniform axial field.

(b) $R \longrightarrow 0$: It is straightforward to show that

$$\lim_{R\to 0} A(R,z) = 0, \tag{5.40}$$

$$\lim_{R\to 0} B_R(R,z) = 0, \tag{5.41}$$

$$\lim_{R\to 0} B_\theta(R,z) = 0. \tag{5.42}$$

On the other hand, using Equation (5.39), the z-component of the magnetic field becomes

$$\lim_{R\to 0} B_z(R,z) = \frac{B_0 \alpha d}{2J_1(\alpha d)} - \sum_{n=1}^{\infty} \frac{B_0 \alpha^2 d^2}{(j_{1,n}^2 - \alpha^2 d^2) J_2(j_{1,n})} \frac{\cosh(k_n z)}{\cosh(k_n L)}. \tag{5.43}$$

At the centre of the tube ($R = 0$), the magnetic field is purely vertical, and its magnitude takes values from $B_0 \alpha d/[2J_1(\alpha d)]$ at the middle plane ($z = 0$), to B_0 at the footpoints ($z = \pm L$). It also can be proved that the twist per unit length takes the value $\alpha/2$.

(c) $R \longrightarrow d$: It is straightforward to show that

$$\lim_{R\to d} A(R,z) = \frac{d^2}{2} B_0, \tag{5.44}$$

$$\lim_{R\to d} B_R(R,z) = 0, \tag{5.45}$$

$$\lim_{R\to d} B_\theta(R,z) = \frac{\alpha d}{2} B_0. \tag{5.46}$$

In addition,

$$\begin{aligned}\lim_{R\to d} B_z(R,z) &= B_0 - B_0 \frac{\alpha d}{2} \frac{J_2(\alpha d)}{J_1(\alpha d)} + \sum_{n=1}^{\infty} B_0 \frac{\alpha^2 d}{(j_{1,n}^2 - \alpha^2 d^2)} \frac{\cosh(k_n z)}{\cosh(k_n L)} \\ &= B_0 \frac{\alpha d}{2} \frac{J_0(\alpha d)}{J_1(\alpha d)} - \sum_{n=1}^{\infty} \frac{B_0 \alpha^2 d^2}{(j_{1,n}^2 - \alpha^2 d^2)} \frac{J_0(j_{1,n})}{J_2(j_{1,n})} \frac{\cosh(k_n z)}{\cosh(k_n L)}.\end{aligned} \tag{5.47}$$

Since the flux tube is considered rigid, no radial component of the magnetic field is present at the outside surface of the tube ($R = d$). The azimuthal component is con-

stant along the tube while the vertical component varies from $B_0 \alpha d J_0(\alpha d)/[2J_1(\alpha d)]$ at the mid-plane ($z = 0$) to B_0 at the footpoints ($z = \pm L$).

(d) $z \longrightarrow 0$: For this case, the $\cosh(k_n z)$ terms are much smaller than the $\cosh(k_n L)$ terms and the summations can be ignored. Hence, at the middle of the loop the flux function and the magnetic field can be estimated by

$$A(R, z \approx 0) \approx B_0 \frac{d}{2} R \frac{J_1(\alpha R)}{J_1(\alpha d)}, \tag{5.48}$$

$$B_R(R, z \approx 0) \approx 0, \tag{5.49}$$

$$B_\theta(R, z \approx 0) \approx B_0 \frac{\alpha d}{2} \frac{J_1(\alpha R)}{J_1(\alpha d)}, \tag{5.50}$$

$$B_z(R, z \approx 0) \approx B_0 \frac{\alpha d}{2} \frac{J_0(\alpha R)}{J_1(\alpha d)}. \tag{5.51}$$

(e) $z \longrightarrow \pm L$: In the footpoints, the flux function becomes the potential one, thus

$$\lim_{z \to \pm L} A(R, z) = \frac{1}{2} B_0 R^2, \tag{5.52}$$

$$\lim_{z \to \pm L} B_R(R, z) = \pm \sum_{n=1}^{\infty} B_0 \frac{\alpha^2 d}{k_n} \frac{J_1(j_{1,n} R/d)}{J_2(j_{1,n}) j_{1,n}} \tanh(k_n L), \tag{5.53}$$

$$\lim_{z \to \pm L} B_\theta(R, z) = \frac{1}{2} B_0 \alpha R, \tag{5.54}$$

$$\lim_{z \to \pm L} B_z(R, z) = B_0. \tag{5.55}$$

The range of α

The linear force-free field is always a local approximation, which translates to a limited range of the parameter α that provides a physical solution. Alissandrakis (1981) studied the linear force-free field in terms of Fourier transforms. He found that, in order to keep the energy of the system finite, he had to limit $|\alpha| < 2\pi L$, where L is the typical length scale of the system. A similar result was found by Nakagawa and Raadu (1972). Gary (1989) found the limit $|\alpha_{max}| \approx |2/R_p|$ where α is calculated by integrating the magnetic field within a circle along the neutral line in the photosphere of radius R_p. Aly (1984) studied a non-linear force-free magnetic field in an infinite domain and found that, there will be solutions when $\alpha^2 < 1/L^2$.

For this case, to keep the solutions (5.34) and (5.37) finite, $J_1(\alpha d)$ cannot vanish,

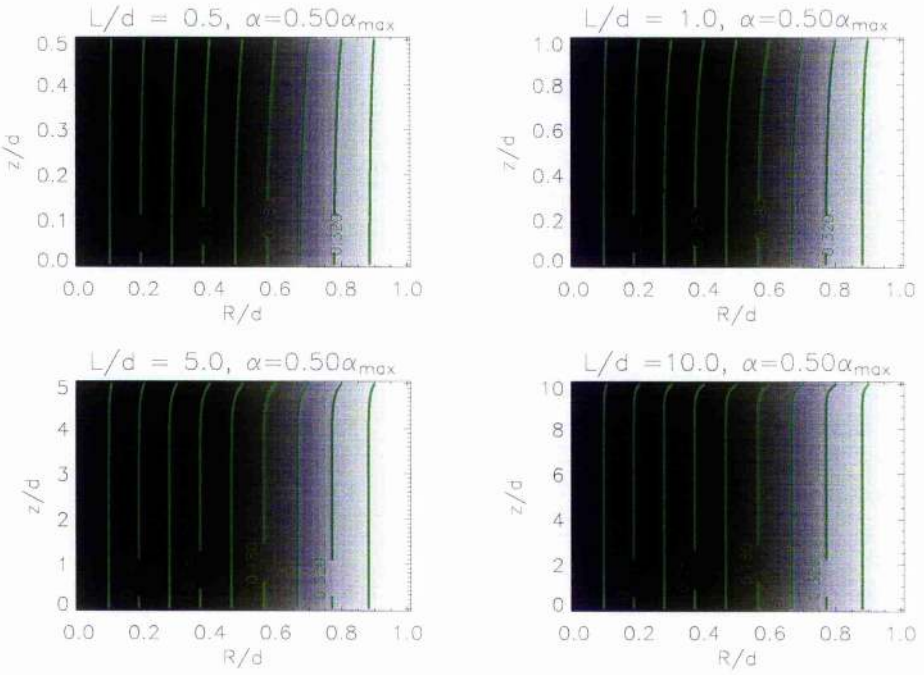

Figure 5.2: Effect of L/d on the magnetic flux function, A. Due to symmetry, only the top half of the flux tube needs to be plotted. The values of A vary from 0 (black shadow) to $\frac{1}{2}B_0 d$ (white shadow). Several contours of A have also been drawn).

which means that the possible values of α are constrained by

$$|\alpha| < j_{1,1}/d \approx \frac{3.83}{d}. \tag{5.56}$$

On the other hand, for a realistic loop model, B_z should be always positive, forcing the magnetic field lines to go from the bottom footpoint to the top one. Since $R \in [0, d]$ the maximum value of α is

$$\alpha_{max} = \frac{j_{0,1}}{d} \approx \frac{2.405}{d}. \tag{5.57}$$

Normalisation

Consider the normalisation:

$$\alpha = \bar{\alpha}\ \alpha_{max} = \frac{j_{0,1}}{d}\bar{\alpha}, \tag{5.58}$$

$$R = \bar{R}d, \tag{5.59}$$

$$z = \bar{z}L, \tag{5.60}$$

where $\bar{\alpha}$, $\bar{R}$ and $\bar{z}$ are now dimensionless. Equations (5.34)-(5.37) will become

$$A(R,z) = B_0 d^2 \left(\frac{\bar{R}}{2} \frac{J_1(j_{0,1}\bar{\alpha}\bar{R})}{J_1(j_{0,1}\bar{\alpha})} - \sum_{n=1}^{\infty} \frac{\bar{\alpha}^2 j_{0,1}^2}{\bar{k}_n^2} \bar{R} \frac{J_1(j_{1,n}\bar{R})}{J_2(j_{1,n})j_{1,n}} \frac{\cosh(\frac{L}{d}\bar{k}_n\bar{z})}{\cosh(\frac{L}{d}\bar{k}_n)} \right), \tag{5.61}$$

$$B_R(R,z) = B_0 \left(\sum_{n=1}^{\infty} \frac{\bar{\alpha}^2 j_{0,1}^2}{\bar{k}_n} \frac{J_1(j_{1,n}\bar{R})}{J_2(j_{1,n})j_{1,n}} \frac{\sinh(\frac{L}{d}\bar{k}_n\bar{z})}{\cosh(\frac{L}{d}\bar{k}_n)} \right), \tag{5.62}$$

$$B_\theta(R,z) = B_0 \bar{\alpha} j_{0,1} \left(\frac{J_1(j_{0,1}\bar{\alpha}\bar{R})}{2J_1(j_{0,1}\bar{\alpha})} - \sum_{n=1}^{\infty} \frac{\bar{\alpha}^2 j_{0,1}^2}{\bar{k}_n^2} \frac{J_1(j_{1,n}\bar{R})}{J_2(j_{1,n})j_{1,n}} \frac{\cosh(\frac{L}{d}\bar{k}_n\bar{z})}{\cosh(\frac{L}{d}\bar{k}_n)} \right), \tag{5.63}$$

$$B_z(R,z) = B_0 \left(\frac{\bar{\alpha} j_{0,1}}{2} \frac{J_0(j_{0,1}\bar{\alpha}\bar{R})}{J_1(j_{0,1}\bar{\alpha})} - \sum_{n=1}^{\infty} \frac{j_{0,1}^2 \bar{\alpha}^2}{\bar{k}_n^2} \frac{J_0(j_{1,n}\bar{R})}{J_2(j_{1,n})} \frac{\cosh(\frac{L}{d}\bar{k}_n\bar{z})}{\cosh(\frac{L}{d}\bar{k}_n)} \right), \tag{5.64}$$

where

$$k_n^2 = \frac{j_{1,n}^2}{d^2} - \bar{\alpha}^2 \frac{j_{0,1}^2}{d^2} = \frac{1}{d^2}\bar{k}_n^2. \tag{5.65}$$

It is now easy to realise that only the ratio L/d has an effect on the behaviour of the system. Figure 5.2 shows this effect, a large value of α has been chosen so the effect is more pronounced. When L and d are comparable, the isosurfaces of A (and also the field lines) will expand from the centre to the footpoints all along the tube. If L is considerably larger than d, this isosurface expansion only occurs in a small area near the footpoints. This boundary layer gets narrower as L/d gets bigger.

This kind of behaviour is common for this geometry and has been obtained in other studies, both linear, Lothian and Hood (1989) and nonlinear, Steinolfson and Tajima (1987). Lothian and Hood (1989) argued that the reason for this boundary layer to exist is that the variation that occurs on the boundary, with a scale of the loop radius, can only 'propagate' the same distance into the loop. Hence, if the loop is much longer than its radius, the main variations will occur at the boundaries and the central part of the loop will remain straight.

In terms of the currents, since the radial current density involves derivatives with respect to z, it will be localised near the footpoints, whereas the azimuthal and axial currents can penetrate through the whole loop.

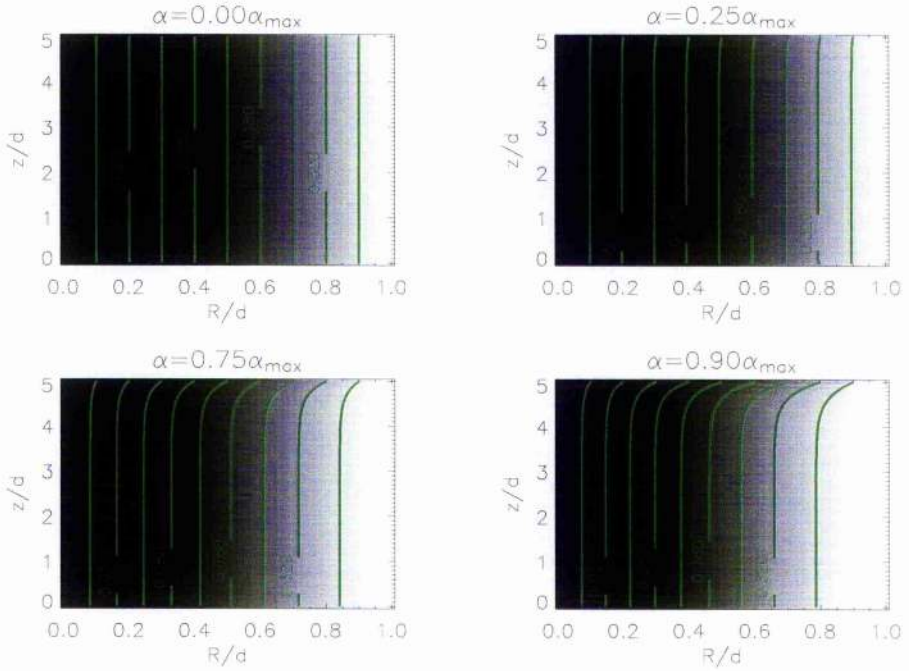

Figure 5.3: The magnetic flux function, A, for several values of α. Only the top half of the flux tube has been plotted. The values of A vary from 0 (black shadow) to $\frac{1}{2}B_0 d$ (white shadow). Several contours of A have also been drawn.

Field Line Structure

Figure 5.3 shows contours of the magnetic flux function for the particular case $L = 5d$. These contours show the magnetic field lines projected onto the $R - z$ plane. For the potential case ($\alpha = 0$), the flux function only depends on R. In fact, for every α, A is almost independent of z, except around the footpoints. As α increases, the flux function depends more strongly on z, with the rapid variation near the loop footpoints becoming more pronounced.

Figure 5.4 shows the magnetic field components for the same case as above. As well as the flux function, the magnetic field components only vary with z around the footpoints and B_R is almost negligible everywhere else.

A set of field lines, for two values of α, are shown in Figure 5.5. The starting points for the field lines have been chosen at $z = 0$ and they are equally spaced in radius. For the potential case, the field lines are just straight lines going from bottom to top. As α increases, the twist also increases and the field lines expand in the radial direction near

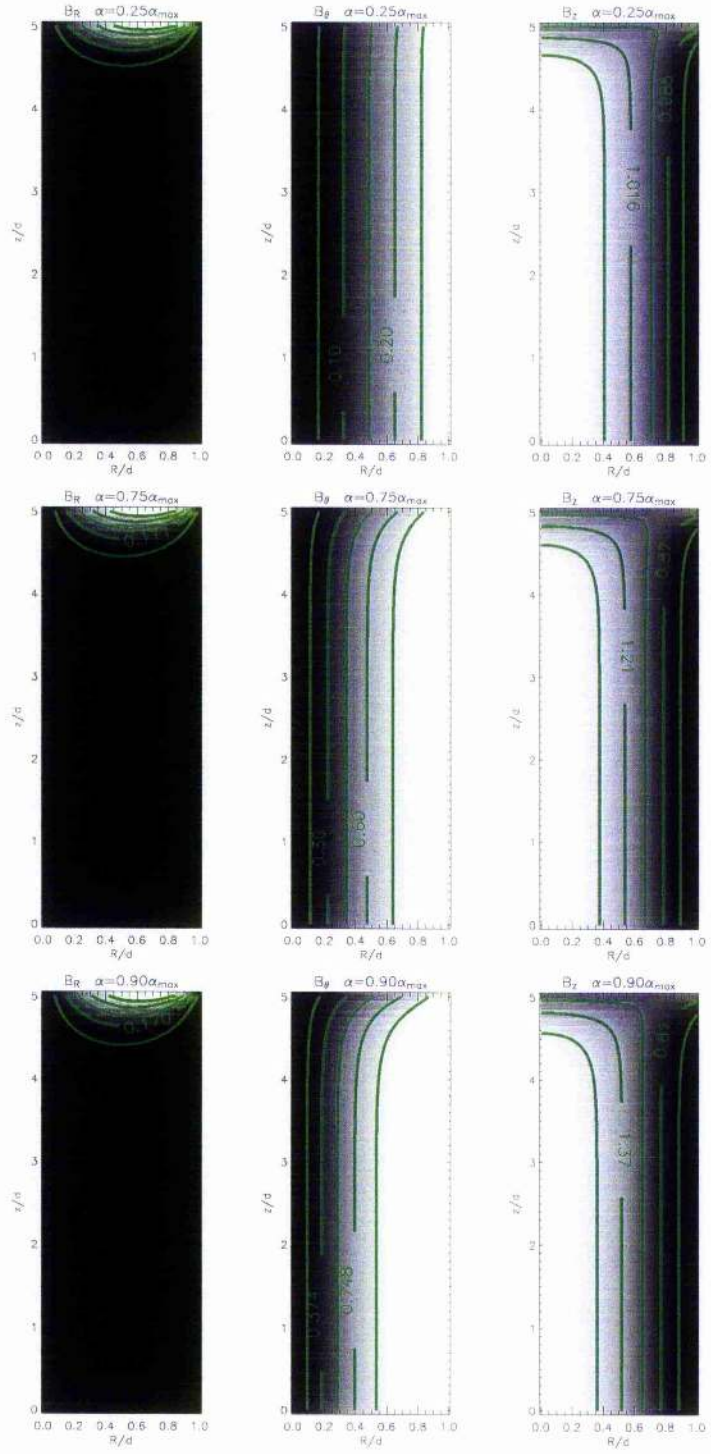

Figure 5.4: Contours of the magnetic field components for several values of α. Only the top half of the flux tube has been plotted. Dark shadows correspond to weak magnetic field, while white shadow represents strong magnetic field. Several contours have also been plotted.

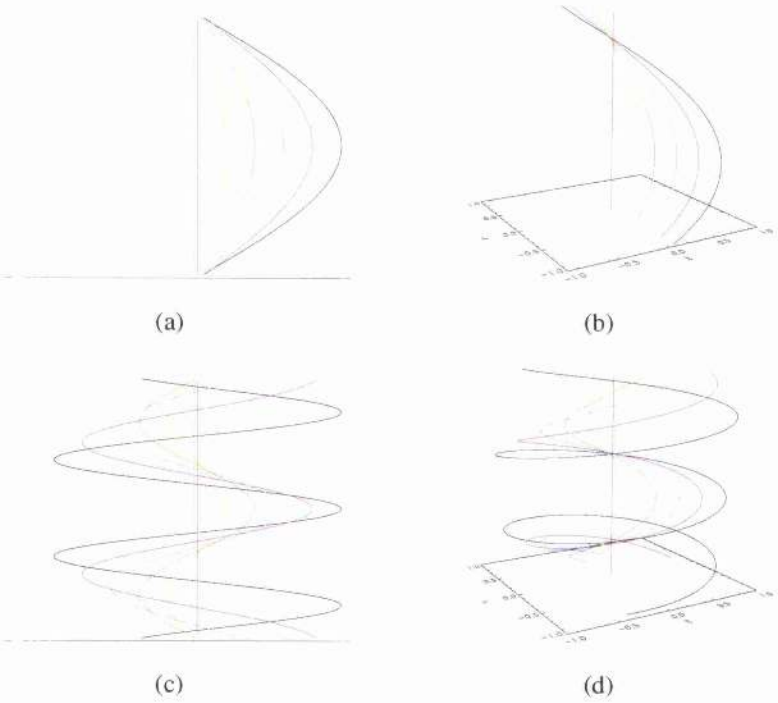

(a) (b)

(c) (d)

Figure 5.5: Field lines for two values of α. Figures (a) and (b) are two different views for $\alpha = 0.25\alpha_{max}$ and Figures (c) and (d) are two views for $\alpha = 0.75\alpha_{max}$. The bottom of each figure correspond to $z = -L = -5d$ and the top to $z = L = 5d$. Figures (a) and (c) show the field lines seen from the y-axes; in Figure (a) it appears that the field lines expand but this is actually a projection effect.

the footpoints.

In Figure 5.6 an isosurface of the flux function is shown for four different values of α. Three field lines lying on the surface are also plotted.

5.1.3 Magnetic Energy and Magnetic Helicity

In this section the magnetic energy and helicity of the tube will be calculated. The *magnetic energy* is defined as

$$W = \frac{1}{8\pi}\int_V \mathbf{B}^2 dV = \frac{1}{2}\int_0^d \int_0^L (B_R^2 + B_\theta^2 + B_z^2) R dR dz. \tag{5.66}$$

For the potential case, $\mathbf{B} = B_0\,\hat{e}_z$ and the magnetic energy will be $W_0 = B_0^2 d^2 L/4$.

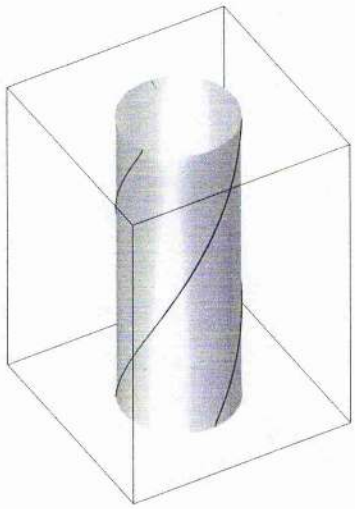

(a) $\alpha = 0.25\alpha_{max}$ and $A = 0.129B_0d^2$

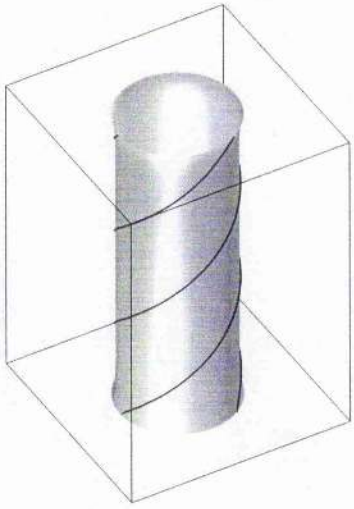

(b) $\alpha = 0.50\alpha_{max}$ and $A = 0.144B_0d^2$

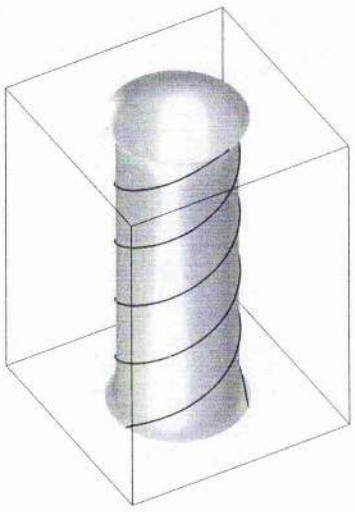

(c) $\alpha = 0.75\alpha_{max}$ and $A = 0.175B_0d^2$

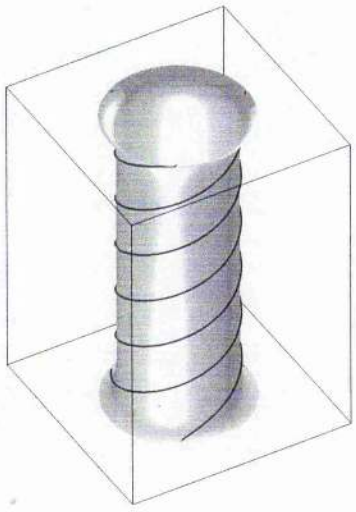

(d) $\alpha = 0.90\alpha_{max}$ and $A = 0.208B_0d^2$

Figure 5.6: Isosurfaces of the flux function, A, for different values of α. Three field lines have been plotted in each figure. The bottom of each figure correspond to $z = -L = -5d$ and the top to $z = L = 5d$.

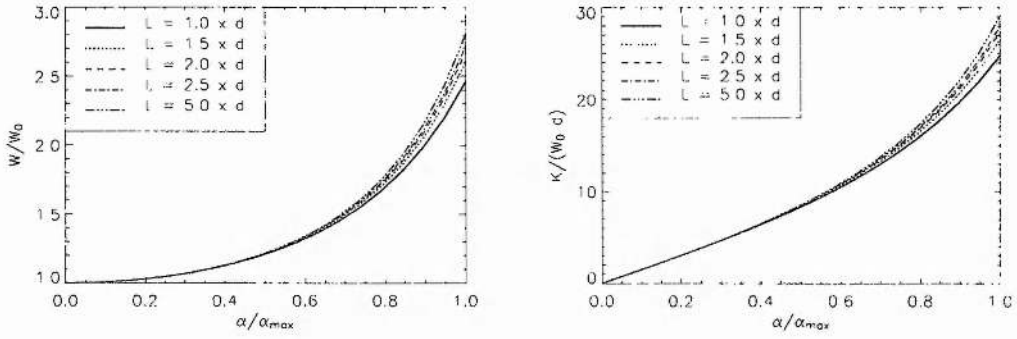

(a) (b)

Figure 5.7: Variation of (a) the magnetic energy, and (b) the magnetic helicity respect α for different values of L.

Using Equations (5.35)-(5.37) for the magnetic field, the above expression can be numerically calculated. Figure 5.7(a) shows the variation of the magnetic energy with respect to α for different values of L. It is easy to see how the magnetic energy divided by the potential energy, W_0, depends very weakly on L. This dependence is only due to the areas near the footpoints where the magnetic field depends strongly on z.

For long and thin tubes, the magnetic field is almost radial and an analytical expression for the energy can be obtained, namely:

$$W_{L>>d} = \frac{B_0^2 \alpha^2 d^2 L}{8 J_1^2(\alpha d)} \int_0^d \left(J_1^2(\alpha R) + J_0^2(\alpha R) \right) R dR$$
$$= \frac{1}{2} W_0 \alpha d \left[\alpha d \left(\frac{J_0(\alpha d)}{J_1(\alpha d)} \right)^2 - \left(\frac{J_0(\alpha d)}{J_1(\alpha d)} \right) + \alpha d \right]. \quad (5.67)$$

The *magnetic helicity* of a volume V, with boundary S and magnetic field $\mathbf{B}$ is defined as:

$$K = \int_V \mathbf{A} \cdot \mathbf{B} \, dV, \quad (5.68)$$

where $\mathbf{A}$ is the *vector potential*, such that $\mathbf{B} = \nabla \times \mathbf{A}$. For a given a magnetic field, the vector potential can be freely transformed by the *gauge transformation*: $\mathbf{A} \rightarrow \mathbf{A} + \nabla\psi$. Only when the volume V is simply connected, the above expression is gauge-invariant. Berger (1999) defined the *relative helicity* as

$$K = \int (\mathbf{A} + \mathbf{A}_P) \cdot (\mathbf{B} - \mathbf{B}_P) \, dV. \quad (5.69)$$

Where $\mathbf{B}_P$ is the unique potential field that satisfies

$$\nabla \times \mathbf{B}_P = 0 \text{ and} \tag{5.70}$$

$$\mathbf{B}_P \cdot \hat{n}|_S = \mathbf{B} \cdot \hat{n}|_S, \tag{5.71}$$

and $\mathbf{A}_P$ is its associated vector potential. The relative helicity is gauge invariant in almost any situation (the exceptions are magnetic monopole fields and periodic geometries with a mean field).

For the straight cylindrical flux tube, the potential field and its vector potential are,

$$\mathbf{B}_P = B_0 \hat{e}_z, \tag{5.72}$$

$$\mathbf{A}_P = \frac{1}{2} B_0 R \hat{e}_\theta. \tag{5.73}$$

For the linear force-free field solution obtained, it is straight forward to verify that conditions (5.70)-(5.71) hold. Therefore it is only necessary to obtain the vector potential to get the helicity. For clarity the linear force-free field will be denoted as $\mathbf{B}_\alpha$ and its associated vector potential will be $\mathbf{A}_\alpha$. $\mathbf{A}_\alpha$ is a three dimensional vector and it should not be confused with the flux function A_α which is an scalar quantity.

The vector potential of the linear force-free solution will satisfy $\nabla \times \mathbf{A}_\alpha = \mathbf{B}_\alpha$. But because of the nature of linear force-free field, $\nabla \times \mathbf{B}_\alpha = \alpha \mathbf{B}_\alpha$, therefore,

$$\mathbf{A}_\alpha = \frac{1}{\alpha}\mathbf{B}_\alpha + \nabla\psi(R,z) = \frac{1}{\alpha}\mathbf{B}_\alpha + \frac{\partial \psi}{\partial R}\hat{e}_R + \frac{\partial \psi}{\partial z}\hat{e}_z. \tag{5.74}$$

$\psi(R,z)$ will determine the gauge and, in general, can depend on α. Since, the potential field corresponds to $\alpha = 0$ it is necessary to impose,

$$\lim_{\alpha \to 0} \mathbf{A}_\alpha = \mathbf{A}_P, \tag{5.75}$$

and therefore

$$\lim_{\alpha \to 0} \frac{\partial \psi}{\partial R} = 0, \text{ and} \tag{5.76}$$

$$\lim_{\alpha \to 0} \left(\frac{\partial \psi}{\partial z} + \frac{B_0}{\alpha} \right) = 0. \tag{5.77}$$

One possible solution is giving by choosing $\psi(z) = -B_0 z/\alpha$, which gives a potential

field

$$\mathbf{A}_\alpha = \frac{1}{\alpha}\left(\mathbf{B}_\alpha - B_0\,\hat{e}_z\right). \tag{5.78}$$

Therefore,

$$(\mathbf{A}_\alpha + \mathbf{A}_P)\cdot(\mathbf{B}_\alpha - \mathbf{B}_P) = \frac{1}{\alpha}\left[B_R^2 + B_\theta^2 + \frac{\alpha}{2}B_0 B_\theta R + B_z^2 - 2B_0 B_z + B_0^2\right]. \tag{5.79}$$

Introducing the magnetic field given by Equations (5.34)-(5.37), it is easy to prove that,

$$\int_V RB_\theta dV = 2\pi B_0 d^3 L\frac{J_2(\alpha d)}{J_1(\alpha d)} - 4\pi B_0\alpha^3 d^4\sum_{n=1}^{\infty}\frac{\tanh(k_n L)}{k_n^3\, j_{1,n}^2} \quad \text{and} \tag{5.80}$$

$$\int_V B_z dV = 2\pi B_0 d^2 L. \tag{5.81}$$

Thus, the relative helicity becomes,

$$K = W_0 d\frac{8\pi}{\alpha d}\left[\frac{W_\alpha}{W_0} - \frac{\alpha d}{2}\frac{J_0(\alpha d)}{J_1(\alpha d)} - \frac{(\alpha d)^4}{(L/d)}\sum_{n=1}^{\infty}\frac{\tanh(k_n L)}{(j_{1,n}^2 - (\alpha d)^2)^{3/2} j_{1,n}^2}\right]. \tag{5.82}$$

Where W_α denotes the magnetic energy of the linear force-free field.

The summation will be neglected except when d is small compared to L. Also, when α is small, the expression simplifies to

$$K_{\alpha\sim 0} = W_0 d\frac{8\pi}{\alpha d}\left[\frac{W_\alpha}{W_0} - 1\right]. \tag{5.83}$$

Figure 5.7(b) shows the relative helicity respect α. For small values of α the helicity is approximately a straight line and it is almost independent of L. As α increases the helicity also increases, and the dependence on L becomes more noticeable. The third term of Equation (5.82) is smaller for bigger L and that is why the helicity increases with the length of the tube towards a maximum value.

5.1.4 Comparison Between Linear and Non-Linear Force-Free Field

Coronal loops tend to be very long in comparison with their widths, which corresponds to $L \gg d$. For this case, the magnetic field is almost independent of z.

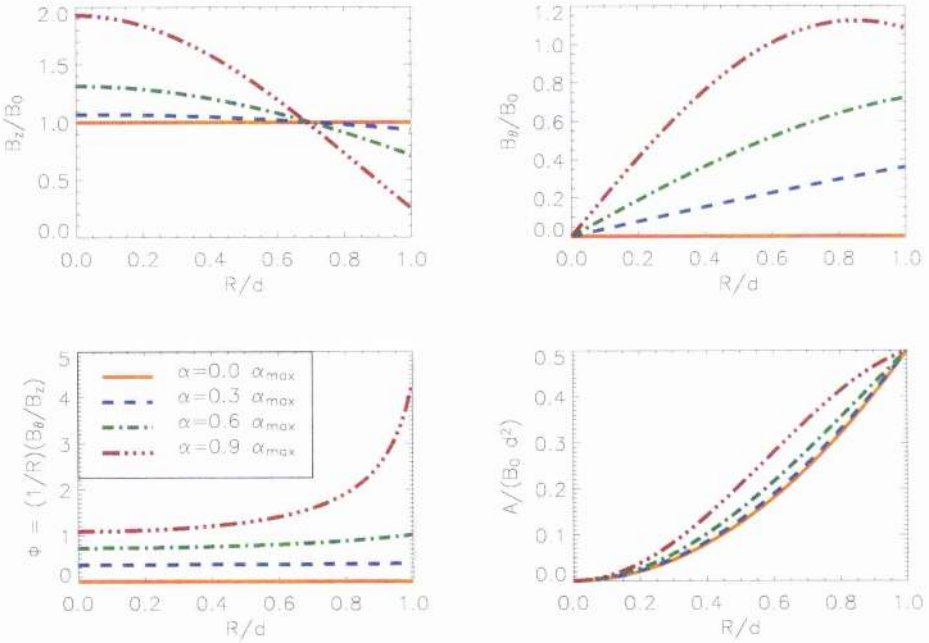

Figure 5.8: Magnetic field components, twist and magnetic flux for different values of α at $z = 0$ and $L << d$.

Linear Force-free Case

For the linear case, the solution reduces to:

$$A_L(R) = B_0 \frac{d}{2} R \frac{J_1(\alpha R)}{J_1(\alpha d)}, \tag{5.84}$$

$$B_{R_L} = 0, \tag{5.85}$$

$$B_{\theta_L}(R) = B_0 \frac{\alpha d}{2} \frac{J_1(\alpha R)}{J_1(\alpha d)}, \tag{5.86}$$

$$B_{z_L}(R) = B_0 \frac{\alpha d}{2} \frac{J_0(\alpha R)}{J_1(\alpha d)}, \tag{5.87}$$

$$\Phi_L = \frac{J_1(\alpha R)}{R J_0(\alpha R)}. \tag{5.88}$$

Figure 5.8 shows the field for several values of α. Notice how the axial flux is increased near $R = 0$ due to the magnetic tension introduced by increasing α. Since the total axial flux is conserved, this implies that B_z must be reduced near the outer edges of the loop.

General Cylindrically Symmetric Force-Free Field Case

For any cylindrically symmetric force-free field, setting,

$$B_R \approx 0, \tag{5.89}$$

$$A = A(R), \tag{5.90}$$

$$B_\theta = B_\theta(R), \tag{5.91}$$

$$B_z = B_z(R), \tag{5.92}$$

a direct relation between B_z and B_θ can be obtained from the force balance equation:

$$B_z \frac{dB_z}{dR} + \frac{B_\theta}{R}\frac{d}{dR}(RB_\theta) = 0. \tag{5.93}$$

There is only a single equation describing force balance for the two functions B_θ and B_z. Therefore, imposing one, it is possible to deduce the other and obtain the flux function. This may be used to show how the linear force-free field compares with a particular twist profile.

In general, the coronal loop will comprise of a non-linear force-free field and the aim of this section is to compare it with a linear force-free field. To do this, it is necessary to select an approximate choice of α.

In Chapter 3, a similar situation was studied but, in that case, it was necessary to compare a theoretical model with observations. In this chapter, no observations are used, but instead two different theoretical models are considered. In order to use the method proposed in Chapter 3 it will be necessary to produced some kind of observation from a general cylindrically symmetric theoretical magnetic field.

Although the method described above is feasible, it is not the easiest one. Since two theoretical magnetic field are given, it would be more straightforward to compare both directly. To do that, several possible methods for selecting α are presented below.

1. **Calculating α directly**

   (a) Either select the functional form of B_θ and deduce B_z using Equation (5.93), or select B_z and deduce B_θ.

   (b) Choose a particular radius R^* to determine the linear force-free field.

(c) Obtain an estimated α^* as the constant of proportionality between the current density and the magnetic field for $R = R^*$. Thus,

$$\alpha^* = -\frac{B_z'(R^*)}{B_\theta(R^*)} \text{ or } \alpha^* = \frac{(R^* B_\theta)'}{R^* B_z}. \tag{5.94}$$

(d) Determine the linear force-free solution for $\alpha = \alpha^*$:

$$B_{\theta_L}(R) = B_0 \frac{\alpha^* d}{2} \frac{J_1(\alpha^* R)}{J_1(\alpha^* d)}, \tag{5.95}$$

$$B_{z_L}(R) = B_0 \frac{\alpha^* d}{2} \frac{J_0(\alpha^* R)}{J_1(\alpha^* d)}, \tag{5.96}$$

$$\Phi_L = \frac{J_1(\alpha^* R)}{R J_0(\alpha^* R)}. \tag{5.97}$$

The coefficient B_0 is fixed so the magnitude of the linear and the non-linear magnetic fields coincide when $R = R^*$. Therefore:

$$B_0 = \frac{2J_1(\alpha^* d)}{\alpha^* d} \sqrt{\frac{B_\theta^2(R^*) + B_z^2(R^*)}{J_1^2(\alpha^* R^*) + J_0^2(\alpha^* R^*)}}. \tag{5.98}$$

This normalisation does not imply that both magnetic fields coincide at $R = R^*$, since they are not necessarily parallel. The only thing fixed is the constant of proportionality between the current density and the magnetic field for both cases which takes the same value.

(e) Compare the original non-linear force-free field (B_θ, B_z) with the linear force-free field (B_{θ_L}, B_{z_L}) in the neighbourhood of $R = R^*$. In this manner, conclusions can be drawn about how good a constant α field is at approximating a non-constant α field.

2. **Using the Twist to obtain α**

Instead of step 1c above, α^* is estimated through the twist. Defining

$$\Phi^* = \frac{1}{R} \frac{B_\theta(R^*)}{B_z(R^*)}, \tag{5.99}$$

in the linear case

$$\Phi^* = \frac{J_1(\alpha^* R^*)}{R^* J_0(\alpha^* R^*)} \Rightarrow \frac{J_1(\alpha^* R^*)}{J_0(\alpha^* R^*)} = R^* \Phi^*. \tag{5.100}$$

Hence α^* is determined by inverting the function

$$f(x) = \frac{J_1(x)}{J_0(x)} \Rightarrow \alpha^* = \frac{1}{R^*} f^{-1}(R^* \Phi^*). \tag{5.101}$$

This may look a little complicated, but using this approach, for $R = R^*$, the linear approximation will be aligned with the non-linear magnetic field. Therefore, applying the normalisation discussed in Equation (5.98), both magnetic fields will coincide when $R = R^*$.

3. **Average of α**

A third approach is to use the specified non-linear field, calculate α for a region and select the average value

$$< \alpha >= \frac{1}{d} \int_0^d \alpha(R) dR \qquad \text{where} \qquad \alpha(R) = -\frac{B_z'(R)}{B_\theta(R)}. \tag{5.102}$$

This method will not contribute anything new, since its results will be equivalent to case 1 where the chosen R^* in Equation (5.94) is such that α^* is equal to the average value.

Application of the methods for two different $B_\theta(R)$ profiles

To illustrate the above idea, two radial profiles have been selected for $B_\theta(R)$.

Example 1 Consider

$$B_\theta(R) = \begin{cases} B_1 d^{-3} R(d^2 - R^2) & R, \leq d, \\ 0 & R, \geq d. \end{cases} \tag{5.103}$$

This is one of the profiles used by Lothian and Hood (1989); it represents a twist within a finite radius, decreasing monotonically from $R = 0$ to $R = d$. This example

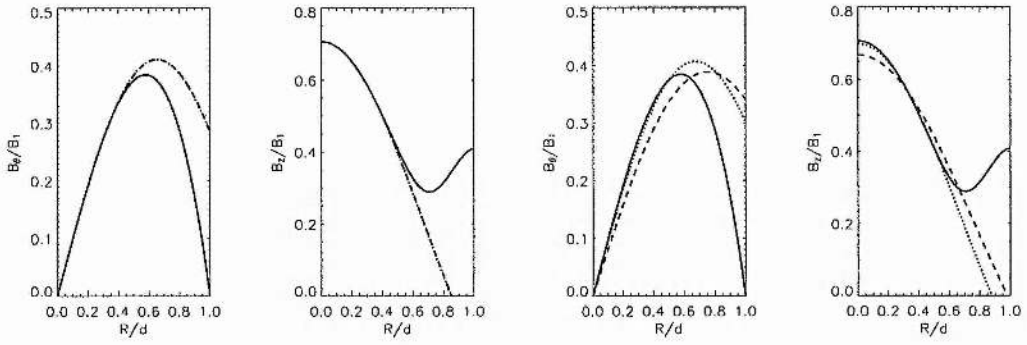

(a) $\alpha_1 = 2.815/d,\ \alpha_2 = 2.824/d$ (b) $\alpha_1 = 2.449/d,\ \alpha_2 = 2.738/d$

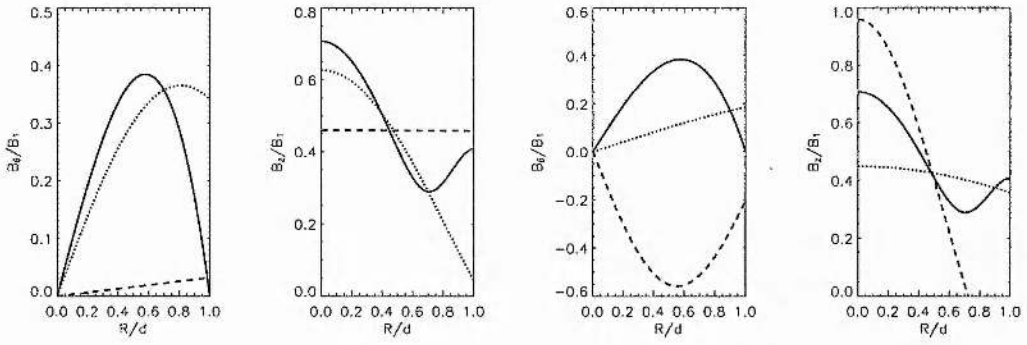

(c) $\alpha_1 = 0.138/d,\ \alpha_2 = 2.273/d$ (d) $\alpha_1 = -3.317/d,\ \alpha_2 = 0.926/d$

Figure 5.9: Specified non-linear magnetic field (solid line) and constant α field using method 1 (dashed lines) and method 2 (dotted lines) for (a) $R^* = 0.25d$, (b) $R^* = 0.50d$, (c) $R^* = 0.70d$ and (d) $R^* = 0.90d$. Each method will produce a different value of α^*, α_1 and α_2 respectively.

presents quite a severe test for choosing an approximate α. Since $B_\theta(d) = 0$, the total axial current ($2\pi \int_0^d j_z R dR$) is zero. On the other hand, for the linear force-free field, $j_z = \alpha B_z$, where B_z is positive, therefore the total axial current for the linear force-free field is non-zero.

Using Equation (5.93), B_z becomes

$$B_z^2 = -2 \int \frac{B_\theta}{R} \frac{d}{dR}(RB_\theta) dR = \frac{B_1^2}{d^6} \left[-2(d^4 R^2 + \frac{3}{2} d^2 R^4 - \frac{2}{3} R^6) + C \right]. \quad (5.104)$$

Rearranging terms, it takes the form

$$B_z^2 = B_1^2 \left[C - \left(2 \left(\frac{R}{d} \right)^2 - 3 \left(\frac{R}{d} \right)^4 + \frac{4}{3} \left(\frac{R}{d} \right)^6 \right) \right], \quad (5.105)$$

$R^*(\times d)$	$\alpha(\times 1/d)$	$B_0(\times B_1)$	$W(\times B_1^2 L d^2)$	$\delta W(\%)$	$K(\times B_1^2 L d^3)$	Method
0.25	2.815	0.2031	0.05689	8.98	0.5691	1
	2.824	0.2010	0.05673	9.24	0.5664	2
0.50	2.449	0.2778	0.05904	5.53	0.6167	1
	2.738	0.2197	0.05748	8.03	0.5837	2
0.70	0.138	0.4587	0.05272	15.56	0.0458	1
	2.273	0.3006	0.05602	10.36	0.5829	2
0.90	-3.317	0.1234	0.08697	39.16	-0.7369	1
	0.926	0.4019	0.04522	27.65	0.2532	2

Table 5.2: Comparison between both methods using Example 1.

where C is the value of B_z^2 at $R = 0$. The value of C should be adjusted to obtain a real value for B_z, by imposing $B_z^2 \geq 0$ for all R[1].

The function $f(x) = 2x^2 - 3x^4 + (4/3)x^6$ reaches is maximum where $f'(x) = 0$ and $f''(x) < 0$. It is straightforward to find that this maximum is reached when $x = 1/\sqrt{2}$ and the maximum value of $f(x)$ is $5/12$. Hence the constant of integration, C, has to be larger than $5/12$. For simplicity, the chosen value is $C = 0.5$.

The magnetic energy for this profile can be easily calculated obtaining

$$W_{Ex1} = \frac{1}{16} B_1^2 L d^2 (4C - 1) = 0.0625 B_1^2 L d^2. \tag{5.107}$$

Figure 5.9 shows the comparison of both methods, α_1 and α_2 are the values of α obtained using method 1 and 2 respectively. The approximation gives a reasonably good fit for small radius ($R \in [0, 0.5d]$), where both methods produce a similar value for the twist. Method 1 becomes less accurate near the minimum of B_z, where it gives a very small value for α, while method 2 is still reasonably good. It is important to notice that the value of α in some of the cases is actually bigger than the limit indicated in (5.57); the value of C is quite closed to the minimum, which produces a small B_z and a large twist. Increasing C will decrease the twist and reduce this effect. However, as C increases, B_z becomes more constant and looks less like the non-linear force-free field. Hence, the linear approximation becomes less accurate.

[1] In fact, this situation will occur for every magnetic field with the form

$$B_\theta(R) \propto \begin{cases} R^n (d^m - R^m)^l, & R \leq d, \\ 0, & R \geq d, \end{cases} \tag{5.106}$$

for all real numbers n, m and l.

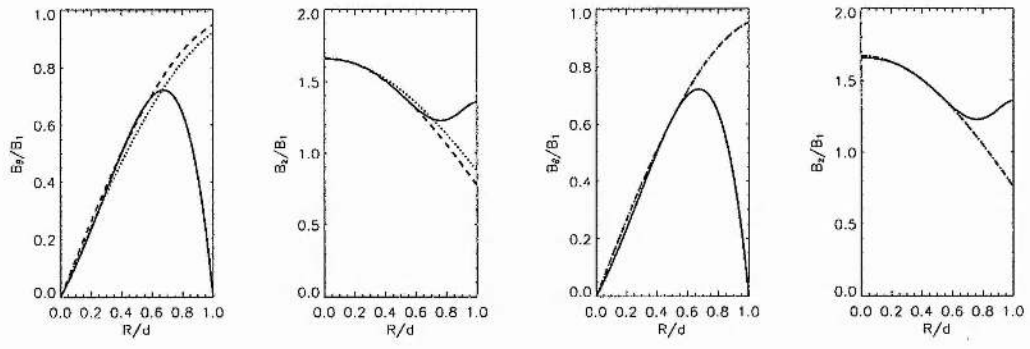

(a) $\alpha_1 = 1.587/d,\ \alpha_2 = 1.474/d$ (b) $\alpha_1 = 1.604/d,\ \alpha_2 = 1.605/d$

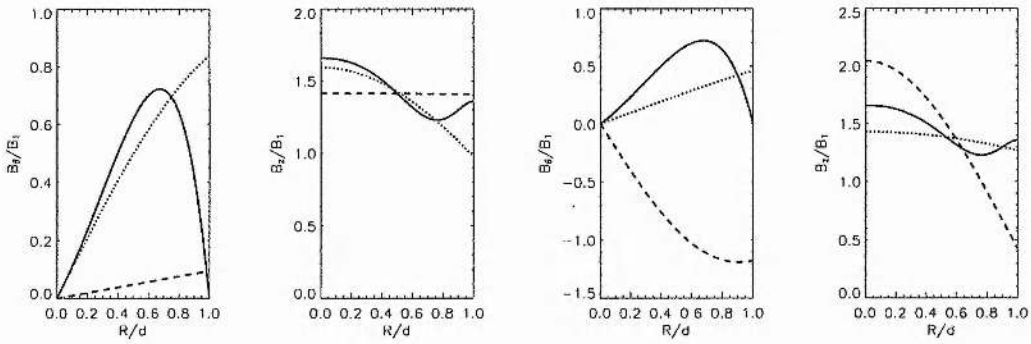

(c) $\alpha_1 = 0.135/d,\ \alpha_2 = 1.316/d$ (d) $\alpha_1 = -2.026/d,\ \alpha_2 = 0.685/d$

Figure 5.10: Specified non-linear magnetic field (solid line), constant α field using method 1 (dashed lines) and constant α field using method 2 (dotted lines) for $d = 1$ and (a)$R^* = 0.25$, (b)$R^* = 0.50$, (c)$R^* = 0.75$ and (d)$R^* = 0.90$. Each method will produce a different value of α^*, α_1 and α_2 respectively.

In this example, B_z has a local minimum for $R = d/\sqrt{2}$. For a radius bigger than that, B_z increases, which is the opposite behaviour to that found for the linear force-free field case. In fact, the first method will give a negative α, which will produce a negative B_θ. In any case, the linear force-free field cannot be a valid approximation. An example of this is shown in Figure 5.9(d).

Table 5.2 shows some results using both described methods. For the inner part of the tube, the approximated linear force-free field, using both methods, produces similar values in the magnetic energy (with discrepancies up to 10%).

$R^*(\times d)$	$\alpha(\times 1/d)$	$B_0(\times B_1)$	$W(\times B_1^2 L d^2)$	$\delta W(\%)$	$K(\times B_1^2 L d^3)$	Method
0.25	1.587	1.1936	0.51564	3.85	4.5231	1
	1.474	1.2492	0.53297	0.62	4.4320	2
0.50	1.604	1.1882	0.51591	3.80	4.5596	1
	1.605	1.1878	0.51583	3.81	4.4528	2
0.70	0.135	1.4098	0.49798	7.14	0.4210	1
	1.316	1.2725	0.51558	3.86	3.9244	2
0.90	-2.026	1.1610	0.65862	22.81	-6.6315	1
	0.685	1.3486	0.48298	9.94	2.0376	2

Table 5.3: Comparison between both methods using Example 2.

Example 2 Now consider a slightly different twist profile given by

$$B_\theta(R) = \begin{cases} B_1 d^{-3} R(d^2 - R^2)\, e^{(R/d)}, & R \leq d, \\ 0, & R \geq d, \end{cases} \tag{5.108}$$

In a similar manner to the last section, B_z can be obtained by solving Equation (5.93). For this case, ignoring constants of integration, the z component of the magnetic field becomes:

$$B_z(R) = B_1 e^{(R/d)} \left[-\left(\frac{R}{d}\right)^6 - \left(\frac{R}{d}\right)^5 + \frac{9}{2}\left(\frac{R}{d}\right)^4 - 3\left(\frac{R}{d}\right)^3 + \frac{7}{2}\left(\frac{R}{d}\right)^2 - \frac{11}{2}\frac{R}{d} + \frac{11}{4} \right]^{1/2}. \tag{5.109}$$

Also, the magnetic energy can be calculated, obtaining:

$$W_{Ex2} = \frac{3}{32} B_1^2 L d^2 (87 - 11e^2) = 0.53629 B_1^2 L d^2. \tag{5.110}$$

Figure 5.10 shows the comparison of both methods. Again, both methods produce similar results for $0 \leq R \leq d/2$, where the correlation is good. Method 2 gives a good fit up to where B_z reaches its minimum, but method 1 does not work well near the minimum, producing a very small value of α.

In this example, B_z has a local minimum for $R \approx 0.76d$. For a larger radius, B_z increases, which is the opposite behaviour to that found for the linear force-free field case. In fact, the first method will give a negative α, which will again produce a negative

B_θ, as discussed above. Method 2 will give a positive α, but no resemblance to the non-linear magnetic field can be obtained. An example of this is shown in Figure 5.10(d).

Table 5.3 shows some results using both described methods. In this case, the magnetic energy obtained with the approximated linear force-free field is even closer to the original profile one (discrepancies up to 5%).

5.1.5 Conclusions

This section has studied the linear force-free solution for the cylindrical geometry, where the photosphere is formed by two parallel planes and a flux tube will consist of a vertical tube connecting both photospheric planes.

If the tube does not expand or contract, and the total flux through the ends of the tube remains fixed, an analytical expression for the magnetic field can be obtained. This solution is almost radial all over the tube except near the footpoints, where a variation with the height, z, appears.

As α increases, the twist of the tube builds up, but, in order to acquire field lines that connect both photospheric planes, the value of α has to lie in the range $|\alpha| < j_{1,1}/d \approx 3.83/d$, where d is the radius of the tube.

This linear solution has been compared with two cylindrically symmetric twist profiles. It has been shown that the linear force-free field can reproduce a similar structure for the inner part of the tube, but the non-linear field differs strongly from the linear one as R approaches d. Similar conclusions can be drawn from the magnetic energy.

It is important to notice that, the linear force-free solution shown in Equations (5.84)-(5.88) has a very distinctive behaviour: B_z always decreases with R and B_θ has only one turning point (a maximum if α is positive or a minimum if α is negative). This property, will limit the accuracy of the linear force-free approximation, as shown in Figures 5.9(d) and 5.10(d).

5.2 Arcade Geometry

The geometry used in Section 5.1 is relevant for coronal structures that have large length-to-width ratios. To study features in the solar corona that are subjected to photospheric shearing motions another geometry has to be considered.

Because the coronal magnetic field is anchored in the photosphere, where the gas pressure is dominant over the magnetic field, the configuration of the coronal field must change as a result of photospheric motions. Thus there is considerable interest in modelling systems describing the evolution of force-free fields in response to the displacement of their magnetic footpoints. Earlier studies include Low (1977), Aly (1984), Klimchuk and Sturrock (1989), Wolfson and Verma (1991) and Roumeliotis (1993).

In Section 5.2.1 the Grad-Shafranov(-Schlüter) equation for translational symmetry will be obtained. Section 5.2.2 describes the non-linear force-free field solution developed by Roumeliotis (1993). In Section 5.2.3 the linear force-free solution is obtained assuming translational geometry and imposing Roumeliotis solution in the photosphere. The magnetic energy for both the linear and the non-linear solutions are calculated in Section 5.2.4. Section 5.2.5 compares both solutions.

5.2.1 General Translational Symmetry Case

This section will concentrate on the translational symmetry case. The approach is similar to the one followed in Section 5.1.1. The magnetic field is again expressed in terms of a magnetic flux function, A, but this time it will take the form

$$\mathbf{B} = \nabla \times (A\mathbf{e}_y) + B_y\mathbf{e}_y = -\frac{\partial A}{\partial z}\mathbf{e}_x + B_y\mathbf{e}_y + \frac{\partial A}{\partial x}\mathbf{e}_z, \tag{5.111}$$

where $\mathbf{e}_x, \mathbf{e}_y$ and $\mathbf{e}_z$ are unit vectors in the Cartesian coordinate system. With this definition,

$$\mathbf{B} \cdot \nabla A = (\nabla A \times \mathbf{e}_y) \cdot \nabla A + B_y\mathbf{e}_y \cdot \nabla A = 0, \tag{5.112}$$

which implies that magnetic field lines lie on surfaces of constant A. The pressure, p, is also constant along the field lines, and it can be expressed in terms of the flux function: $p(x, z) = P(A(x, z))$.

The current density will be

$$\begin{aligned}\mathbf{j} = \frac{1}{\mu_0}\nabla \times \mathbf{B} &= \frac{1}{\mu_0}\left[\nabla \times (\nabla \times (A\ \mathbf{e}_y)) + \nabla B_y \times\ \mathbf{e}_y\right] \\ &= \frac{1}{\mu_0}\left(-\nabla^2 A\ \mathbf{e}_y + \nabla B_y \times\ \mathbf{e}_y\right),\end{aligned} \tag{5.113}$$

and the Lorentz force will become

$$\begin{aligned}\mathbf{j} \times \mathbf{B} = \frac{1}{\mu_0}\{&-\nabla^2 A\left[\mathbf{e}_y \times (\nabla A \times\ \mathbf{e}_y) + B_y\ \mathbf{e}_y \times\ \mathbf{e}_y\right] \\ &+ (\nabla B_y \times\ \mathbf{e}_y) \times (\nabla A \times\ \mathbf{e}_y) + By(\nabla B_y \times\ \mathbf{e}_y) \times\ \mathbf{e}_y\} \\ = \frac{1}{\mu_0}\{&-\nabla^2 A \nabla A - \left[(\nabla B_y \times\ \mathbf{e}_y) \cdot \nabla A\right]\ \mathbf{e}_y - B_y \nabla B_y\}.\end{aligned} \tag{5.114}$$

The force balance equation, $\mathbf{j} \times \mathbf{B} - \nabla p = 0$, reduces to

$$-\nabla^2 A \nabla A - \left[(\nabla B_y \times\ \mathbf{e}_y) \cdot \nabla A\right]\ \mathbf{e}_y - B_y \nabla B_y = \mu_0 \frac{dP}{dA}\nabla A. \tag{5.115}$$

The y-component of the above equation becomes:

$$-(\nabla B_y \times\ \mathbf{e}_y) \cdot \nabla A = 0, \tag{5.116}$$

which can be expanded to

$$-\frac{\partial B_y}{\partial z}\frac{\partial A}{\partial x} + \frac{\partial B_y}{\partial x}\frac{\partial A}{\partial z} = 0, \tag{5.117}$$

which means that B_y is a function of the magnetic flux function ($B_y(x,z) = B_y(A(x,z))$). With this result, the component along ∇A of Equation (5.115) becomes

$$-\nabla^2 A - B_y \frac{dB_y}{dA} = \mu_0 \frac{dP}{dA}, \tag{5.118}$$

which is the Grad-Shafranov(-Schlüter) equation for translational symmetry.

5.2.2 Non-linear Force-Free Field Case: An Analytical Solution

For the general force-free field case with translational symmetry, Equation (5.118) has to be solved. Ignoring the pressure term, it can be written as

$$\frac{\partial^2 A}{\partial x^2} + \frac{\partial^2 A}{\partial z^2} + \frac{d}{dA}\left[\frac{1}{2}B_y^2(A)\right] = 0. \tag{5.119}$$

There are only a few cases for which this nonlinear elliptic equation can be solved for a given generating function, $B_y(A)$. Low (1977) showed how to construct solutions when $B_y(A) = \lambda e^A$, where λ is a free parameter. These type of solutions represent sheared bipolar arcades in which the shear depends on the parameter λ.

Roumeliotis (1993), on the other hand, constructed a set of solutions based on the assumption that the flux function has a specific nonlinear form (what he called "nonlinear separation of variables").

The solutions he found have the form

$$A(x,z) = \frac{C}{\sqrt{\lambda}}\tan^{-1}\left[\frac{f(x)g(z)}{\sqrt{\lambda}}\right], \text{ where} \tag{5.120}$$

$$\frac{1}{2}\left(\frac{df}{dx}\right)^2 = \alpha f^4 + \beta f^2 + \lambda\bar{\alpha}, \tag{5.121}$$

$$\frac{1}{2}\left(\frac{dg}{dz}\right)^2 = \bar{\alpha}g^4 + \bar{\beta}g^2 + \lambda\alpha, \text{ and} \tag{5.122}$$

$$B_y^2(A) = (\beta+\bar{\beta})\frac{C^2}{\lambda}\left[1 - \frac{1}{2}\sin^2\left(\frac{2\sqrt{\lambda}A}{C}\right)\right] + D. \tag{5.123}$$

He also presented two examples, one which is periodic in the x-direction and a second one which is periodic in both x- and z-directions. The first one will be compared with the periodic linear force-free field case.

Consider the functions

$$f(x) = \frac{1}{\cos(\pi x/2x_0)}, \tag{5.124}$$

$$g(z) = \sinh(\pi z/2z_0), \tag{5.125}$$

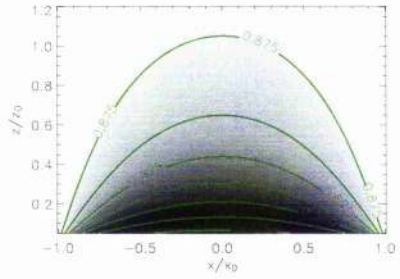

Figure 5.11: Flux function for the Roumeliotis solution, using $z_0 = 2x_0$. The shading goes from black (where the magnetic flux is zero) to white (where the magnetic flux is A_∞).

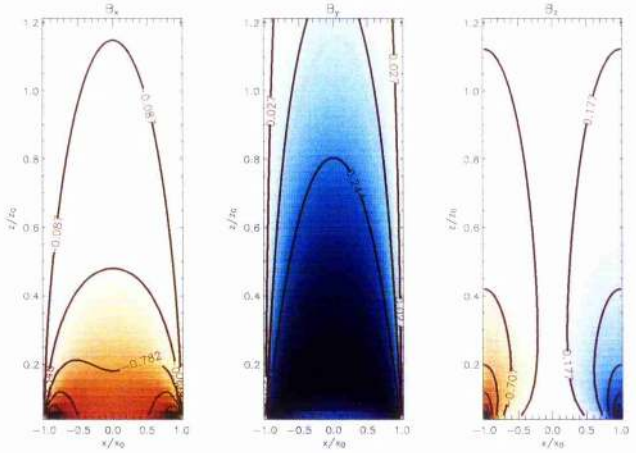

Figure 5.12: Magnetic field for the Roumeliotis solution, using $z_0 = 2x_0$. Red shading corresponds to negative values (the darker the smaller), while blue shading means positive values (the darker the bigger). White colour corresponds to zero.

which produces a field of the form

$$A^{(R)}(x,z) = \frac{2A_\infty}{\pi}\tan^{-1}\left[\frac{z_0}{x_0}\frac{\sinh(\pi z/2z_0)}{\cos(\pi x/2x_0)}\right], \tag{5.126}$$

$$B_x^{(R)}(x,z) = -\frac{A_\infty}{x_0}\left\{\frac{\dfrac{\cosh(\pi z/2z_0)}{\cos(\pi x/2x_0)}}{1+\left(\dfrac{z_0}{x_0}\right)^2\dfrac{\sinh^2(\pi z/2z_0)}{\cos^2(\pi x/2x_0)}}\right\}, \tag{5.127}$$

$$B_y^{(R)}(A) = \frac{A_\infty}{2}\left(\frac{1}{x_0^2}-\frac{1}{z_0^2}\right)^{1/2}\left|\sin\left(\frac{\pi A}{A_\infty}\right)\right|, \tag{5.128}$$

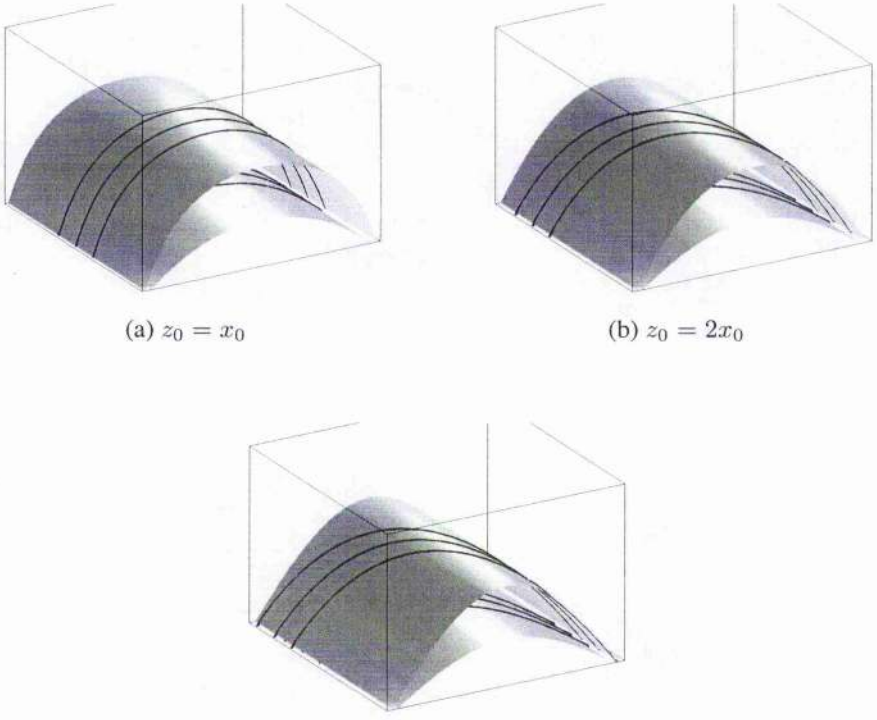

(a) $z_0 = x_0$ (b) $z_0 = 2x_0$

(c) $z_0 = 20x_0$

Figure 5.13: Isosurfaces of the flux function $A^{(R)}$, for several values of the parameter z_0. Three field lines have also been plotted over each isosurface

$$B_z^{(R)}(x,z) = A_\infty \frac{z_0}{x_0^2} \left\{ \frac{\sinh(\pi z/2z_0)\sin(\pi x/2x_0)}{1+\left(\frac{z_0}{x_0}\right)^2 \frac{\sinh^2(\pi z/2z_0)}{\cos^2(\pi x/2x_0)}} \right\}. \tag{5.129}$$

The parameters A_∞ and x_0 are fixed and the parameter z_0 can vary from x_0 to infinity. For the case $z_0 = x_0$, the magnetic field is potential, arising from an infinite set of lines sources on the plane $z = 0$. For $z_0 > x_0$ shear appears due to the displacements of the footpoints in the y-direction. It can be proved that this footpoint displacement increases smoothly with z_0, and each field line steadily expands upwards as the footpoint displacement increases.

The above solution is, in some way, nonphysical, since it has line sources at $z = 0$. To avoid this problem, the photosphere will be located at a height $z_p > 0$.

The flux function $A^{(R)}(x,z)$ and the magnetic field are shown in Figures 5.11 and 5.12, assuming $z_0 = 2x_0$. Note that, to avoid the singularities, the plots starts at $z_p = 0.1x_0$. The x-component of the magnetic field is always negative (plot in red), while the y-component is always positive (plot in blue); this implies that the field lines will go from right to left. The z-component is negative for $x < 0$, positive for $x > 0$ and it cancels for $x = 0$. Both $|B_x^{(R)}|$ and $|B_z^{(R)}|$ increase dramatically in the neighbourhood of $(x_0, 0)$.

Figure 5.13 shows the isosurfaces of the flux function for several values of z_0. It can be seen how the shear increases with z_0 and also how the field lines expand upwards when z_0 increases.

There is another interesting property to this solution. The flux function $\tilde{A}^{(R)}$ given by

$$\tilde{A}^{(R)}(x,z) = A^{(R)}(x,z) + nA_\infty, \text{ where } n \in \mathbb{Z}, \tag{5.130}$$

then

$$\tilde{B}_x^{(R)} = -\frac{\partial \tilde{A}^{(R)}}{\partial z} = -\frac{\partial A^{(R)}}{\partial z} = B_x^{(R)}, \tag{5.131}$$

$$\tilde{B}_y^{(R)} = \frac{A_\infty}{2}\left(\frac{1}{x_0^2} - \frac{1}{z_0^2}\right)^{1/2}\left|\sin\left(\frac{\pi A^{(R)}}{A_\infty} + n\pi\right)\right| = B_y^{(R)}, \tag{5.132}$$

$$\tilde{B}_z^{(R)} = \frac{\partial \tilde{A}^{(R)}}{\partial x} = \frac{\partial A^{(R)}}{\partial x} = B_z^{(R)}. \tag{5.133}$$

Therefore the magnetic field is the same when an integer times the parameter A_∞ is added. This will become quite useful when comparing this non-linear solution with the linear one discussed is Section 5.2.3.

5.2.3 The Linear Force-Free Case

In this section, the flux function and the magnetic field will be obtained for the linear force-free case in translational geometry. The geometry of the system is shown in Figure 5.14, field lines will connect both footpoint areas located in the neighbourhood of $x = x_0, z = z_p$.

The boundary conditions employed for this case are:

1. To have an isolated system, between $-x_0$ and x_0, the flux function should vanish at

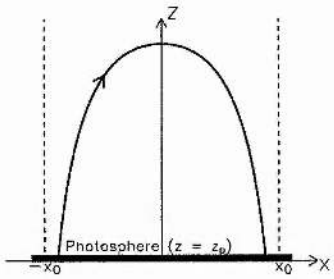

Figure 5.14: Geometry of the system for the translational case.

the boundary, hence

$$A(x = \pm x_0, z) = 0. \tag{5.134}$$

2. In order to avoid infinite magnetic energy, the flux function ought to tend to zero as z tends to infinity,

$$\lim_{z \to \infty} A(x, z) = 0. \tag{5.135}$$

3. To obtain a physical solution, no detached field lines are allowed. All field lines leave and enter the photosphere at $z = z_p$.

4. Symmetry in the x-direction will be assumed; therefore B_z should vanish at $x = 0$ and B_x should be even respect to x.

Consider the linear force-free case, $\nabla \times \mathbf{B} = \alpha \mathbf{B}$, with α constant. Using Equation (5.111) for the magnetic field, the x- and z-components will become,

$$\frac{dB_y}{dA} = \alpha, \tag{5.136}$$

thus

$$B_y = \alpha A + \beta. \tag{5.137}$$

The constant of integration, β would give a non-zero magnetic field when z tends to infinity. In order to get finite magnetic energy the condition $\beta = 0$ must be satisfied. Therefore, the y-component of the magnetic field is $B_y(A) = \alpha A$ and the Grad-Shafranov(-Schlüter) equation, ignoring the pressure term, becomes

$$-\nabla^2 A - \alpha^2 A = 0. \tag{5.138}$$

This equation has a linear separable solution $A^{(\alpha)}(x,z) = F(x)G(z)$, where

$$\frac{d^2F}{dx^2} + k^2F = 0, \tag{5.139}$$

$$\frac{d^2G}{dz^2} + (\alpha^2 - k^2)G = 0, \tag{5.140}$$

and k^2 is the separation constant.

Solving for $F(x)$

- If $k \in \mathbb{R}$, then

$$F(x) = C\cos(kx) + D\sin(kx), \tag{5.141}$$

where C and D are constants of integrations. A has to be even respect x, hence $D = 0$. The separation constant, k has a discrete set of values determined by the boundary condition (5.134), these values are

$$k_n = (2n+1)\frac{\pi}{2x_0}. \tag{5.142}$$

- If $k = i\omega$ where $\omega \in \mathbb{R}$, then

$$F(x) = C'\cosh(\omega x) + D'\sinh(\omega x), \tag{5.143}$$

where C' and D' are constants of integration. A has to be even, therefore $D' = 0$. Unfortunately, in this case, no value of ω can fulfil the boundary condition (5.134), so this is not a valid solution.

Solving for $G(z)$

- If $\sqrt{\alpha^2 - k^2} \in \mathbb{R}$, then

$$G(z) = H\cos(\sqrt{\alpha^2 - k^2}z) + I\sin(\sqrt{\alpha^2 - k^2}z), \tag{5.144}$$

where H and I are constants of integration. But this solution cannot fulfil the boundary condition (5.135), so this is not a valid case.

- If $\sqrt{k^2-\alpha^2} \in \mathbb{R}$, then

$$G(z) = H' e^{\sqrt{k^2-\alpha^2}z} + I' e^{-\sqrt{k^2-\alpha^2}z}, \tag{5.145}$$

where H' and I' are constants of integrations. Imposing condition (5.135), the constant H' should vanish.

The general solution of Equation (5.138) will be the linear combination of all possible solutions. Therefore the flux function takes the form:

$$A^{(\alpha)}(x,z) = \sum_{n=0}^{\infty} b_n \cos(k_n x) \exp\left\{-\sqrt{k_n^2-\alpha^2}z\right\}, \tag{5.146}$$

where $k_n = (2n+1)\pi/2x_0$.

Note that, again, α values have a limited range given by

$$|\alpha| \leq \alpha_{max} = \frac{\pi}{2x_0}. \tag{5.147}$$

In order to obtain the value of the coefficients b_n, another boundary condition is needed. If the flux function in the photosphere is known[2], $P(x)$, then

$$A^{(\alpha)}(x, z=z_p) = P(x) = \sum_{n=0}^{\infty} b_n \cos(k_n x) \exp\left\{-\sqrt{k_n^2-\alpha^2}z_p\right\}. \tag{5.148}$$

The right hand side is the Fourier series of the function $P(x)$ and the Fourier coefficients, b_n, can then be calculated. A treatise on Fourier series can be found in Lanczos (1966). Therefore, the flux function for any other height will be

$$A^{(\alpha)}(x,z) = \sum_{n=0}^{\infty} a_n \cos(k_n x) \exp\left\{-\sqrt{k_n^2-\alpha^2}(z-z_p)\right\}, \tag{5.149}$$

where

$$a_n = b_n \exp\left\{-\sqrt{k_n^2-\alpha^2}z_p\right\} = \frac{1}{x_0}\int_{-x_0}^{x_0} P(x)\cos(k_n x)dx. \tag{5.150}$$

[2]The height of the photosphere, z_p, is usually taken as zero. However, to compare with the analytical solution expressed in Equation (5.126), z_p is taken to be non-zero.

In order to compare this linear solution with the non-linear one discussed on Section 5.2.2, the latter will be used to provide the boundary condition on the photosphere. Hence,

$$A^{(\alpha)}(x, z = z_p) = P(x) = A^{(R)}(x, z = z_p) - A_\infty, \tag{5.151}$$

where A_∞ has been subtracted from the Roumeliotis original solution in order to maintain $A(x = \pm x_0, z) = 0$.

With this condition, the coefficients a_n of Equation (5.149) will become

$$a_n = \frac{1}{x_0}\int_{-x_0}^{x_0}\left\{\frac{2A_\infty}{\pi}\tan^{-1}\left[\frac{z_0}{x_0}\frac{\sinh(\pi z_p/2z_0)}{\cos(\pi x/2x_0)}\right] - A_\infty\right\}\cos(k_n x)dx. \tag{5.152}$$

This integral has the analytical solution:

$$a_n = \frac{4A_\infty}{(2n+1)\pi}(-1)^{n+1}\,\Upsilon^{2n+1}, \tag{5.153}$$

where

$$\Upsilon = \sqrt{1+\tau^2} - \tau \qquad \text{and} \qquad \tau = \frac{z_0}{x_0}\sinh\left(\frac{\pi z_p}{2z_0}\right) \tag{5.154}$$

are constants that depend on the parameters x_0, z_0 and z_p. This result is derived in Appendix D.

To summarise, the flux function for the linear force-free case, using the Roumeliotis solution to give the boundary conditions, takes the form:

$$A^{(\alpha)}(x, z) = \frac{4A_\infty}{\pi}\sum_{n=0}^{\infty}\frac{(-1)^{n+1}}{(2n+1)}\,\Upsilon^{2n+1}\cos(k_n x)\exp\left\{-\sqrt{k_n^2-\alpha^2}(z - z_p)\right\}, \tag{5.155}$$

which produces a magnetic field of the form:

$$B_x^{(\alpha)}(x, z) = \frac{4A_\infty}{\pi}\sum_{n=0}^{\infty}\frac{(-1)^{n+1}}{(2n+1)}\,\Upsilon^{2n+1}\sqrt{k_n^2-\alpha^2}\cos(k_n x)\exp\left\{-\sqrt{k_n^2-\alpha^2}(z - z_p)\right\}, \tag{5.156}$$

$$B_y^{(\alpha)}(x, z) = \alpha A_\alpha(x, z), \tag{5.157}$$

$$B_z^{(\alpha)}(x, z) = \frac{2A_\infty}{x_0}\sum_{n=0}^{\infty}(-1)^n\,\Upsilon^{2n+1}\sin(k_n x)\exp\left\{-\sqrt{k_n^2-\alpha^2}(z - z_p)\right\}. \tag{5.158}$$

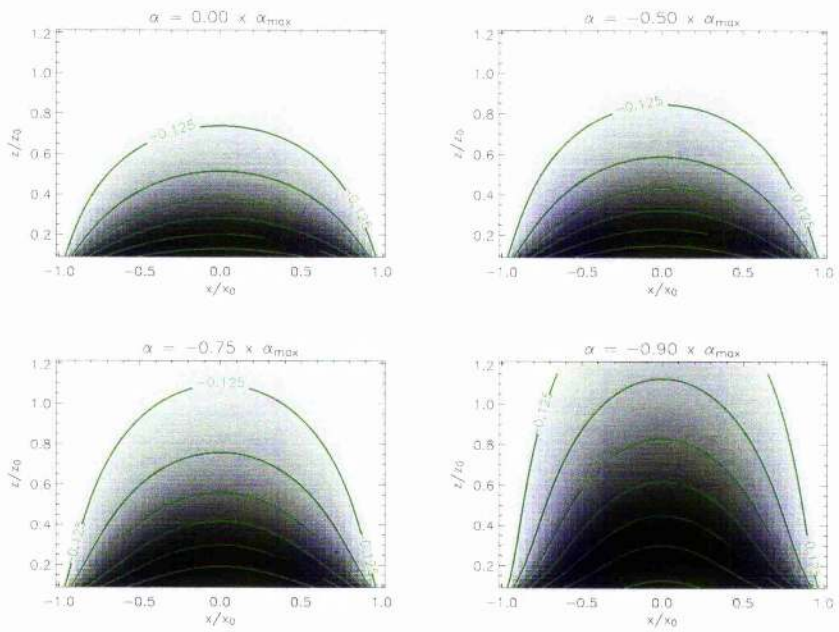

Figure 5.15: Flux function for the linear force-free field case, using $z_0 = 2x_0$ and $z_p = 0.1x_0$, for several values of α. The shading palette goes from black (where the flux function is $-A_\infty$) to white (where the flux function is zero). Several contours have also been plotted.

Since $z_p \ll x_0$ and $z_0 > x_0$, Υ can be expanded, using $\sinh(u) \approx u$ and $(1+u)^n \approx 1 + nu$, for u small, giving

$$\Upsilon \approx 1 + \frac{1}{2}\tau^2 - \tau \approx 1 - \frac{\pi z_p}{2x_0} + \frac{\pi^2 z_p^2}{8x_0^2}. \tag{5.159}$$

Υ will be always smaller than 1 and is almost independent of z_0. This will make the series above to converge quite rapidly.

The flux function and its associated magnetic field are shown in Figures 5.15 and 5.16, for different values of α. Figure 5.17 shows the isosurfaces of $A^{(\alpha)}$ and some field lines. Negative values for α have been chosen so $B_x^{(\alpha)}$ and $B_y^{(\alpha)}$ have opposite polarities.

As $|\alpha|$ increases, the arcades become higher due to an increase in $B_z^{(\alpha)}$. The shear increases as well, since $B_y^{(\alpha)}$ is proportional to α.

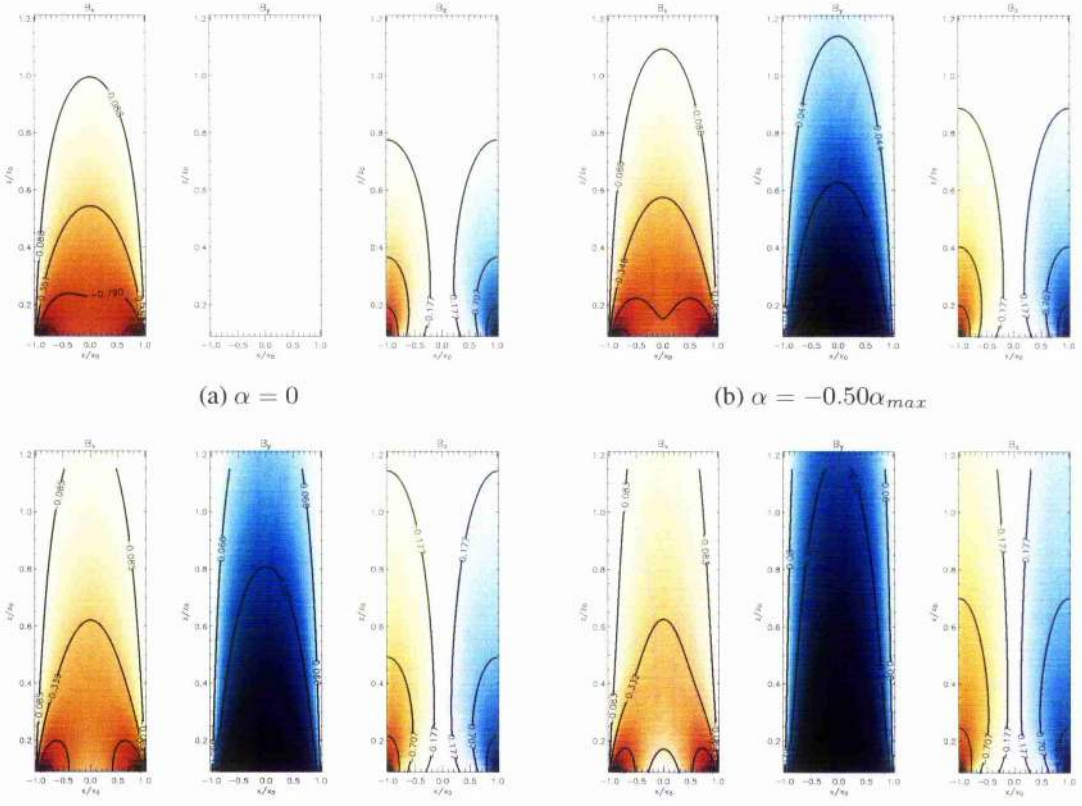

(a) $\alpha = 0$

(b) $\alpha = -0.50\alpha_{max}$

(c) $\alpha = -0.75\alpha_{max}$

(d) $\alpha = -0.90\alpha_{max}$

Figure 5.16: Magnetic field for the linear force-free field case, using $z_0 = 2x_0$ and $z_p = 0.1x_0$, for several values of α. Red shading means negative values while blue shading means positive values. Several contours have also been plotted.

5.2.4 Magnetic Energy

Since the system does not depend on y, the magnetic energy can be defined as:

$$W = \frac{L_y}{8\pi} \int_{-x_0}^{x_0} \int_{z_p}^{\infty} |\mathbf{B}|^2 dz dx, \tag{5.160}$$

where L_y is the scale length in the y direction.

Using Equations (5.127)-(5.129) for the Roumeliotis solution, or Equations (5.156)-(5.158) for the linear force-free solution, the magnetic energy can be calculated. In general both integrals need to be calculated numerically. An analytic expression can be obtained only for the potential case, when $z_0 = x_0$ The magnitude of the potential magnetic

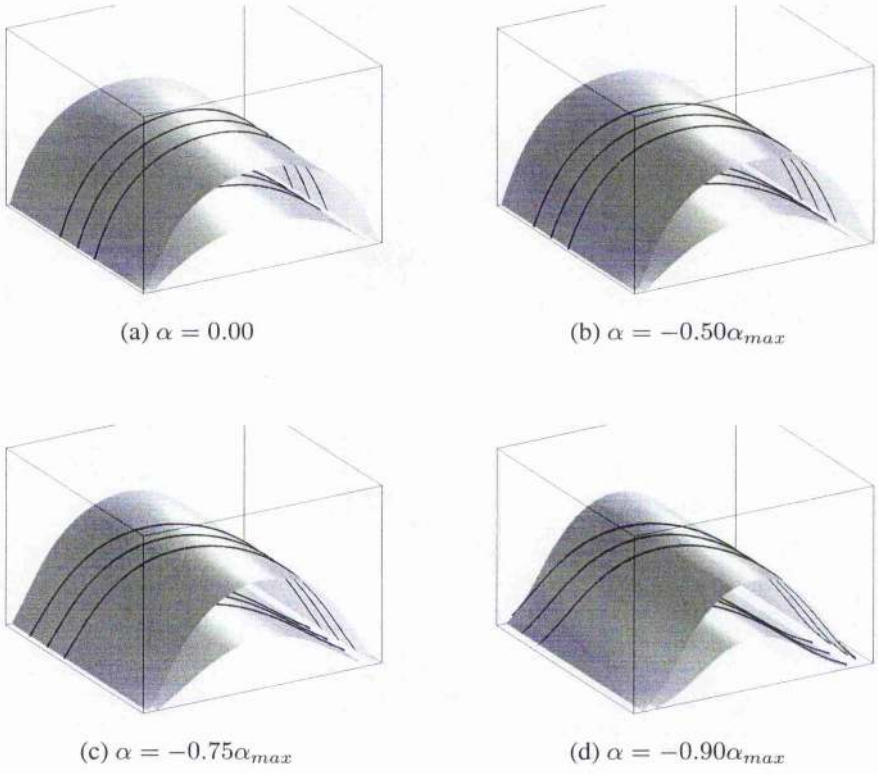

(a) $\alpha = 0.00$ (b) $\alpha = -0.50\alpha_{max}$

(c) $\alpha = -0.75\alpha_{max}$ (d) $\alpha = -0.90\alpha_{max}$

Figure 5.17: Isosurfaces of the flux function $A^{(\alpha)}$, for several values of α. Three field lines have also been plotted over each isosurface

field simplifies to

$$|\mathbf{B}|^2 = \left(\frac{A_\infty}{x_0}\right)^2 \frac{1}{\cos^2(\pi x/2x_0) + \sinh^2(\pi z/2x_0)}, \tag{5.161}$$

thus the energy becomes

$$W_0 = \frac{L_y A_\infty^2}{\pi^3} \int_{\pi z_p/2x_0}^{\infty} \int_0^{\pi/2} \frac{dv\, du}{\cos^2 v + \sinh^2 u}. \tag{5.162}$$

where $u = \pi z/2x_0$ and $v = \pi x/2x_0$. Firstly, the integral in v can be expressed as:

$$I_v = \int_0^{\pi/2} \frac{dv}{\cos^2 v + \sinh^2 u} = \frac{1}{\sinh^2 u + 1} \int_0^{\pi/2} \frac{dv}{1 - a^2 \sin^2 v}, \tag{5.163}$$

where $a = 1/\sqrt{1 + \sinh^2 u} = 1/\cosh u$. Using Gradshteyn and Ryzhik (1965a), the

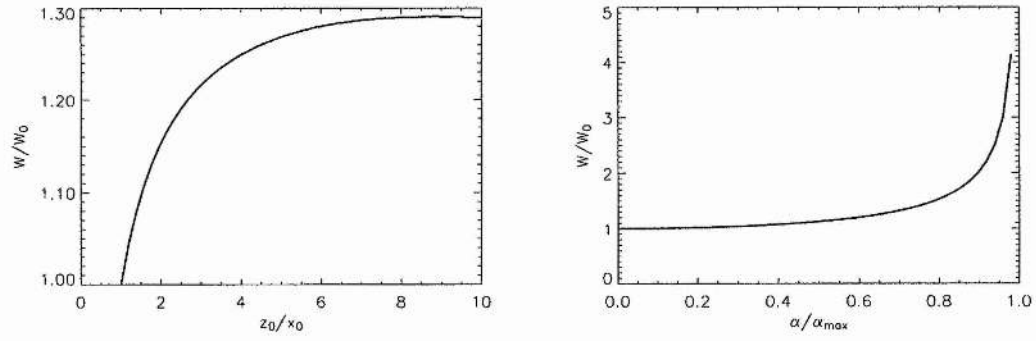

(a) (b)

Figure 5.18: Magnetic energy for (a) the Roumeliotis solution and (b) the linear force-free fields solution.

integral in v becomes

$$I_v = \frac{\pi}{2} \frac{1}{\sinh u \cos u}. \tag{5.164}$$

The potential magnetic energy takes the form

$$W_0 = \frac{L_y A_\infty^2}{2\pi^2} \int_{\pi z_p/2x_0}^{\infty} \frac{du}{\sinh u \cos u}, \tag{5.165}$$

using Gradshteyn and Ryzhik (1965b), the integral above can be simplified to

$$W_0 = \frac{A_\infty^2 L_y}{2\pi^2} \ln \left(\frac{\cosh(\pi z_p/2x_0)}{\sinh(\pi z_p/2x_0)} \right). \tag{5.166}$$

Due to the singularities of the Roumeliotis solution, the potential energy tends to infinity as the photospheric height decreases. The chosen height in the photosphere is $z_p = 0.1x_0$ which produces a potential energy of $W_0 = 0.0942 A_\infty^2 L_y$.

Figure 5.18 shows how the magnetic energy depends on the different parameters, the energy values have been normalised by the potential energy, W_0. For the Roumeliotis solution, the magnetic energy increases with z_0 due to a shear effect. The energy finally reaches a maximum value and saturates. For the linear force-free case, it is observed that the magnetic energy depends very weakly on z_0 and increases with α. It is also important to notice how the magnetic energy goes to infinity when α reaches its maximum value $\alpha_{max} = \pi/2x_0$.

5.2.5 Comparison Between Linear Force-Free Field and Non-Linear Force-Free Field

This section will compare the linear force-free field case, $\mathbf{B}^{(\alpha)}(x,z)$, formulated in Section 5.2.3 with the non-linear analytical solution, $\mathbf{B}^{(R)}(x,z)$, formulated in Section 5.2.2.

It is not hard to prove that, for the case $z_0 = x_0$ and $\alpha = 0$ both solutions are the same, namely the potential case.

Assuming that $z_0 \neq x_0$, there are many ways to estimate the value of α that produces a reasonable correlation between the linear force-free field solution and the Roumeliotis one.

For positions well above the photosphere, $z \gg z_p$, the series in Equations (5.155)-(5.158) converge very fast and the first term will be the dominant one. If only the first term in the summations is considered, the magnetic field takes the form:

$$B_x^{(\alpha)}(x,z) \approx -\frac{4A_\infty \Upsilon}{\pi}\left[\left(\frac{\pi}{2x_0}\right)^2 - \alpha^2\right]^{\frac{1}{2}} \cos\left(\frac{\pi x}{2x_0}\right) \exp\left\{-\left[\left(\frac{\pi}{2x_0}\right)^2 - \alpha^2\right]^{\frac{1}{2}}(z - z_p)\right\}, \tag{5.167}$$

$$B_y^{(\alpha)}(x,z) \approx -\frac{4\alpha A_\infty \Upsilon}{\pi}\cos\left(\frac{\pi x}{2x_0}\right) \exp\left\{-\left[\left(\frac{\pi}{2x_0}\right)^2 - \alpha^2\right]^{\frac{1}{2}}(z - z_p)\right\}, \tag{5.168}$$

$$B_z^{(\alpha)}(x,z) \approx \frac{2A_\infty}{x_0}\,\Upsilon \sin\left(\frac{\pi x}{2x_0}\right) \exp\left\{-\left[\left(\frac{\pi}{2x_0}\right)^2 - \alpha^2\right]^{\frac{1}{2}}(z - z_p)\right\}. \tag{5.169}$$

Therefore,

$$\frac{B_y^{(\alpha)}(x,z)}{B_x^{(\alpha)}(x,z)} \approx \frac{\alpha}{\sqrt{\left(\frac{\pi}{2x_0}\right)^2 - \alpha^2}}, \tag{5.170}$$

and α can be approximated as

$$\alpha \approx \frac{-B_y^{(\alpha)}}{\sqrt{(B_x^{(\alpha)})^2 + (B_y^{(\alpha)})^2}}. \tag{5.171}$$

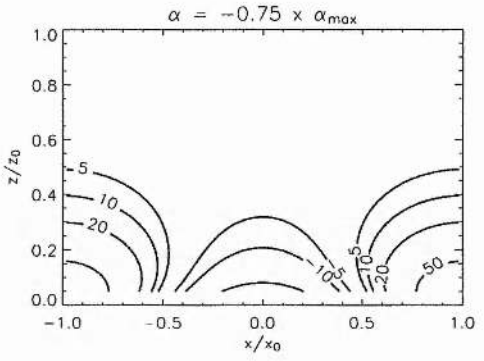

Figure 5.19: Percentage error in the approximated α.

Figure 5.19 shows the error of this assumption; for heights above $z_0/2$ the error is well below 5%.

Given a chosen position $\mathbf{r}^* = (x^*, z^*)$, the value of α that will produce the best fit between both magnetic field solutions will be

$$\alpha^* = \frac{-B_y^{(R)}(x^*, z^*)}{\sqrt{\left[B_x^{(R)}(x^*, z^*)\right]^2 + \left[B_y^{(R)}(x^*, z^*)\right]^2}}. \tag{5.172}$$

It will be interesting to compare $\mathbf{B}^{(\alpha=\alpha^*)}(x, z)$ with $\mathbf{B}^{(R)}(x, z)$ in the neighbourhood of $\mathbf{r}^*$.

Note that, when $x = 0$, the z-component of the magnetic field cancels. Imposing $x^* = 0$, both fields will be aligned at the particular point $\mathbf{r}^*$. It is important to realise that, in this case, it is not possible to make a renormalisation of the field as was done in Section 5.1.4. Changing the magnitude of $\mathbf{B}^{(\alpha)}$ would not satisfy the boundary condition in the photosphere.

Figure 5.20 shows how the two models differ along the line $x = 0$ for different values of z^*. The values of α^* obtained increase with z^*. Because of the different behaviour of both solutions, the linear approximation does not reproduce the same results as the Roumeliotis field for lower heights, but for higher z both have similar characteristics.

To see this explicitly, Figure 5.21 shows how the field lines compare for both models. For four different values of z^* the estimated α^* has been determined and four field lines with the starting points $(0, 0.5z_0)$, $(0, 1.0z_0)$, $(0, 1.5z_0)$, $(0, 2.5z_0)$ have been plotted. The

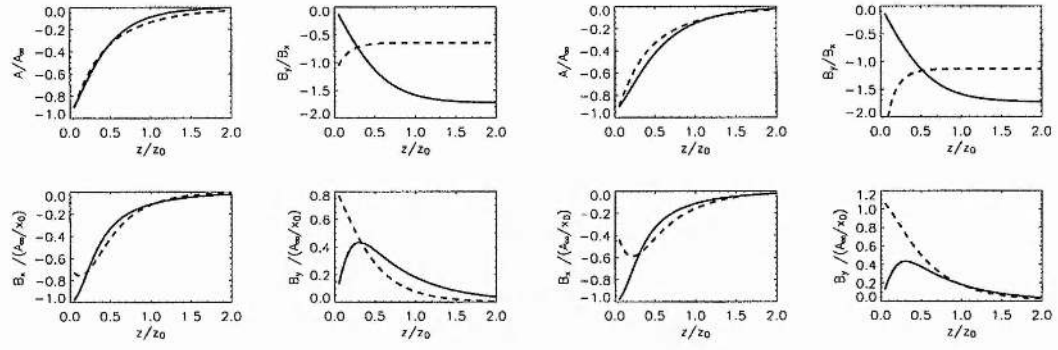

(a) $z^* = 0.5x_0,\ \alpha^* = -0.54\alpha_{max}$ (b) $z^* = 1.0x_0,\ \alpha^* = -0.75\alpha_{max}$

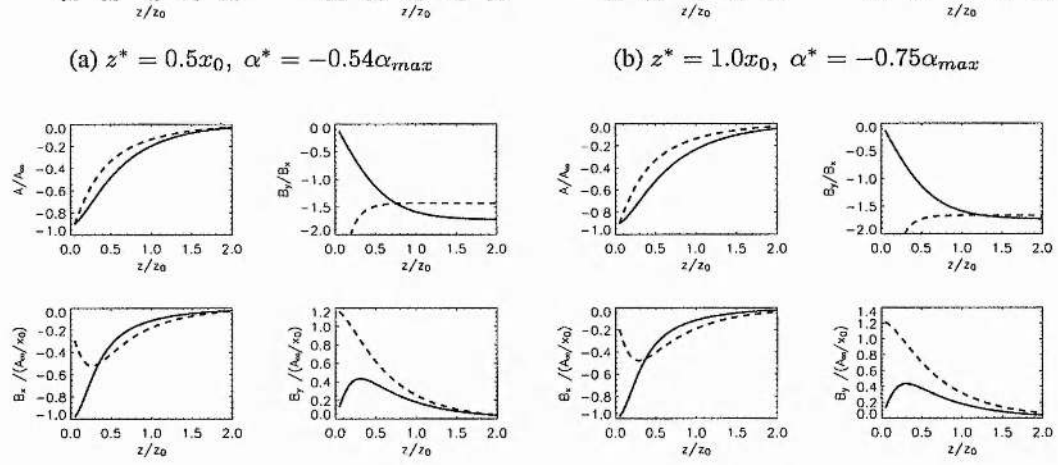

(c) $z^* = 1.5x_0,\ \alpha^* = -0.82\alpha_{max}$ (d) $z^* = 2.5x_0,\ \alpha^* = -0.86\alpha_{max}$

Figure 5.20: Comparison between the linear force-free field and the Roumeliotis solution, for different values of z^*, fixing $x = 0$. The solid lines correspond to the Roumeliotis model, while the dashed lines correspond to our linear force-free field solution.

biggest difference between both models is their height dependence. For the Roumeliotis solution, the angle the field lines form with respect to the y-axes depend highly on z, while in the linear force-free case, this angle remains almost constant. Therefore, if an observed structure follows the Roumeliotis solution, it can be reproduced quite accurately with the linear force-free assumption as long as the structure contains field lines of similar heights.

Another factor to take into account is the total magnetic energy for both models. For the Roumeliotis solution, using $z_0 = 2x_0$ and $z_p = 0.1x_0$, the magnetic energy becomes $W_R = 1.154W_0$. The linear force-free magnetic energy will depend on the chosen value of the parameter α. Table 5.4 shows the different values of the magnetic energy. As the height increases, a larger value of α is needed to reproduce similar field lines, but then the magnetic energy becomes very large in comparison with the Roumeliotis field.

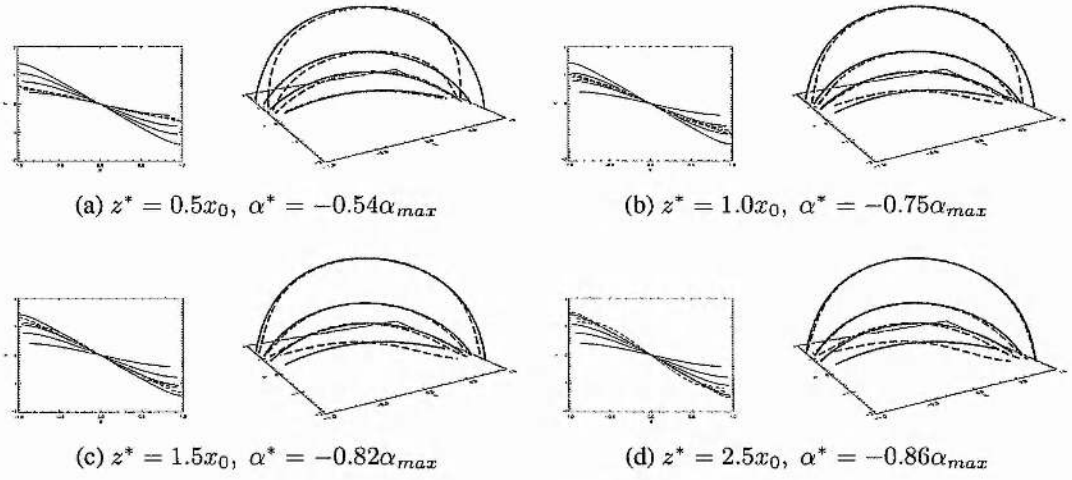

(a) $z^* = 0.5x_0,\ \alpha^* = -0.54\alpha_{max}$ (b) $z^* = 1.0x_0,\ \alpha^* = -0.75\alpha_{max}$

(c) $z^* = 1.5x_0,\ \alpha^* = -0.82\alpha_{max}$ (d) $z^* = 2.5x_0,\ \alpha^* = -0.86\alpha_{max}$

Figure 5.21: Field line comparison between the linear force-free field and the Roumeliotis solution, for different values of z^*. The solid blue field lines correspond to the Roumeliotis model, while the dashed red field lines correspond to the linear force-free field solution obtained in Section 5.2.3.

z^*/x_0	α^*/α_{max}	W_α/W_0	$W_\alpha - W_R$ (%)
0.5	-0.54	1.155	0.06
1.0	-0.75	1.411	18.2
1.5	-0.82	1.595	27.7
2.5	-0.86	1.750	34.0

Table 5.4: Comparison between Roumeliotis and linear magnetic energy.

5.2.6 Conclusion

This section has studied the linear force-free solution for translational symmetry, where the photosphere is just a plane and the field has an arcade shape.

Imposing an isolated system with vertical field lines at $x = \pm x_0$, an analytical expression of the linear force-free magnetic field has been obtained. One of the solutions obtained by Roumeliotis (1993) has been used to provide the boundary conditions. The case $\alpha = 0$ corresponds to the unsheared potential field with an almost circular shaped arcade. As α increases, the twist increases and the isosurfaces expand in the z-direction and compress in the x-direction.

Also, the values of α have a limited range given by $|\alpha| \leq \pi/2x_0$, for larger values the

flux function will have an oscillating term in the z direction and will not tend to zero as z tends to infinity.

This linear solution has been compared with a similar geometry solution, deduced by Roumeliotis (1993). Constraining the comparison to a small range of height, both models produce very similar structures. The energies on the other hand only are similar when the structures are not very high in the corona.

Chapter 6

Summary and Further Work

So, good night unto you all.
Give me your hands, if we be friends,
And Robin shall restore amends.
- **William Shakespeare**, A Midsummer Night Dream, Act V (1590).

6.1 Summary

The solar corona is one of the most studied areas in solar physics. Its activity, such as flares, prominence eruptions and CMEs, is far from understood. Since the solar corona is a low-β plasma, its structure and dynamics are driven by the magnetic field.

The aim of this thesis is the study of the magnetic field in the solar corona. Unfortunately, high quality direct measurements of the coronal magnetic field are not available.

The thesis can be divided into two separate parts. In the first part, from Chapter 2 to Chapter 4, a quantitative way to compare theory and observations is introduced and applied.

The second part of the thesis, Chapter 5, focused on the linear force-free field. Analytical expressions are obtained for two different geometric configurations and they are compared with other more general non constant α solutions.

6.1.1 Comparing Theory and Observations

The magnetic field in the solar corona cannot be measured easily. As an alternative, the magnetic field in the corona can be extrapolated from the known magnetic field in the photosphere. There are many models of magnetic extrapolations, some of them have been summarised in Chapter 2. Although theoretical models are very useful in determining general properties of the corona and its evolutionary states, it is still necessary to see if they can reproduce the type of structures observed.

In most studies, comparison between theoretical magnetic fields and observation consists on plotting a group of field lines and comparing with the shape of the structures observed. This methodology has some clear weaknesses. That is why it is necessary to introduce some qualitative study to measure the deviation between theory and observations.

A quantitative method to fit magnetic field lines to observed coronal loops is introduced in Chapter 3. The method needs only two things: Firstly, a magnetic field model is necessary to calculate the field lines. It will probably include a magnetogram for the photospheric boundary conditions. Also needed is an image of the corona, where the structure is observed. The more isolated the structure is, the better the method will work.

The procedure will calculate a quantity C, for each field line, which can be understood as the average of the distance between the field line and the loop. The smaller the value of C is, the more closely the field line follows the observed loop.

If the magnetic field depends on one or more parameters, the value of the parameter(s) that provides the best fit between theory and observations will be the one that minimise C.

In Chapter 4 the method described above was used to study the magnetic field in an active region. AR 8906 was first studied by Glover et al. (2001) where its evolution was followed during three solar rotations. During its third rotation, the active region suffered two CMEs which changed its morphology. In order to determine how much the magnetic field changed though the CMEs, the active region is studied prior and after its first eruption.

Prior to the first CME, the AR had three separate structures, each of them was fitted individually using a Green's function linear force-free field model. The value of α ob-

tained for each area was very similar, which indicates that the AR was in a near linear force-free magnetic configuration.

After the first CME the morphology of the region changed considerably. The area which presented a higher value of α before the eruption was not visible anymore after the CME and the remaining structures seemed to have join in a longer loop. This structure was again fitted to a linear force-free field to find a similar value for α. The error of this last estimate was considerable, making it not possible to reach a firm conclusion about the evolution of α. This also shows that the linear force-free field might not be a valid approximation for the magnetic field in the AR at this stage in its evolution.

The field line fitting method has also been used when more than one parameter is necessary to specify the magnetic field. Petrie and Lothian (2003) suggested a more general linear force-free solution, where the magnetic field depends on two parameters, α and b. This model was used with the same AR as the one studied before. Although adding this new parameter does not improve considerably the results, this example showed how the field line fitting method works for more than one parameter.

Another totally different problem was also studied using the field line fitting method. A group of loops were observed near the limb with TRACE and SOHO/CDS. In order to obtain the strength of the magnetic field inside each loop, the field line that better reproduces the shape of the observed loop must be founded. In this case, three free parameters were necessary, which were the coordinates of the starting position of the field lines. Since the method needed each loop to be as isolated as possible, the original image was altered to remove the background around each loop. The method worked very well for the majority of the loops.

The variable that quantifies the discrepancy between the theoretical field lines and the observed loops, C, is the standard deviation of the distance between them for each point of the field line. Therefore, when very small structures are studied, very short field lines will be selected and the statistical value of C becomes less meaningful. This is the main reason why the smallest loops studied from the structure above did not return a good fit using the method. Although this is a weakness in the method that should be considered, it is not very dramatic, since, at these scales, the magnetograms are not that accurate and the magnetic extrapolation is also not very reliable.

6.1.2 Linear Force-free Field

Linear force-free fields have been used in many studies of the magnetic field of the corona. Although some would say that it is too simple to produce realistic results, constant α force-free fields produce analytical expressions that are relatively easy to compute.

Chapter 5 studied the linear force-free field for two different geometrical systems. An analytical expression of the field was obtained and compared with more general solutions.

For the first system, the photosphere consisted on two parallel planes connected by a vertical flux tube. The Grad-Shafranov(-Schlüter) equation of rotational symmetry was solved for the linear force-free case. The boundary conditions were: the flux function vanishes at the centre of the tube, the tube does not expand or contract and the total flux through the end of the tube remained fixed.

An analytical expression of the flux function and the magnetic field was found in terms of the Bessel functions. Most of the tube remains in a near radial state. It is only near the footpoints were a dependence on the coordinate along the loop, z is apparent. Also, the possible values of the parameter α were constrained to be within a limited range.

The magnetic energy and the magnetic helicity were also obtained for this case. The magnetic energy depends very weakly on the length of the tube, this dependence is only due to the footpoint areas where the magnetic field depends strongly on z. For small values of α, the helicity is almost a straight line, independent of the loops length. As α increases, the helicity increases and a dependence on the length of the tube becomes more noticeable.

The linear solution was then compared with two cylindrically symmetric twist profiles. It was shown that the linear force-free field can reproduce a similar structure for the inner part of the tube, but the non-linear field differs strongly from the linear one for the outer part of the tube. Similar conclusions can be drawn from the magnetic energy.

For the second system, the photosphere is an infinite plane and the coronal magnetic field is anchored to it. The Grad-Shafranov(-Schlüter) equation for translational geometry was solved for the linear force-free case. The assumptions taken where: the system was isolated, the magnetic energy was finite and all the field lines started and ended at the photospheric level.

Using the solution obtained by Roumeliotis (1993) as the flux function in the photo-

sphere, analytical expressions for the flux function and the magnetic field were obtained.

For $\alpha = 0$, the unsheared potential field is obtained. As α increases the shear in the arcade increases and the isosurfaces expand in the z-direction and contract in the x-direction. The magnetic energy increase with the parameter α tending to infinity when α reaches its maximum value.

The linear force-free field was compared with the non linear solution obtained by Roumeliotis (1993). Constraining the comparison to a small range of height, both models produce structures with very similar shapes. The energies are similar only when the structures are not very high in the corona.

6.2 Future Work

6.2.1 Magnetic Field Line Fitting

The method described in Chapter 3 is a first approach towards a quantitative way to compare theory and observations. Although the method works for one or more different parameters and under very different magnetic models, there are a few weaknesses that could be improved.

A first improvement would be to reduce the long computational time, as mentioned in Section 3.4.1. The routines could become substantially faster by transferring the computation of the field lines to a more appropriate platform (e.g. Fortran code implemented in a parallel computer). The way the magnetogram data is evaluated can also be optimised by ignoring areas where the magnetic field is bellow a certain threshold.

The footpoint areas are currently selected manually, this step can be automated using advanced feature recognition techniques. It is also necessary to observe a complete loop in the intensity image so the footpoints can be selected. A more general way to select field lines could be introduced to make the method less restrictive.

The method is also very sensitive to background emission or interconnected loops. For high resolution images, such as TRACE, groups of loops are observed instead of an isolated one, making necessary to alter the original image in order to study each individual loop separately. Some improvements in this line should also be desirable.

The field line fitting method has been used to study how the linear force-free parameter α varies along an AR and how it evolves with time. More studies of this kind can throw some light into the coronal magnetic field evolution and how it depends on the photospheric motions.

The method can also be used to calculate α in nearby regions in order to obtain a map of $\alpha(\mathbf{r})$. An initial value of α for the lower boundary of the computational box is necessary for some non-linear force-free methods (as discussed in Section 2.2.3). It could be possible to use this field line fitting method to derivate the map of α instead of the highly inaccurate vector magnetograms.

Observations of an AR with different wavelength filters will outline plasma at different temperatures. It would be interesting to see whether different observations of an AR are indeed represented by a common α in a linear force-free model, or whether the value of α varies significantly. This would provide a measure of the quality of the linear force-free model in a localised region of the corona, and would have implications on the validity of using this model to study changes in α over a period of time.

The fitting method assumes that magnetic field lines highlight the general profile of the structures observed in the corona, and therefore comparing both should produce an estimation about how close the theoretical magnetic field is from the real one. There is another way to approach this problem which would not involve directly fitting field lines. Given a theoretical magnetic field, the temperature and the density could be determined using the thermal energy equation. A synthetic image could then been produced from the response function of a given instrument. This synthetic image can then be directly compared with a real image of the area of interest. As done in the field line fitting, some quantity can be calculated to measure the differences between them. Changing the magnetic field would change the synthetic image and the difference quantity. The magnetic field that minimise the difference between the observed image and the produced synthetic one could be assumed to be the more accurate one for the studied AR.

6.2.2 Comparing Linear with Non Linear Force-Free Field

For both geometries the analytical linear force-free field was compared with more general solutions. How to compare two magnetic field systems is not straight forward.

For the axisymmetric case, two twist profiles where chosen and the energy and mag-

netic field were compared directly. A set of field lines could have been compared in a similar way as it was done for the arcade geometry case, but visualisation was harder in this case. To get a better idea, more twist profiles could be used, or maybe a more general solution. It is a similar case with the arcade geometry.

In order to compare linear force-free field with a more general one, a choice in α has to be taken. For both studies, the two magnetic fields where coaligned in a particular point as it was shown how they compared in its neighbourhood. This points out how local the linear force-free field is. Making this fit for the entire area of study, map of $\alpha(\mathbf{r})$ can also be obtained.

For both of the studied cases, the system presents a symmetry. The next step would be to consider a non-linear force-free field in three dimensions (thus, without any symmetry) and compare it with the linear one. This non-linear force-free field would probably be obtained by a numerical simulation. The numerical value of $\alpha(\mathbf{r})$ could be obtained to see how local structures could be fitted into linear force-free field.

6.2.3 Future Missions

Over the last ten years the success of the Yohkoh, SOHO and more recently TRACE and RHESSI missions have transformed dramatically our knowledge of the Sun. Over the next ten years new spacecraft will build on these successes, with the Japan-UK Solar-B and NASA Solar Dynamics Observatory (SDO) missions providing much higher-resolution information of the solar corona, the NASA STEREO mission allowing stereoscopic study of structures in the corona and solar wind and the ESA SOLar Orbiter (SOLO) will provide unprecedentedly high resolution data over long periods as it almost co-rotates with the Sun.

Table 6.1 displays a summary of the instruments that will be included in the future missions. These missions will provide high resolution magnetograms which can be used to produced extrapolated coronal magnetic fields using the methods described in Chapter 2.

Also, high resolution images will be produced in different wavelengths (such as X-Rays using Solar-B/XRT or EUV using Solar-B/EUT and Solar Orbiter/EUI).

The magnetic field line fitting method, described in Chapter 3 can be used with these

Mission	Instrumentation	Brief Description
Solar-B	SOT	50cm optical telescope (150 km resolution)
	FPP	Narrow-band filtergrams/magnetograms/Dopplergrams/Stokes images
	XRT	Full-disk X-ray imager (2 Åto 60 Å), YOHKOH-SXT follow-on
	EIS	Multi-layer EUV telescope/spectroscope (170 - 210 Åand 250-290 Å)
Stereo	SECCHI	2 white-light coronagraphs/EUV imager/heliosperic imager
	SWAVES	Interplanetary radio burst tracker
	IMPACT	In-situ solar energetic particle detector
	PLASTIC	Plasma and suprathermal ion detector
SDO	HMI	Helioseismic and magnetic imager (MDI follow-on)
	SHARPP	White-light coronographic imager
	EVE	Full-disk irradiance spectrometer (10-1200 Å)
SOLO	VIM	White-light imager & magnetograph
	EUS	EUV spectrometer
	EUI	EUV imager
	UVC	UV & white-light coronagraph
	SWA/RPW	Solar wind plasma analyser / radio & plasma waves analyser
	CRS/RAD	Coronal radio sounding/radiometer
	MAG	Magnetometer
	EPD/NED	energetic particle detector / neutron detector
	DUD/NPD	dust detector / neutral particle detector

Table 6.1: Brief Summary of future solar missions.

new observations to give us an idea how the different magnetic extrapolations can reproduce the high resolution structures observed.

Appendix A

Linear Force-free field using Green's Functions

In Cartesian geometry, the photosphere is represented as the plane $z = 0$, while the corona is the upper half-space, $z > 0$.

Assuming that the magnetic field is a constant α force-free field, the equations to be solved in the corona are

$$\nabla \times \mathbf{B} = \alpha \mathbf{B}, \tag{A.1}$$

$$\nabla \cdot \mathbf{B} = 0. \tag{A.2}$$

The boundary conditions will be:

$$B_z(x, y, 0) = B_0(x, y), \tag{A.3}$$

$$\lim_{z \to \infty} \mathbf{B}(x, y, z) = 0, \tag{A.4}$$

where $B_0(x, y)$, the normal component of the magnetic field in the photosphere, is obtain using magnetograms.

The magnetic field can be written in the form:

$$\mathbf{B} = \nabla \times \nabla \times (P\hat{z}) + \nabla \times (T\hat{z}), \tag{A.5}$$

which can be substituted into Equation (A.1) to give:

$$\nabla \times \nabla \times [(T - \alpha P)\hat{z}] - \nabla \times [(\alpha T + \Delta P)\hat{z}] = 0; \tag{A.6}$$

which is satisfied when:

$$T - \alpha P = 0 \tag{A.7}$$

$$\alpha T + \Delta P = 0 \tag{A.8}$$

thus

$$\Delta P + \alpha^2 P = 0. \tag{A.9}$$

Equation (A.9) is the *Helmholtz Equation*. Cylindrical polar coordinates and separation of variables can be used to obtain the solution:

$$\begin{aligned} P(r,\theta,z) = \sum_{m=-\infty}^{\infty} e^{im\theta} \Bigg\{ & \int_{\alpha}^{\infty} A_m(k) \exp\left[-\left(k^2-\alpha^2\right)^{1/2} z\right] J_m(kr)dk \\ & + \int_0^{\alpha} B_m(k) \cos\left[\left(\alpha^2-k^2\right)^{1/2} z\right] J_m(kr)dk \\ & + \int_0^{\alpha} C_m(k) \sin\left[\left(\alpha^2-k^2\right)^{1/2} z\right] J_m(kr)dk \Bigg\}, \end{aligned} \tag{A.10}$$

where A_m, B_m and C_m are to be determined and J_m is the Bessel function of order m. Substituting P in Equation (A.5), the magnetic field takes the form:

$$\begin{aligned} B_z(r,\theta,z) = -k^2 P(r,\theta,z) = \\ \sum_{m=-\infty}^{\infty} e^{im\theta} \Bigg\{ & \int_{\alpha}^{\infty} A_m(k)k^2 \exp\left[-\left(k^2-\alpha^2\right)^{1/2} z\right] J_m(kr)dk \\ & + \int_0^{\alpha} B_m(k)k^2 \cos\left[\left(\alpha^2-k^2\right)^{1/2} z\right] J_m(kr)dk \\ & + \int_0^{\alpha} C_m(k)k^2 \sin\left[\left(\alpha^2-k^2\right)^{1/2} z\right] J_m(kr)dk \Bigg\}. \end{aligned} \tag{A.11}$$

Equation (A.11) can be evaluated on the $z = 0$ plane to produce:

$$B_z(r,\theta,0) = \sum_{m=-\infty}^{\infty} e^{im\theta} \left[\int_{\alpha}^{\infty} A_m(k)k^2 J_m(kr)dk + \int_0^{\alpha} B_m(k)k^2 J_m(kr)dk \right]. \tag{A.12}$$

Note that, as C_m terms disappear due to the evaluation of $\sin\left[(\alpha^2 - k^2)^{1/2} z\right]$ when $z = 0$, the boundary condition of Equation (A.3) cannot be used to evaluate $C_m(k)$ and some extra information is needed. The most common approach to this problem is to ignore the C_m contribution, which is equivalent to imposing that $\partial B_z/\partial z = 0$ where $B_z \neq 0$ and $z = 0$. The contribution of the term involving C_m will be obtained later on.

In order to find the values of A_m and B_m in terms of $B_z(r, \theta, 0)$, it is necessary to invert Equation (A.12) using the completeness relation for Bessel functions and exponential terms:

$$\int_0^\infty x J_m(\lambda x) J_m(\lambda' x) dx = \frac{\delta(\lambda' - \lambda)}{\lambda'} \quad \text{and} \tag{A.13}$$

$$\int_0^{2\pi} e^{im\theta} e^{-in\theta} d\theta = 2\pi\delta_{mn}. \tag{A.14}$$

Multiplying Equation (A.12) by $e^{-in\theta} J_n(k'r)$ and integrating over r and θ:

$$\int_0^\infty \int_0^{2\pi} e^{-in\theta} J_n(k'r) B_z(r, \theta, 0) r d\theta dr = 2\pi k' \left[A_n(k') H(k' - \alpha) + B_n(k') H(k' - \alpha)\right], \tag{A.15}$$

where $H(x)$ is the *step function*[1]. The above equation separates to:

$$A_m(k) = \frac{1}{2\pi k} \int_0^\infty \int_0^{2\pi} e^{-im\theta} J_m(kr) B_z(r, \theta, 0) r d\theta dr \qquad \text{for } k > \alpha, \tag{A.17}$$

$$B_m(k) = \frac{1}{2\pi k} \int_0^\infty \int_0^{2\pi} e^{-im\theta} J_m(kr) B_z(r, \theta, 0) r d\theta dr \qquad \text{for } k < \alpha. \tag{A.18}$$

Using the identity:

$$\sum_{m=-\infty}^{\infty} e^{im(\theta - \theta')} J_m(kr) J_m(kr') = J_0(kR), \tag{A.19}$$

where $R^2 = (x - x')^2 + (y - y')^2$ and ignoring the term containing $C_m(k)$, Equation

[1]The step function is defined as:

$$H(x) = \begin{cases} 0 & \text{if } x < 0, \\ \frac{1}{2} & \text{if } x = 0, \\ 1 & \text{if } x > 0. \end{cases} \tag{A.16}$$

(A.10) becomes:

$$P(r,\theta,z) = \frac{1}{2\pi}\int_0^{\infty}\int_0^{2\pi} G_1(r,\theta,z,r',\theta')B_z(r',\theta',0)r'd\theta'dr', \tag{A.20}$$

where

$$G_1(r,\theta,z,r',\theta') = \int_{\alpha}^{\infty}\frac{1}{k}J_0(kR)\exp\left[-\left(k^2-\alpha^2\right)^{1/2}z\right]dk + \int_0^{\alpha}\frac{1}{k}J_0(kR)\cos\left[\left(\alpha^2-k^2\right)^{1/2}z\right]dk. \tag{A.21}$$

Using Equation (A.5), the magnetic field components can be expressed in terms of the derivatives of P, which are equivalent to the derivatives of G_1. Calculating these derivatives, the magnetic field can be written in the form:

$$\mathbf{B}(x,y,z) = \frac{1}{2\pi}\int_{-\infty}^{\infty}\int_{-\infty}^{\infty}\mathbf{G}(x,y,z,x',y')B_z(x',y',0)dx'dy', \tag{A.22}$$

where

$$G_x(x,y,z,x',y') = \frac{\partial^2 G_1}{\partial z\partial x} + \alpha\frac{\partial G_1}{\partial y} = \frac{x-x'}{R}\frac{\partial\Gamma}{\partial z} + \alpha\Gamma\frac{y-y'}{R}, \tag{A.23}$$

$$G_y(x,y,z,x',y') = \frac{\partial^2 G_1}{\partial z\partial y} - \alpha\frac{\partial G_1}{\partial x} = \frac{y-y'}{R}\frac{\partial\Gamma}{\partial z} - \alpha\Gamma\frac{x-x'}{R}, \tag{A.24}$$

$$G_z(x,y,z,x',y') = -\frac{\partial^2 G_1}{\partial x^2} - \frac{\partial^2 G_1}{\partial y^2} = -\frac{\Gamma}{R} - \frac{\partial\Gamma}{\partial R}. \tag{A.25}$$

And Γ takes the form

$$\Gamma = -\int_{\alpha}^{\infty} J_1(kR)\exp\left[-\left(k^2-\alpha^2\right)^{1/2}z\right]dk - \int_0^{\alpha} J_1(kR)\cos\left[\left(\alpha^2-k^2\right)^{1/2}z\right]dk. \tag{A.26}$$

Watson (1995b), page 416 equation 4 describes

$$\int_0^{\infty} J_0(bt)\exp\{-a(t^2-y^2)^{1/2}\}\frac{t\,dt}{(t^2-y^2)^{1/2}} = \frac{\exp\{\mp iy(a^2-b^2)^{1/2}\}}{(a^2-b^2)^{1/2}}. \tag{A.27}$$

Making the substitution: $t = k, a = z, b = R$ and $y = \alpha$ and dividing into its real and

imaginary parts, the next identities are obtained:

$$\frac{\cos(\alpha\rho)}{\rho} = \int_{\alpha}^{\infty} \frac{k}{(k^2-\alpha^2)^{1/2}} \exp\left[-\left(k^2-\alpha^2\right)^{1/2} z\right] J_0(kR)dk - \int_0^{\alpha} \frac{k}{(\alpha^2-k^2)^{1/2}} \sin\left[\left(\alpha^2-k^2\right)^{1/2} z\right] J_0(kR)dk, \text{ and} \quad \text{(A.28)}$$

$$\frac{\sin(\alpha\rho)}{\rho} = \int_0^{\alpha} \frac{k}{(\alpha^2-k^2)^{1/2}} \cos\left[\left(\alpha^2-k^2\right)^{1/2} z\right] J_0(kR)dk, \quad \text{(A.29)}$$

where $\rho^2 = R^2 + z^2$.

To obtain the value of Γ, it is necessary to integrate by parts using the identity:

$$\frac{1}{R}\frac{dJ_0}{dk}(kR) = -J_1(kR). \quad \text{(A.30)}$$

Finally, using Equation (A.28), Γ takes the form :

$$\Gamma = \frac{z\cos(\alpha\rho)}{R\rho} - \frac{\cos(\alpha z)}{R}, \quad \text{(A.31)}$$

where $R^2 = (x-x')^2 + (y-y')^2$.

Using a similar approach, the C_m term can be calculated. It is necessary to assume that there is a function in the source coordinates such that

$$H(x',y') = \sum_{m=-\infty}^{\infty} e^{im\theta} \int_0^{\alpha} C_m(k)k^2 J_m(k)dk. \quad \text{(A.32)}$$

Then the coefficients C_m can be expressed as

$$C_m(k) = \frac{1}{2\pi k} \int_0^{\infty} \int_0^{2\pi} H(r',\theta')e^{-im\theta'} J_m(kr')r'dr'd\theta. \quad \text{(A.33)}$$

Therefore, the contribution of the term with the C_m coefficients in $P(x,y,z)$ can be expressed as

$$\tilde{P}(x,y,z) = \frac{1}{2\pi} \int_0^{\infty} \int_0^{\infty} G_2(x,y,z,x',y')H(x',y')dx'dy', \quad \text{(A.34)}$$

where

$$G_2 = \int_0^{\alpha} \frac{1}{k} J_0(kR) \sin\left[(\alpha^2-k^2)^{1/2} z\right] dk. \quad \text{(A.35)}$$

The contribution of the C_m term in the magnetic field is

$$\tilde{\mathbf{B}}(x,y,z) = \frac{1}{2\pi}\int_{-\infty}^{\infty}\int_{-\infty}^{\infty}\tilde{\mathbf{G}}(x,y,z,x',y')H(x',y')dx'dy', \tag{A.36}$$

where the *complementary Green's function*, $\tilde{\mathbf{G}}(x,y,z,x',y')$, is

$$\tilde{G}_x(x,y,z,x',y') = \frac{\partial^2 G_2}{\partial z \partial x} + \alpha\frac{\partial G_2}{\partial y} = \frac{x-x'}{R}\frac{\partial\tilde{\Gamma}}{\partial z} + \alpha\tilde{\Gamma}\frac{y-y'}{R}, \tag{A.37}$$

$$\tilde{G}_y(x,y,z,x',y') = \frac{\partial^2 G_2}{\partial z \partial y} - \alpha\frac{\partial G_2}{\partial x} = \frac{y-y'}{R}\frac{\partial\tilde{\Gamma}}{\partial z} - \alpha\tilde{\Gamma}\frac{x-x'}{R}, \tag{A.38}$$

$$\tilde{G}_z(x,y,z,x',y') = -\frac{\partial^2 G_2}{\partial x^2} - \frac{\partial^2 G_2}{\partial y^2} = -\frac{\tilde{\Gamma}}{R} - \frac{\partial\tilde{\Gamma}}{\partial R}, \tag{A.39}$$

where

$$\tilde{\Gamma} = -\int_0^{\alpha} J_1(kR)\sin\left[(\alpha^2-k^2)^{1/2}z\right]dk. \tag{A.40}$$

$\tilde{\Gamma}$ is calculated the same way as Γ but, using Equation (A.29) instead. It is straight forward to prove that

$$\tilde{\Gamma} = \frac{z\sin(\alpha\rho)}{R\rho} - \frac{\sin(\alpha z)}{R}. \tag{A.41}$$

To summarise, the general result for force-free magnetic field in Cartesian coordinates, using Green's functions, takes the form:

$$\begin{aligned}\mathbf{B}(x,y,z) = \frac{1}{2\pi}\int_{-\infty}^{\infty}\int_{-\infty}^{\infty}&\mathbf{G}(x-x',y-y',z)B_z(x',y',0)dx'dy' \\ &+ \frac{1}{2\pi}\int_{-\infty}^{\infty}\int_{-\infty}^{\infty}\tilde{\mathbf{G}}(x-x',y-y',z)H(x',y')dx'dy',\end{aligned} \tag{A.42}$$

where $H(x,y)$ is an arbitrary function of the source coordinates, $\mathbf{G}$ is the Green's function and $\tilde{\mathbf{G}}$ is the "complementary" Green's function. The Green's function components G_x, G_y and G_z take the form:

$$\begin{aligned}G_x(x,y,z,x',y') &= \frac{x-x'}{R}\frac{\partial\Gamma}{\partial z} + \alpha\Gamma\frac{y-y'}{R}, \\ G_y(x,y,z,x',y') &= \frac{y-y'}{R}\frac{\partial\Gamma}{\partial z} - \alpha\Gamma\frac{x-x'}{R}, \\ G_z(x,y,z,x',y') &= -\frac{\Gamma}{R} - \frac{\partial\Gamma}{\partial R},\end{aligned} \tag{A.43}$$

where

$$\Gamma = \frac{z\cos(\alpha\rho)}{R\rho} - \frac{\cos(\alpha z)}{R}, \tag{A.44}$$

with $R^2 = (x-x')^2 + (y-y')^2$ and $\rho^2 = R^2 + z^2$. Meanwhile $\tilde{\mathbf{G}}$ has the same structure as $\mathbf{G}$ in Equation A.43 with Γ replaced by a function $\tilde{\Gamma}$ whose expression is

$$\tilde{\Gamma} = \frac{z\sin(\alpha\rho)}{R\rho} - \frac{\sin(\alpha z)}{R}. \tag{A.45}$$

Appendix B

Numerical Computation of Field Lines

The equations of a field line are simply

$$\frac{d\mathbf{r}(s)}{ds} = \frac{\mathbf{B}\left(\mathbf{r}(s)\right)}{|\mathbf{B}\left(\mathbf{r}(s)\right)|} = \mathbf{F}\left(s, \mathbf{r}\right) \tag{B.1}$$

where $\mathbf{r}(s)$ is the position vector of the field line as a function of the parameter s, which is the length of the line from the initial point. This is a *initial value problem* where the starting point of the field line is given, $\mathbf{r}(s = 0) = \mathbf{r}_0$. If the differentiation is rewritten as finite steps, Δs, an algebraic formula can be obtained for the change in the function $\mathbf{r}$ when the independent variable s is stepped by one stepsize. This way, starting from the initial condition, the field line can be constructed until a final condition is reached.

There are several numerical methods to solve a system of ordinary differential equations like Equation (B.1). The simplest and least accurate method (first order accuracy) is called the *Euler method* where, given a point in the field line $\mathbf{r}_n$, the next one is approximated to

$$\mathbf{r}_{n+1} = \mathbf{r}_n + \Delta s\, \mathbf{F}(s_n, \mathbf{r}_n) + O(\Delta s^2), \tag{B.2}$$

which advances the solution from s_n to $s_{n+1} = s_n + \Delta s$. This method is not recommended for practical use, due to its low accuracy and its instability.

One step further is to take a "trial" step in the midpoint of the interval. Then use the value of both s and $\mathbf{r}$ at that midpoint to compute the "real" step across the whole interval.

In equations,

$$\mathbf{k}_1 = \Delta s\ \mathbf{F}(s_n, \mathbf{r}_n), \tag{B.3}$$

$$\mathbf{k}_2 = \Delta s\ \mathbf{F}(s_n + \frac{\Delta s}{2}, \mathbf{r}_n + \frac{1}{2}\mathbf{k}_1), \tag{B.4}$$

$$\mathbf{y}_{n+1} = \mathbf{y}_n + \mathbf{k}_2 + O(\Delta s^3). \tag{B.5}$$

The method above is called *second-order Runge-Kutta* or *midpoint* method.

In general, the Runge-Kutta method propagates the solution over an interval by combining the information from several Euler-type steps and then using the information obtained to match a Taylor series expansion up to some higher order. Runge-Kutta succeeds virtually always, but it is not usually the fastest.

By far the most often used is the *fourth-order Runge-Kutta formula*, which is:

$$\mathbf{k}_1 = \Delta s\ \mathbf{F}(s_n, \mathbf{r}_n), \tag{B.6}$$

$$\mathbf{k}_2 = \Delta s\ \mathbf{F}(s_n + \frac{\Delta s}{2}, \mathbf{r}_n + \frac{\mathbf{k}_1}{2}), \tag{B.7}$$

$$\mathbf{k}_3 = \Delta s\ \mathbf{F}(s_n + \frac{\Delta s}{2}, \mathbf{r}_n + \frac{\mathbf{k}_2}{2}), \tag{B.8}$$

$$\mathbf{k}_4 = \Delta s\ \mathbf{F}(s_n + \frac{\Delta s}{2}, \mathbf{r}_n + \mathbf{k}_3), \tag{B.9}$$

$$\mathbf{y}_{n+1} = \mathbf{y}_n + \frac{\mathbf{k}_1}{6} + \frac{\mathbf{k}_2}{3} + \frac{\mathbf{k}_3}{3} + \frac{\mathbf{k}_4}{6} + O(\Delta s^5). \tag{B.10}$$

Fourth-order Runge-Kutta method, if combined with an adaptive stepsize algorithm, is quite competitive as long as very high accuracy is not required. For problems where high accuracy is required, there are other methods, like predictor-corrector method, which are more efficient.

More information about the above methods can be found in Press et al. (1986).

Appendix C

Flux Function Coefficients for the Axisymmetric Geometry

For the linear force-free case, in the axisymmetric geometry, the flux function takes the form:

$$A(R,z) = B_0 \frac{d}{2} R \frac{J_1(\alpha R)}{J_1(\alpha d)} + \sum_{n=1}^{\infty} a_n R J_1(\sqrt{\alpha^2 + k_n^2} R) \frac{\cosh(k_n z)}{\cosh(k_n L)}, \tag{C.1}$$

where the terms of the Fourier-Bessel expansion are

$$a_n = \frac{B_0 d}{J_2^2(j_{1,n})} \int_0^1 t \left(t - \frac{J_1(\alpha t d)}{J_1(\alpha d)} \right) J_1(j_{1,n} t) dt. \tag{C.2}$$

This expression can be divided into the sum of two integrals, namely

$$a_n = \frac{B_0 d}{J_2^2(j_{1,n})} I_1 - \frac{B_0 d}{J_2^2(j_{1,n}) J_1(\alpha d)} I_2, \tag{C.3}$$

where

$$I_1 = \int_0^1 t^2 J_1(j_{1,n} t) dt, \tag{C.4}$$

and

$$I_2 = \int_0^1 t J_1(\alpha t d) J_1(j_{1,n} t) dt. \tag{C.5}$$

The expression

$$\frac{d}{dx} \left(x^\ell J_\ell(x) \right) = x^\ell \frac{dJ_\ell(x)}{dx} + \ell x^{\ell-1} J_\ell(x) = x^\ell J_{\ell-1}(x) \tag{C.6}$$

can be obtained by multiplying $(x^{\ell-1})$ by the identity

$$x\frac{dJ_\ell(x)}{dx} = -\ell J_\ell(x) + xJ_{\ell-1}(x). \tag{C.7}$$

Hence

$$\int_a^b x^\ell J_{\ell-1}(x) = \left[x^\ell J_\ell(x)\right]_a^b, \tag{C.8}$$

and therefore

$$I_1 = \frac{1}{(j_{1,n})^3}\int_0^{j_{1,n}} w^2 J_1(w)dw = \frac{J_2(j_{i,n})}{j_{1,n}}, \tag{C.9}$$

where $w = j_{1,n}t$.

Considering u and v as solutions of the Bessel equations:

$$x^2\frac{d^2u}{dx^2} + x\frac{du}{dx} + (\lambda^2x^2 - m^2)u = 0, \tag{C.10}$$

$$x^2\frac{d^2v}{dx^2} + x\frac{dv}{dx} + (\mu^2x^2 - \ell^2)v = 0, \tag{C.11}$$

multiplying Equations (C.10) and (C.11) by v/x and u/x respectively, and integrating along x, the expressions

$$\int x\frac{d^2u}{dx^2}vdx + \int \frac{du}{dx}vdx + \lambda^2\int xuvdx - m^2\int \frac{uv}{x}dx = 0, \tag{C.12}$$

$$\int x\frac{d^2v}{dx^2}udx + \int \frac{dv}{dx}udx + \mu^2\int xuvdx - \ell^2\int \frac{uv}{x}dx = 0. \tag{C.13}$$

are obtained. Subtracting Equation (C.13) from Equation (C.12) and integrating by parts, the resulting equation takes the form:

$$\int\left[(\lambda^2 - \mu^2)x + \frac{\ell^2 - m^2}{x}\right]uvdx = x\left(u\frac{dv}{dx} - v\frac{du}{dx}\right). \tag{C.14}$$

If $\ell = m$ and $Re(\ell) > -1$, the functions u and v become the Bessel functions $u = J_\ell(\lambda x)$ and $v = J_\ell(\mu x)$, and the above equation becomes

$$\int(\lambda^2 - \mu^2)xJ_\ell(\lambda x)J_\ell(\mu x)dx = x\left(J_\ell(\lambda x)\frac{dJ_\ell(\mu x)}{dx} - J_\ell(\mu x)\frac{dJ_\ell(\lambda x)}{dx}\right). \tag{C.15}$$

Using that

$$\frac{dJ_\ell(\lambda x)}{dx} = \lambda \frac{dJ_\ell(x)}{d(\lambda x)} = \lambda \left(-J_{\ell+1}(\lambda x) + \frac{\ell}{\lambda x} J_\ell(\lambda x) \right), \tag{C.16}$$

and rearranging terms, Equation (C.15) can be expressed as:

$$\int x J_\ell(\lambda x) J_\ell(\mu x) = \frac{x}{(\lambda^2 - \mu^2)} \left(\lambda J_{\ell+1}(\lambda x) J_\ell(\mu x) - \mu J_\ell(\lambda x) J_{\ell+1}(\mu x) \right). \tag{C.17}$$

The integral I_2 is a particular solution of the above when $\ell = 1, \lambda = \alpha d, \mu = j_{1,n}$ and $x = t$:

$$I_2 = -\frac{j_{1,n} J_1(\alpha d) J_2(j_{1,n})}{(\alpha^2 d^2 - j_{1,n}^2)}. \tag{C.18}$$

Substituting the expressions for I_1 and I_2 into Equation (C.3), the coefficients a_n finally take the form:

$$a_n = -\frac{\alpha^2 d B_0}{k_n^2 J_2(j_{1,n}) j_{1,n}}. \tag{C.19}$$

Appendix D

Flux Function Coefficients for the Arcade Geometry

For the linear force-free case, in the arcade geometry, the flux function has the form:

$$A_\alpha(x,z) = \sum_{n=0}^{\infty} a_n \cos\left[\frac{(2n+1)\pi x}{2x_0}\right] \exp\left\{-\left[\left((2n+1)\frac{\pi}{2x_0}\right)^2 - \alpha^2\right]^{\frac{1}{2}}(z-z_p)\right\}, \quad \text{(D.1)}$$

where the terms of the Fourier expansion are

$$a_n = \frac{1}{x_0}\int_{-x_0}^{x_0}\left\{\frac{2A_\infty}{\pi}\tan^{-1}\left[\frac{z_0}{x_0}\frac{\sinh(\pi z_p/2z_0)}{\cos(\pi x/2x_0)}\right] - A_\infty\right\}\cos\left[\frac{(2n+1)\pi x}{2x_0}\right]dx. \quad \text{(D.2)}$$

The above expression can be divided into the sum of two integrals, namely

$$a_n = \frac{2A_\infty}{x_0}\left(\frac{2}{\pi}I_1 - I_2\right), \quad \text{(D.3)}$$

where

$$I_1 = \int_0^{x_0}\cos\left[\frac{(2n+1)\pi x}{2x_0}\right]\tan^{-1}\left[\frac{z_0}{x_0}\frac{\sinh(\pi z_p/2z_0)}{\cos(\pi x/2x_0)}\right]dx \quad \text{(D.4)}$$

and

$$
\begin{aligned}
I_2 &= \int_0^{x_0} \cos\left[\frac{(2n+1)\pi x}{2x_0}\right] dx = \frac{2x_0}{(2n+1)\pi} \sin\left[\frac{(2n+1)\pi}{2x_0} x\right]\Big|_0^{x_0} \\
&= \frac{2x_0}{(2n+1)\pi} \sin\left[\frac{(2n+1)\pi}{2}\right] = \frac{2x_0}{(2n+1)\pi}(-1)^n.
\end{aligned}
\tag{D.5}
$$

Calling $\lambda = \pi/(2x_0)$ and $\tau = (z_0/x_0)\sinh(\pi z_p/2z_0)$, and integrating by parts, the first integral becomes

$$
\begin{aligned}
I_1 &= \int_0^{x_0} \cos\left[(2n+1)\lambda x\right] \tan^{-1}\left[\frac{\tau}{\cos(\lambda x)}\right] dx \\
&= \frac{1}{(2n+1)\lambda} \sin\left[(2n+1)\lambda x\right] \tan^{-1}\left[\frac{\tau}{\cos(\lambda x)}\right]\Big|_0^{x_0} \\
&- \frac{\tau}{(2n+1)} \int_0^{x_0} \frac{\sin(\lambda x)\sin\left[(2n+1)\lambda x\right]}{\cos^2(\lambda x) + \tau^2} dx.
\end{aligned}
\tag{D.6}
$$

Since $\sin a \sin b = \frac{1}{2}[\cos(a-b) - \cos(a+b)]$, the above integral becomes

$$
\begin{aligned}
I_1 &= \frac{x_0(-1)^n}{(2n+1)} - \frac{\tau}{2(2n+1)} \int_0^{x_0} \frac{\cos(2n\lambda x) - \cos\left[2(n+1)\lambda x\right]}{\tau^2 + \cos^2(\lambda x)} dx \\
&= \frac{x_0(-1)^n}{(2n+1)} + \frac{\tau}{2(2n+1)}(-I'_n + I'_{n+1}),
\end{aligned}
\tag{D.7}
$$

where

$$
I'_n = \int_0^{x_0} \frac{\cos(2n\lambda x)}{\tau^2 + \cos^2(\lambda x)} dx. \tag{D.8}
$$

Making the change $u = \lambda x$ and applying

$$
\int_0^{\pi/2} \frac{\cos(2nx)dx}{1 - a^2\sin^2 x} = \frac{(-1)^n \pi}{2\sqrt{1-a^2}} \left(\frac{1 - \sqrt{1-a^2}}{a}\right)^{2n}, \tag{D.9}
$$

which can be obtained from Gradshteyn and Ryzhik (1965a), the integral $I'(n)$ takes the form:

$$
\begin{aligned}
I'_n &= \frac{2x_0}{\pi(\tau^2+1)} \int_0^{\pi/2} \frac{\cos(2nu)du}{1 - \varphi^2\sin^2(u)} \\
&= \frac{x_0}{(\tau^2+1)} \frac{(-1)^n}{\sqrt{1-\varphi^2}} \left(\frac{1 - \sqrt{1-\varphi^2}}{\varphi}\right)^{2n};
\end{aligned}
\tag{D.10}
$$

where $\varphi^2 = 1/(\tau^2+1)$. The above result can be simplified to

$$I'_n = \frac{x_0(-1)^n}{\tau\sqrt{1+\tau^2}}\left(\sqrt{1+\tau^2}-\tau\right)^{2n}. \tag{D.11}$$

Therefore,

$$\begin{aligned} -I'_n + I'_{n+1} &= \frac{x_0(-1)^{n+1}}{\tau\sqrt{1+\tau^2}}\left(\sqrt{1+\tau^2}-\tau\right)^{2n}\left[1+\left(\sqrt{1+\tau^2}-\tau\right)^2\right] \\ &= \frac{2x_0}{\tau}(-1)^{n+1}\left(\sqrt{1+\tau^2}-\tau\right)^{2n+1}. \end{aligned} \tag{D.12}$$

Using the above result, Equation (D.7) becomes

$$I_1 = \frac{x_0(-1)^n}{(2n+1)}\left[1-\left(\sqrt{1+\tau^2}-\tau\right)^{2n+1}\right]. \tag{D.13}$$

Equations (D.13) and (D.5) can be implemented into Equation (D.3) to obtain

$$\begin{aligned} a_n &= \frac{4A_\infty}{\pi x_0}\left\{\frac{x_0(-1)^n}{(2n+1)}\left[1-\left(\sqrt{1+\tau^2}-\tau\right)^{2n+1}\right]-\frac{x_0(-1)^n}{(2n+1)}\right\} \\ &= \frac{4A_\infty}{(2n+1)\pi}(-1)^{n+1}\Upsilon^{2n+1}, \end{aligned} \tag{D.14}$$

where

$$\Upsilon = \sqrt{1+\tau^2}-\tau \qquad \text{and} \qquad \tau = \frac{z_0}{x_0}\sinh\left(\frac{\pi z_p}{2z_0}\right). \tag{D.15}$$

Bibliography

Alissandrakis, C. E. (1981). On the computation of constant alpha force-free magnetic field. *Astronomy and Astrophysics*, 100:197–200.

Altschuler, M. D. and Newkirk, G. (1969). Magnetic Fields and the Structure of the Solar Corona. I: Methods of Calculating Coronal Fields. *Solar Physics*, 9:131–+.

Aly, J. J. (1984). On some properties of force-free magnetic fields in infinite regions of space. *The Astrophysical Journal*, 283:349–362.

Amari, T., Aly, J. J., Luciani, J. F., Boulmezaoud, T. Z., and Mikic, Z. (1997). Reconstructing the Solar Coronal Magnetic Field as a Force-Free Magnetic Field. *Solar Physics*, 174:129–149.

Amari, T., Boulmezaoud, T. Z., and Mikic, Z. (1999). An iterative method for the reconstructionbreak of the solar coronal magnetic field. I. Method for regular solutions. *Astronomy and Astrophysics*, 350:1051–1059.

Amari, T. and Luciani, J. F. (1999). Confined Disruption of a Three-dimensional Twisted Magnetic Flux Tube. *The Astrophysical Journal Letters*, 515:L81–L84.

Arnaud, J. and Newkirk, G. (1987). Mean properties of the polarization of the Fe XIII 10747 A coronal emission line. *Astronomy and Astrophysics*, 178:263–268.

Aschwanden, M. J., Newmark, J. S., Delaboudinière, J., Neupert, W. M., Klimchuk, J. A., Gary, G. A., Portier-Fozzani, F., and Zucker, A. (1999). Three-dimensional Stereoscopic Analysis of Solar Active Region Loops. I. SOHO/EIT Observations at Temperatures of (1.0-1.5) X 10^6 K. *The Astrophysical Journal*, 515(2):842–867.

Berger, M. A. (1984). Rigorous new limits on magnetic helicity dissipation in the solar corona. *Geophysical and Astrophysical Fluid Dynamics*, 30:79–104.

Berger, M. A. (1999). Introduction to magnetic helicity . *Plasma Physics and Controlled Fusion*, 41:B167–B175.

Browning, P. K. and Priest, E. R. (1983). The structure of twisted magnetic flux tubes. *The Astrophysical Journal*, 266:848–865.

Chiu, Y. and Hilton, H. (1977). Exact green's function method of solar force-free mag-

netic field computations with constant α. *The Astrophysical Journal*, 212:873–885.

Chodura, R. and Schlueter, A. (1981). A 3D code for MHD equilibrium and stability. *Journal of Computational Physics*, 41:68–88.

Cirtain, J. W., Mackay, D. H., Carcedo, L., and Martens, P. C. H. (2005). The temperature and pressure along coronal loops seen in CDS and TRACE. Paper in preparation.

Dahlburg, R. B., Dahlburg, J. P., and Mariska, J. T. (1988). Helical magnetohydrodynamic turbulence and the coronal heating problem. *Astronomy and Astrophysics*, 198:300–310.

de Jager, C., Švestka, Z., and Howard, R. F., editors (1991). *Solar Physics*, volume 136, No. 1. Kluwer Academic Publishers.

de Jager, C., Švestka, Z., and Howard, R. F., editors (1995). *Solar Physics*, volume 162, Nos. 1-2. Kluwer Academic Publishers.

De Moortel, I. and Hood, A. W. (2000). Wavelet analysis and the determination of coronal plasma properties. *Astronomy and Astrophysics*, 363:269–278.

Fleck, B. and Švestka, Z., editors (1997). *The first results from SOHO*. Kluwer Academic Publishers.

Frazier, E. N. (1972). The Relations between Chromospheric Features and Photospheric Magnetic Fields. *Solar Physics*, 24:98–112.

Gary, G. A. (1989). Linear force-free magnetic fields for solar extrapolation and interpretation. *The Astrophysical Journal Supplement Series*, 69:323–348.

Gary, G. A. (2001). Plasma Beta above a Solar Active Region: Rethinking the Paradigm. *Solar Physics*, 203:71–86.

Glover, A., Harra, L., Matthews, S., Hori, K., and Culhane, J. L. (2001). Long term evolution of a non-active region sigmoid and its coronal mass ejection activity. *Astronomy and Astrophysics Manuscript*, 378(1):239–246.

Grad, H. and Rubin, H. (1958). In *Proc. 2nd International Conference on Peaciful Uses of Atomic Energy*, volume 31, page 190, Geneva. United Nations.

Gradshteyn, I. and Ryzhik, I. M. (1965a). *Table if Integrals, Series and Products*, chapter 3.615, equation 1, page 368. Acamedic Press, Inc., sixth edition.

Gradshteyn, I. and Ryzhik, I. M. (1965b). *Table if Integrals, Series and Products*, chapter 2.423, equation 49, page 368. Acamedic Press, Inc., sixth edition.

Handy, B. N., Acton, L. W., Kankelborg, C. C., Wolfson, C. J., Akin, D. J., Bruner, M. E., Caravalho, R., Catura, R. C., Chevalier, R., Duncan, D. W., Edwards, C. G., Feinstein, C. N., Freeland, S. L., Friedlaender, F. M., Hoffmann, C. H., Hurlburt, N. E., Jurcevich, B. K., Katz, N. L., Kelly, G. A., Lemen, J. R., Levay, M., Lindgren, R. W., Mathur,

D. P., Meyer, S. B., Morrison, S. J., Morrison, M. D., Nightingale, R. W., Pope, T. P., Rehse, R. A., Schrijver, C. J., Shine, R. A., Shing, L., Strong, K. T., Tarbell, T. D., Title, A. M., Torgerson, D. D., Golub, L., Bookbinder, J. A., Caldwell, D., Cheimets, P. N., Davis, W. N., Deluca, E. E., McMullen, R. A., Warren, H. P., Amato, D., Fisher, R., Maldonado, H., and Parkinson, C. (1999). The transition region and coronal explorer. *Solar Physics*, 187:229–260.

Harrison, R. A. (1995). The nature of solar flares associated with coronal mass ejection. *Astronomy and Astrophysics*, 304:585–594.

Hildner, E. (1974). The Formation of Solar Quiescent Prominences by Condensation. *Solar Physics*, 35:123–+.

Hindler, E. (1977). Study of traveling interplanetary phenomena. *D. Reidel Publ. Co., Dordrecht, Holland*, page 3.

House, L. L. (1977). Coronal emission-line polarization from the statistical equilibrium of magnetic sublevels. I - Fe XIII. *The Astrophysical Journal*, 214:632–652.

Hundhausen, A. (1998). *The Many Faces of the Sun*, chapter 5, pages 143–200. Springer-Verlag New York Inc.

Judge, P. G. (1998). Spectral Lines for Polarization Measurements of the Coronal Magnetic Field. I. Theoretical Intensities. *The Astrophysical Journal*, 500:1009–+.

Judge, P. G., Casini, R., Tomczyk, S., Edwards, D. P., and Francis, E. (2001). Coronal Magnetometry: A Feasibility Study. *NASA STI/Recon Technical Report N*, 2:27999–+.

Klimchuk, J. A. and Sturrock, P. A. (1989). Force-free magnetic fields - Is there a 'loss of equilibrium'? *The Astrophysical Journal*, 345:1034–1041.

Kruskal, M. and Schwarzschild, M. (1954). Some instabilities of a completely ionized plasma. *Proceedings of the Royal Society. London*, 223A:348–360.

Kusano, K., Suzuki, Y., and Nishikawa, K. (1995). A solar flare triggering mechanism based on the Woltjer-Taylor minimum energy principle. *The Astrophysical Journal*, 441:942–951.

Lanczos, C. (1966). *Discourse on Fourier Series*, chapter 1.6., pages 26–37. Oliver & Boyd, Tweeddale Court, Edinburgh.

Lang, K. R. (2001). *The Cambridge Encyclopedia of the Sun*. Cambridge University Press.

Levine, R. H. (1976). Evidence for opposed currents in active region loops. *Solar Physics*, 46:159–170.

Longcope, D. W. and Sudan, R. N. (1992). Quasi-static evolution of coronal magnetic fields. *The Astrophysical Journal*, 384:305–318.

Lothian, R. and Browning, P. (1995). Coronal magnetic field equilibrium with discrete flux sources. *Solar Physics*, 161:289–316.

Lothian, R. M. and Hood, A. W. (1989). Twisted magnetic flux tubes - Effect of small twist. *Solar Physics*, 122:227–244.

Low, B. C. (1973). Resistive Diffusion of Force-Free Magnetic Fields in a Passive Medium. *The Astrophysical Journal*, 181:209–226.

Low, B. C. (1977). Evolving force-free magnetic fields. I - The development of the preflare stage. *The Astrophysical Journal*, 212:234–242.

Low, B. C. (1985). Three-dimensional structures of magnetostatic atmospheres. I - Theory. *The Astrophysical Journal*, 293:31–43.

Nakagawa, Y. and Raadu, M. A. (1972). On Practical Representation of Magnetic Field. *Solar Physics*, 25:127–135.

Nakagawa, Y., Raadu, M. A., Billings, D. E., and McNamara, D. (1971). On the Topology of Filaments and Chromospheric Fibrils near Sunspots. *Solar Physics*, 19:72–+.

Nakariakov, V. M. and Ofman, L. (2001). Determination of the coronal magnetic field by coronal loop oscillations. *Astronomy and Astrophysics*, 372:L53–L56.

Parker, E. N. (1979). *Cosmical magnetic fields: Their origin and their activity*. Oxford, Clarendon Press; New York, Oxford University Press, 1979, 858 p.

Petrie, G. J. D. and Lothian, R. M. (2003). An investigation of the topology and structure of constant-alpha force-free fields. *Astronomy and Astrophysics*, 398:287–295.

Petrie, G. J. D. and Neukirch, T. (2000). The Green's function method for a special class of linear three-dimensional magnetohydrostatic equilibria. *Astronomy and Astrophysics*, 356:735–746.

Poletto, G., Vaiana, G. S., Zombeck, M. V., Krieger, A. S., and Timothy, A. F. (1975). A comparison of coronal X-ray structures of active regions with magnetic fields computed from photospheric observations. *Solar Physics*, 44:83–99.

Press, W. H., Flannery, B. P., Teukolsky, S. A., and Vetterling, W. T. (1986). *Numerical Recipes: The Art of Scientific Computing* . Cambridge University Press.

Régnier, S., Amari, T., and Kersalé, E. (2002). 3D Coronal magnetic field from vector magnetograms: non-constant-alpha force-free configuration of the active region NOAA 8151. *Astronomy and Astrophysics*, 392:1119–1127.

Régnier, S. and Amari, T. (2001). Reconstruction of the coronal magnetic field for active region NOAA 8151. In Brekke, P., Fleck, B., and Gurman, J. B., editors, *Recent Insights into the Physics of the Sun and Heliosphere: Highlights from SOHO and other Space Missions*, pages 441–443, San Francisco. International Astronomical

Union, Symposium No. 203, Astronomical Society of the Pacific.

Roberts, B., Edwin, P. M., and Benz, A. O. (1984). On coronal oscillations. *The Astrophysical Journal*, 279:857–865.

Roumeliotis, G. (1993). A new class of exact, nonlinear solutions to the Grad-Shafranov equation. *The Astrophysical Journal*, 404:781–787.

Roumeliotis, G. (1996). The "Stress-and-Relax" Method for Reconstructing the Coronal Magnetic Field from Vector Magnetograph Data. *The Astrophysical Journal*, 473:1095–+.

Sakurai, T. (1981). Calculation of Force-Free Magnetic Field with Non Constant Alpha. *Solar Physics*, 69:343–359.

Schatten, K. H. (1971). . *Cosmic Electrodynamics*, 2:232–+.

Schatten, K. H., Wilcox, J. M., and Ness, N. F. (1969). A model of interplanetary and coronal magnetic fields. *Solar Physics*, 6:442–455.

Schatzman, E. (1965). Model of force free fields. In *IAU Symp. 22: Stellar and Solar Magnetic Fields*, pages 337–+.

Schmidt, H. V. (1964). On the observable effects of magnetic energy storage and release connected with solar flares. In Ness, W. N., editor, *ASS-NASA Symposium on the physics of Solar Flares*, pages 107–114.

Seehafer, N. (1978). Determination of constant alpha force-free solar magnetic fields from magnetograph data. *Solar Physics*, 58:215–223.

Semel, M. (1967). Contribution à létude des champs magnétiques dans les régions actives solaires. *Annales d'Astrophysique*, 30:513.

Semel, M. (1988). Extrapolation functions for constant-alpha force-free fields - Green's method for the oblique boundary value. *Astronomy and Astrophysics*, 198:293–299.

Shafranov, V. D. (1956). The stability of a cylindrical gaseous conductor in a magnetic field. *Soviel Journal of Atomic Energy*, 5:38.

Sheeley, N. R., Howard, R. A., Michels, D. J., Robinson, R. D., Koomen, M. J., and Stewart, R. T. (1984). Associations between coronal mass ejections and metric type II bursts. *The Astrophysical Journal*, 279:839–847.

St. Cyr, O. C. and Webb, D. F. (1991). Activity associated with coronal mass ejections at solar minimum - SMM observations from 1984-1986. *Solar Physics*, 136:379–394.

Steinolfson, R. S. and Tajima, T. (1987). Energy buildup in coronal magnetic flux tubes. *The Astrophysical Journal*, 322:503–511.

Sterling, A. C. (2000). Sigmoid CME source at the sun: Some recent results. *Journal of Atmospheric and Solar-Terrestrial Physics*, 62:1427–1435.

Tang, Y. H., Li, Y. N., Fang, C., Aulanier, G., Schmieder, B., Demoulin, P., and Sakurai, T. (2000). Hα and Soft X-Ray Brightening Events Caused by Emerging Flux. *The Astrophysical Journal*, 534:482–489.

Taylor, J. B. (1974). Relaxation of Toroidal Plasma and Generation of Reverse Magnetic Fields. *Physical Review Letters*, 33:1139–1141.

Trujillo Bueno, J. (2001). Atomic Polarization and the Hanle Effect. In *ASP Conf. Ser. 236: Advanced Solar Polarimetry – Theory, Observation, and Instrumentation*, pages 161–+.

van Ballegooijen, A. A., Cartledge, N. P., and Priest, E. R. (1998). Magnetic Flux Transport and the Formation of Filament Channels on the Sun. *The Astrophysical Journal*, 501:866–+.

van Driel-Gesztelyi, L., Manoharan, P. K., Démoulin, P., Aulanier, G., Mandrini, C. H., Lopez-Fuentes, M., Schmieder, B., Orlando, S., Thompson, B., and Plunkett, S. (2000). Initiation of CME: the role of magnetic twist. *Journal of Atmospheric and Solar-Terrestrial Physics*, 62:1437–1448.

Watson, G. N. (1995a). *A Treatise on the Theory of Bessel Functions*, pages 591–595. Cambridge University Press, second edition.

Watson, G. N. (1995b). *A Treatise on the Theory of Bessel Functions*. Cambridge University Press, second edition.

Wheatland, M. S., Sturrock, P. A., and Roumeliotis, G. (2000). An Optimization Approach to Reconstructing Force-free Fields. *The Astrophysical Journal*, 540:1150–1155.

Wiegelmann, T. (2004). Optimization code with weighting function for the reconstruction of coronal magnetic fields. *Solar Physics*, 219:87–108.

Wiegelmann, T. and Inhester, B. (2003). Magnetic modeling and tomography: First steps towards a consistent reconstruction of the solar corona. *Solar Physics*, 214:287–312.

Wiegelmann, T. and Neukirch, T. (2002). Including spectroscopic information in the reconstruction of coronal magnetic fields. *Solar Physics*, 208(2):233–251.

Wiik, J., Schmieder, B., Kucela, T., Poland, A., P.Brekke, and Simnett, G. (1997). Eruptive prominence and associated CME observed with SUMMER and LASCO (SOHO). *Solar Physics*, 175(2):411–436. Also in Fleck *et al.* Fleck and Švestka (1997).

Wolfson, R. and Verma, R. (1991). Force-free magnetic fields - Generating functions and footpoint displacements. *The Astrophysical Journal*, 375:254–263.

Woltjer, L. (1958). The Stability of Force-Free Magnetic Fields. *The Astrophysical Journal*, 128:384–+.

Wu, S. T., Sun, M. T., Chang, H. M., Hagyard, M. J., and Gary, G. A. (1990). On the numerical computation of nonlinear force-free magnetic fields. *The Astrophysical Journal*, 362:698–708.

Zhao, X. and Hoeksema, J. T. (1993). Unique determination of model coronal magnetic fields using photospheric observations. *Solar Physics*, 143:41–48.

Zhao, X. and Hoeksema, J. T. (1994). A coronal magnetic field model with horizontal volume and sheet currents. *Solar Physics*, 151:91–105.

Zhao, X. P., Hoeksema, J. T., and Scherrer, P. H. (2000). Modeling the 1994 April 14 Polar Crown SXR Arcade Using Three-Dimensional Magnetohydrostatic Equilibrium Solutions. *The Astrophysical Journal*, 538:932–939.

Zirin, H. (1971). Application of the Chromospheric Magnetograph to Active Regions (presented by P. Foukal). In *IAU Symp. 43: Solar Magnetic Fields*, pages 237–242.

Zweibel, E. G. and Boozer, A. H. (1985). Evolution of twisted magnetic fields. *The Astrophysical Journal*, 295:642–647.